

# *Engineering Documents*

---

*University of Pennsylvania*

*Year 1992*

---

## Nonlinear Optical Spectroscopy of Solid/Solid Interfaces

Mohsen S. Yeganeh  
University of Pennsylvania,

University of Pennsylvania, Dissertation, 1992.

This paper is posted at ScholarlyCommons@Penn.  
<http://repository.upenn.edu/seas.docs/6>

NONLINEAR OPTICAL SPECTROSCOPY OF  
SOLID/SOLID INTERFACES

MOHSEN S. YEGANEH

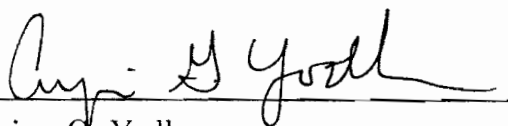
A DISSERTATION

in

PHYSICS

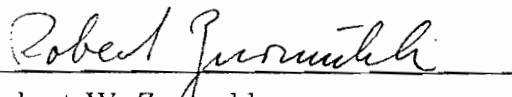
Presented to the Faculties of the University of Pennsylvania in Partial Fulfillment  
of the Requirements for the Degree of  
Doctor of Philosophy.

December 1992



Arjun G. Yodh

Supervisor of Dissertation



Robert W. Zuremuhle

Graduate Group Chairperson

© Copyright 1993

by

Mohsen S. Yeganeh

To Mary, Alexander (Ali) and Sara

# Acknowledgements

There are many people who have contributed in some way to my thesis. I especially thank my advisor, Professor Arjun G. Yodh, for his support and guidance during the last four years. His interest, enthusiasm and most of all his dedication to solving difficult scientific problems was an inspiration for all of us.

I wish to thank Professor E. J. Mele for all the patience and guidance he has offered me in understanding the theoretical aspects of physical problems. I am very grateful to Professor E. W. Plummer who first introduced me to nonlinear optical experiments and made my first PRL possible. I also wish to thank Professor E. Burstein for all his time and patience and Professor S. Rabi for his guidance and for teaching the best course I took at Penn.

It has been a great pleasure and a valuable opportunity to work closely with several students in Arjun's group. I would like to acknowledge the friendship and help of Joe Culver, Peter Kaplan, Ming Kao, Ilya Koltover and Jining Qi. I especially thank Joe for introducing me to Wayne Campbell and Garth Algar...NOT.

My greatest appreciation goes to my beautiful wife, Mary, my son, Alexander

(Ali) and my daughter, Sara, who have been supporting me with love and patience for as long as I can remember. I thank them for the best lesson I have ever learned. They showed me that nothing, even physics, is more important than love. And last, but not least, I thank my parents who made my trip to the U.S. possible ten years ago.

November 1992

# Abstract

## Nonlinear Optical Spectroscopy of Solid/Solid Interfaces

Mohsen S. Yeganeh

Arjun G. Yodh

Three-wave mixing (3WM) spectroscopy is an exciting and relatively unexplored probe of buried solid interfaces. It possesses long penetration depths characteristic of most optical methods and intrinsic interface specificity characteristic of second-order optical processes. In this thesis we present frequency domain measurements of the ZnSe/GaAs(001) heterojunction by second-harmonic (SH) and sum-frequency (SF) generation.

Our experiments reveal an unusual three-wave mixing resonance that arises as a result of virtual transitions between an interfacial quantum well state and the ZnSe valence band. The interfacial quantum well was brought about by interdiffusion of Zn (Ga) into GaAs (ZnSe) during sample growth. The observation introduces a new class of nonlinear optical phenomena at interfaces that can provide useful information about band profiles, diffusion and defects along the boundary of two semiconductors.

We have found that this interfacial SH resonance is sensitive to a variety of *structural* phenomena. In essence *any process* that modifies the band profile *near* the junction will affect the strength of the resonance. We have observed the variation of interface SH spectra with respect to lattice strain relaxation and to surface reconstruction of the buried GaAs. In addition, using a newly developed photomodulation-SHG (PSHG) technique, we have exploited this sensitivity to determine the nature and relative density of interface charge traps as a function of substrate surface reconstruction.

The PSHG method was also used to study free charge trapping mechanisms at ZnSe/GaAs(001) heterointerfaces. Our measurements determined that the interfacial trap-centers are mainly hole-traps with lifetime of 35 sec.

In the course of carrying out these experiments we also observed interference in reflected second harmonic generation from two adjoined nonlinear slabs. A theory for the phenomena was presented and was used to understand our experimental results with ZnSe/GaAs(001) heterostructures. This interference phenomena was introduced as a new methodology to measure the second-order susceptibility of thin overlayer materials.

# Contents

Acknowledgements	v
<b>1 General Introduction</b>	<b>1</b>
<b>2 Second-order Nonlinear Optics: Theoretical Background</b>	<b>9</b>
2.1 Second-order Nonlinear Susceptibility . . . . .	11
2.1.1 $\chi^{(2)}$ and Symmetry . . . . .	13
2.2 Isotropic and Anisotropic Properties of $P^{(2\omega)}$ . . . . .	13
2.3 Higher Order Bulk Contributions . . . . .	15
2.4 Second-order Nonlinear Electronic Fields . . . . .	18
2.4.1 Review of Semi-Infinite Medium Results . . . . .	18
<b>3 Experimental</b>	<b>29</b>
3.1 Optical Arrangements . . . . .	29
3.2 Normalization . . . . .	32
3.2.1 Beam Size Effect . . . . .	36
3.3 Samples . . . . .	37

3.4	Data Acquisition . . . . .	37
3.5	Other Optical Methods . . . . .	39
3.5.1	Linear Spectroscopy . . . . .	39
3.5.2	Thickness Measurements . . . . .	40
<b>4</b>	<b>Physical Properties of ZnSe and GaAs</b>	<b>58</b>
4.1	Crystalline Properties . . . . .	58
4.2	Electronic Structures . . . . .	59
4.2.1	Joint Density of States . . . . .	62
4.2.2	Absorption Coefficient . . . . .	62
4.3	Selection Rules: Bulk . . . . .	63
4.3.1	Basis Function . . . . .	65
4.3.2	Bulk Intraband Transition at $k = 0$ : Two-level Processes . . .	67
4.3.3	Possible Three Level Process at $k = 0$ . . . . .	68
<b>5</b>	<b>Interference in Reflected SHG From Thin Nonlinear Slabs</b>	<b>79</b>
5.1	A Method to Measure $\chi^{(2)}$ of Thin Overlayers . . . . .	79
5.2	Experiment . . . . .	81
5.3	Two Adjoined Nonlinear Optical Slabs: Theory . . . . .	82
5.4	Results . . . . .	86
5.5	$\chi_{xyz}^{(2)}$ Calculation of ZnSe . . . . .	87
5.5.1	Method of Calculation . . . . .	88

<b>6</b>	<b>The Interface</b>	<b>97</b>
6.1	SHG Experiments and Results . . . . .	97
6.2	Two-photon Resonance . . . . .	98
6.3	Spatial Origin . . . . .	99
6.3.1	Surface Contribution . . . . .	99
6.3.2	Higher Order Bulk Contribution . . . . .	99
6.4	Thickness Dependent Measurements . . . . .	100
6.4.1	Bulk Data . . . . .	100
6.4.2	Interfacial Resonance at 2.92 eV . . . . .	101
6.4.3	Interfacial Resonance at 2.72 eV . . . . .	102
6.5	Spectral Origin . . . . .	103
6.5.1	The Effect of the Deformation Potential . . . . .	104
6.6	A New Picture of the Interface: Band Bending . . . . .	106
6.7	The Interfacial Quantum Well in ZnSe/GaAs Heterointerface: A Theoretical Model . . . . .	108
6.7.1	Results of the Calculation . . . . .	111
6.8	Lattice Relaxation As Detected by SHG Spectroscopy . . . . .	116
<b>7</b>	<b>Photomodulation of Second-harmonic Generation</b>	<b>137</b>
7.1	PSHG Experiment . . . . .	138
7.2	Is the Interfacial Resonance at 2.72 eV Associated With the Quantum Well? An Independent Test . . . . .	139

7.3	Identification of the Type of Trap-centers . . . . .	140
7.4	Interfacial Trap Lifetime and Density: A Theoretical Model . . . . .	141
7.5	Variation of Quantum Levels With Photomodulation: A Theoretical Model . . . . .	146
7.6	Interfacial Electronic Trap Lifetime . . . . .	148
7.7	Influence of Buried GaAs Surface Reconstruction on Interfacial Defect Density . . . . .	151
<b>8</b>	<b>Conclusion</b>	<b>167</b>
	<b>Appendix</b>	<b>169</b>
<b>A</b>	$\chi^{(2)}$ and Symmetry	<b>169</b>
<b>B</b>	Boundary Conditions at Vacuum/crystal interface	<b>174</b>
<b>C</b>	Solution of The Nonlinear Wave Equation With Position Depen- dent $\chi^{(2)}$	<b>175</b>
<b>D</b>	Exact Boundary Conditions at Buried Interface	<b>177</b>
<b>E</b>	Transmitted SHG From a Quartz Plate	<b>180</b>
<b>F</b>	Linear Reflectivity of Two Adjoined Slabs	<b>182</b>
<b>G</b>	Joint Density of States: Formulation	<b>185</b>



# List of Tables

2.1	Angular dependence of $P^{(2\omega)}$ for $\bar{4}3m$ and $C_{4v}$ symmetry. . . . .	22
4.1	Character table of $\bar{T}_d$ . . . . .	78
4.2	Direct product table of $\bar{T}_d$ . . . . .	78
6.1	Parameters used for band-profile calculations . . . . .	113
6.2	Energy levels in the quantum well . . . . .	114

# List of Figures

1.1	SHG study of Au/Si(111) . . . . .	7
1.2	SHG and SFG study of CaF <sub>2</sub> /Si(111) . . . . .	8
2.1	A possible mixing process in a three-level system. . . . .	23
2.2	A simplified schematic of crystal and lab frames. . . . .	24
2.3	Rotation anisotropy results . . . . .	25
2.4	Simplified coordinate system . . . . .	26
2.5	SH spectra of GaAs(001) bulk as a function of energy . . . . .	27
2.6	$ \chi_{xyz}^{(2)} $ of GaAs(001) as a function of energy . . . . .	28
3.1	A rough schematic of the optical set-up . . . . .	41
3.2	Optical set-up . . . . .	42
3.3	Schematic of dye laser . . . . .	43
3.4	Power spectra of LDS751 dye . . . . .	44
3.5	Power spectra of LDS925 dye . . . . .	45
3.6	Schematic of prism combination . . . . .	46
3.7	Maker fringes produced by a quartz plate. . . . .	47

3.8	Maker fringes produced by a wedged quartz plate. . . . .	48
3.9	Variation of $\Phi$ as a function of $l_o$ . . . . .	49
3.10	The ZnSe/GaAs(001) sample . . . . .	50
3.11	Schematic of the frequency doubler. . . . .	51
3.12	Schematic of stepper motor . . . . .	52
3.13	A typical SH spectrum of ZnSe/GaAs(001) . . . . .	53
3.14	Optical set-up for linear reflectivity measurements . . . . .	54
3.15	Linear reflectivity spectra . . . . .	55
3.16	Experimental set-up for the thickness measurements. . . . .	56
3.17	Linear reflectivity as a function of the angle of incidence. . . . .	57
4.1	Atomic arrangement in a zinc-blende crystal . . . . .	70
4.2	First Brillouin zone for the GaAs and ZnSe lattice. . . . .	71
4.3	Electronic band structure of ZnSe and GaAs. . . . .	72
4.4	The calculated JDOS of ZnSe and GaAs as function of energy. . . . .	73
4.5	The absorption coefficient of ZnSe and GaAs as a function of energy. . . . .	74
4.6	$E_0$ and $E_0 + \Delta_0$ linear optical transitions . . . . .	75
4.7	Two-level process in GaAs and ZnSe bulk material . . . . .	76
4.8	A possible three-level process in ZnSe or GaAs bulk system. . . . .	77
5.1	Simplified coordinate system . . . . .	91
5.2	Bulk SHG signal . . . . .	92
5.3	Variation in the SHG intensity with thickness . . . . .	93

5.4	Second-order susceptibility of ZnSe . . . . .	94
5.5	Relative phase of ZnSe susceptibility with respect to $\chi_{xyz}^{(2)}$ of GaAs . .	95
5.6	Calculated $\chi_{xyz}^{(2)}$ of ZnSe . . . . .	96
6.1	Interfacial SH spectrum of 215 Å sample . . . . .	119
6.2	Bulk SH spectrum of 215 Å sample . . . . .	120
6.3	The variation of SH and SF intensity as a function of one-photon energy	121
6.4	The variation of SH and SF intensity as a function of two-photon energy	122
6.5	Auger electron spectrum of the etched sample . . . . .	123
6.6	The SH spectrum before and after chemical etching. . . . .	124
6.7	SH intensity as a function of two-photon energy in S-in/S-out and S-in/P-out polarization configurations. . . . .	125
6.8	A simplified coordinate for the model that describes the 2.92 eV reso- nance and the 2.92 eV interfacial resonance as a function of overlayer thickness. . . . .	126
6.9	Thickness dependence of the 2.72 eV interfacial resonance. . . . .	127
6.10	The optical transitions and band splitting caused by the deformation potential. . . . .	128
6.11	Normalized SHG intensity of the interface and deduced $\chi_{xyz}^{(2)}$ of the ZnSe bulk overlayer. . . . .	129

6.12	The energy-band profile as a function of depth for ZnSe/GaAs(001) and the wavefunction of the first three eigenstates of the quantum well along with the valence band wavefunction. . . . .	130
6.13	Calculated matrix element of dipole moment as a function of the energy for the interfacial quantum well. . . . .	131
6.14	Calculated permanent dipole moments. . . . .	132
6.15	Relative strength of the SH signal as a function of energy in the two level process . . . . .	133
6.16	A schematic representation of the formation of misfit dislocations. . .	134
6.17	Interfacial resonance SHG spectra near 2.72 eV as a function of overlayer thickness. . . . .	135
6.18	Normalized SHG peak intensity at 2.72 eV as a function of overlayer thickness. . . . .	136
7.1	Schematic of the PSHG experiment . . . . .	154
7.2	Variation of SHG intensity for bulk and interfacial resonances. . . . .	155
7.3	Normalized variation of the resonance interface SHG intensity at 2.72 eV as a function of lamp photon energy. . . . .	156
7.4	Variation of energy-band profile with photomodulation. . . . .	157
7.5	Change of the valence band wavefunction with perturbation. . . . .	158
7.6	Variation of quantum well wavefunction with photomodulation.. . . .	

7.7	Normalized variation of SHG intensity with time for a photoexcitation intensity of $5.3\mu\text{W}/\text{cm}^2$ . . . . .	160
7.8	The inverse of lifetime ( $\tau$ ) as a function of intensity. . . . .	161
7.9	Normalized SH intensity with 2.4 eV and 3.0 eV lamp photon energy as a function of time. . . . .	162
7.10	Normalized steady state SH intensity as a function of lamp intensity with a 3.0 eV photomodulation beam. . . . .	163
7.11	Steady state PSHG for 3x1 and 2x4 samples. . . . .	164
7.12	SHG spectra for 3x1 and 2x4 buried GaAs surface reconstructed samples	165
7.13	Steady state PSHG for 3x1 and 2x4 samples with a 2.4 eV photomod- ulation beam. . . . .	166
F.1	Simplified coordinate for linear reflectivity . . . . .	184

# Chapter 1

## General Introduction

When two dissimilar materials are brought in contact with each other, a new class of physical problems is generated. The interface of this system, as compared to the bulk, has intrinsically different physical properties that strongly depend on the interfacial atomic arrangement and the electronic structure of the two materials joined at the junction. The development of a microscopic understanding of these exciting physical problems is clearly a challenging scientific task.

Different physical phenomena are responsible for the new properties of the system. For example, a new interfacial bond can have electronic states that are different from the neighboring bulk materials [1, 2, 3, 4]; a new charge distribution, resulting from interdiffusion or defects, generates a different band profile which can lead to new electronic states [5, 6, 7]. All of these phenomena influence the macroscopic physical properties of the entire system and in particular the thin overlayer.

Thin films are fundamentally important in their own right. Charge transport, low dimensional excitations, defect states and deformation potentials in thin films are all the subject of much research [8, 9, 10, 11, 12, 13]. The increased attention in this area results in part from the existence of many interesting physical phenomena which only exist in materials with low dimensionality. In general, the bulk physical properties of a thin overlayer are dependent on the interface, particularly as the overlayer thickness becomes comparable to the diffusion length of the free carriers. Solid/solid interfaces and thin films are also of technological importance. The successful growth, fabrication and characterization of electronic devices is a direct consequence of an accurate fundamental knowledge of buried interfaces.

Although new methods have been developed and used with limited success to reveal specific features about the buried interface [14, 15, 16, 17], basic problems still remain. Solid/solid interfaces are buried under a thick overlayer which is greater than the escape and penetration depth of an electron in a solid. This makes buried interfaces inaccessible to the electronic diagnostic techniques currently being used widely in surface science. Linear optical scattering is a powerful probe to investigate the bulk of a material, however, it gives very little interface specificity. On the other hand, second-order nonlinear optical probes are intrinsically sensitive to interfaces and have proven to be a powerful tool in surface diagnostics. For example the results of surface studies using second-order nonlinear optics, namely sum-frequency (SF) and second-harmonic (SH) generation, corroborate with results obtained using

electronic techniques.

Therefore, nonlinear optical methods are well suited for studying buried interfaces, both because they are able to penetrate bulk material and because they have demonstrated interface sensitivity. Demonstration of surface sensitivity of SHG and SFG was the subject of research for many years [18, 19, 20]. While the surface sensitivity of SHG and SFG has been used extensively, few SHG studies have been performed on buried solid interfaces [21, 22, 23, 24, 25] and even fewer have utilized the spectroscopic aspect of SHG [22, 24, 25].

The first experiment on solid/solid interfaces was performed by McGilp and Yeh on Au/Si systems [23]. The polarized SHG intensity was measured as a function of the input polarization of the laser beam. It was found that the symmetry of the interface changed as a function of the Au overlayer coverage. See Fig. 1.1. This change was explained as follows. The gold absorption produces interface states associated with steps. These steps, and thus the interface states, were found to be localized along the  $[\bar{1}\bar{1}2]$  direction which change the symmetry of the junction.

The first nonlinear optical *spectroscopy* experiments on solid/solid interfaces were carried out by Heinz *et. al.* on  $\text{CaF}_2/\text{Si}(111)$  [22]. SFG and SHG measurements as a function of the fundamental photon energy were used to determine an interfacial band gap. See Fig. 1.2. The interesting result of this work is due to the new interfacial bond combination. It was found that the Ca (4s) and Si (3p) orbitals hybridize to produce bonding and antibonding bands at the interface with an energy separation

well within the band gap of the  $\text{CaF}_2$ . Heinz *et. al.* detected a transition between the bonding and antibonding orbitals of the interface states.

This thesis is concerned with the use of nonlinear optical spectroscopy to investigate ZnSe/GaAs heterostructures. ZnSe/GaAs(001) is an important *non-centrosymmetric* system that has received intense recent interest, in part, due to laser action being achieved in ZnSe near its optical band-gap energy of 2.67 eV [26]. The ZnSe/GaAs heterostructure exhibits a rich phenomenology brought about by an interplay of the physics and chemistry of the interface. For example, different reconstructions of the buried GaAs surface created during epitaxial growth have been observed to induce dramatically different photoconductive properties [27]. Thin ZnSe layers grow pseudomorphically on GaAs and then abruptly relax, leaving dislocations and point defects at the buried interface [28, 29, 30], charge traps are believed to also exist at the interface, however, their nature and origin are only partially understood [31].

In contrast to  $\text{CaF}_2/\text{Si}(111)$ , the new phenomena at the interface of the ZnSe/GaAs heterostructure arises as a result of a new band profile which allows new electronic states in the system. This band profile was first determined by Kassel *et. al.* [32]. Their electrolyte electroreflectance measurements showed a weak peak corresponding to a real cross-over transition between the valence band of ZnSe and the resonance state of the quantum well created by the band bending. This thesis concentrates

on understanding the effect that this band bending has on nonlinear optical spectroscopy. Our work provides new examples of the sensitivity of SHG to buried interfaces [25], interfacial defects, lattice relaxation, substrate surface reconstruction, and band bending [33]. It also contains newly developed techniques to measure the nonlinear susceptibility of thin overlayers [34], interfacial trap lifetime [35], relative interfacial trap density, and critical thickness, and to determine the interfacial charge.

This report is organized in the following way. A general discussion of second-order nonlinear optics is given in Chapter 2. The symmetry dependence of the second order susceptibility and the azimuthal angular dependence of the nonlinear polarization term are discussed. Higher order contributions are briefly addressed and the anisotropic and isotropic part of these contributions are explained. Lastly, SHG intensity in reflection from a semi-infinite media is described.

In Chapter 3, a description of our samples and experimental set-up is given along with an explanation of some important considerations which arise in this type of experiment. Other linear optical methods which were used to characterize the samples are also discussed.

In Chapter 4 some of the important physical properties of ZnSe and GaAs are discussed. Selection rules and possible optical transitions are explained.

The subject of Chapter 5 is the interference in reflected second-harmonic generation from two adjoined nonlinear slabs. A theory for the phenomena is presented

and is used to explain the experimental results obtained using ZnSe/GaAs(001) heterostructures. This phenomenon is introduced as a new method to measure the second-order susceptibility of a thin overlayer. The experimental results of the frequency-dependent bulk nonlinear susceptibility for ZnSe near the  $E_0$  transition are also presented and compared to our theoretical calculations.

In Chapter 6 we have discussed the use of three-wave mixing spectroscopy for probing the interfacial electronic structure of a ZnSe/GaAs(001) heterostructure. Observed spectral features at 2.72 and 2.92 eV are explained. This chapter includes details on thickness dependent measurements that were used to determine the spatial origin of SH signals in multilayer systems. A theoretical model for the interface quantum well is also provided.

Chapter 7 is devoted to a new experimental technique we have developed, called photomodulation-second-harmonic generation (PSHG). We explain the basic theory of this technique and then present practical applications towards measurements of interface charge, trap lifetimes and trap density.

A brief conclusion is given in Chapter 8.

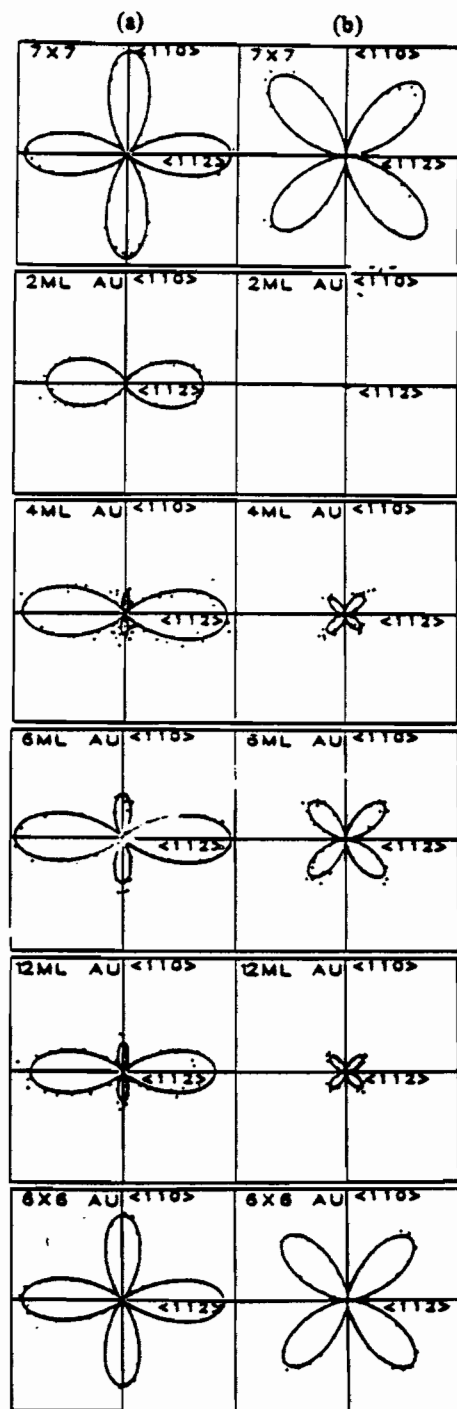


Figure 1.1: SH intensity as a function of input polarization for Si(111)  $7 \times 7$  and Au-covered Si(111) along (a)  $[11\bar{2}]$  and (b)  $[1\bar{1}0]$ . One can see that the interfacial symmetry changes as a function of the gold coverage. (From Ref. [23])

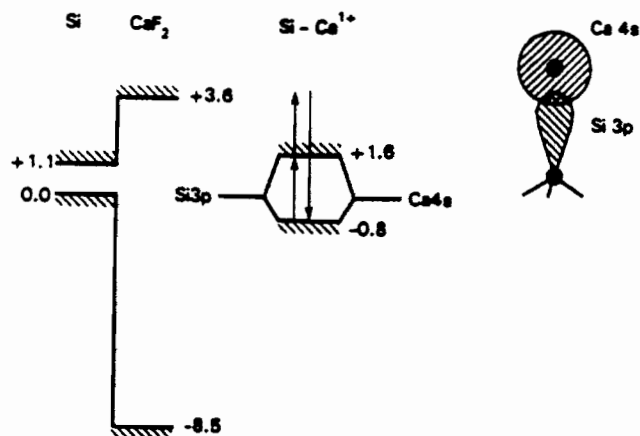
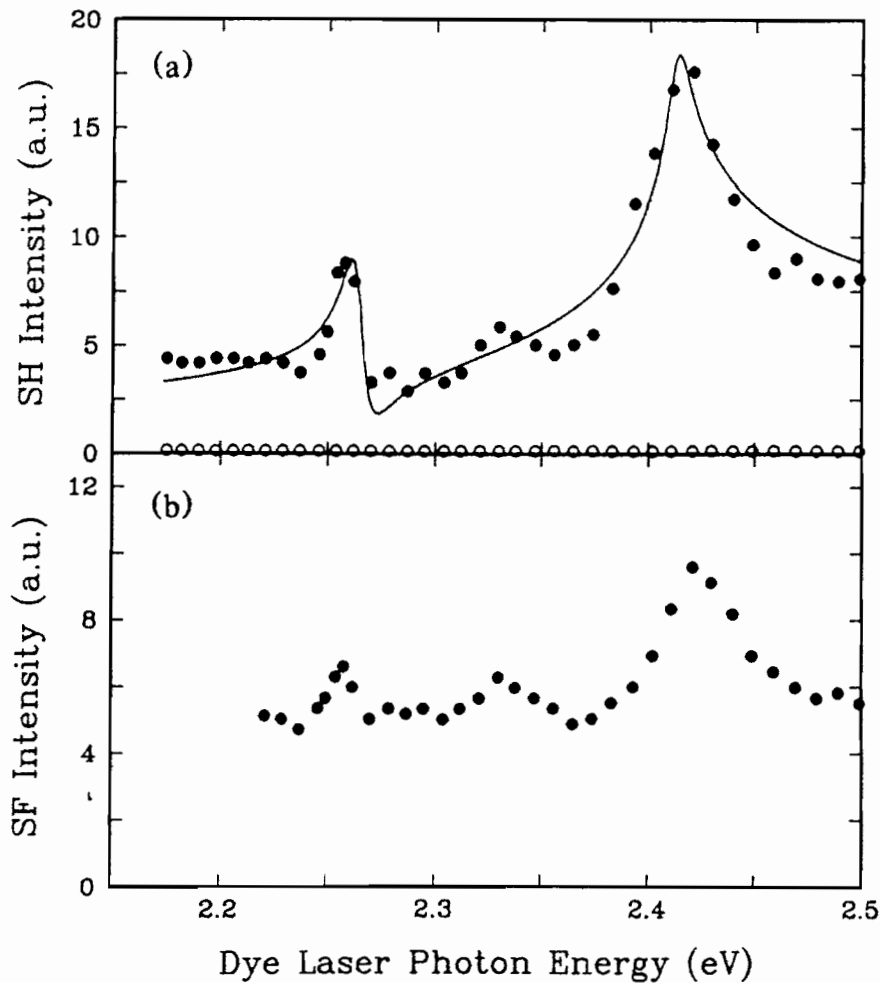


Figure 1.2: (a) Resonant second-harmonic and (b) resonant sum-frequency generation of CaF<sub>2</sub>/Si(111). The filled symbols represent signal from the interface and the open symbols stand for signal from the oxide Si(111) surface. (c) The interfacial band profile of CaF<sub>2</sub>/Si(111). The schematic representation of hybridized Si(3P) dangling bond and Ca<sup>+</sup>(4S) orbitals is also displayed. (From Ref. [22])

## Chapter 2

# Second-order Nonlinear Optics: Theoretical Background

The response of a material to strong optical fields of lasers can be nonlinear. This nonlinearity is characterized through the susceptibility that gives rise to a nonlinear polarization source,  $P^{NLS}$ . The nonlinear source polarization radiates an electromagnetic wave with angular frequency which is different than the frequency of the incident laser beam. The propagation of the radiated electric field,  $\mathbf{E}$ , must obey the nonlinear wave equation [36]:

$$\nabla \times \nabla \times \mathbf{E}^{(\omega_3)} + \frac{\epsilon}{c^2} \frac{\partial^2}{\partial t^2} \mathbf{E}^{(\omega_3)} = -\frac{4\pi}{c^2} \frac{\partial^2}{\partial t^2} \mathbf{P}^{(\omega_3)}. \quad (2.1)$$

Here  $\omega_3$  is the angular frequency of the nonlinear polarization.  $\epsilon$  is the frequency-dependent linear dielectric constant of the medium. We are only interested in the

second-order nonlinear response of the system, where we can write:

$$\omega_3 = \omega_1 + \omega_2. \quad (2.2)$$

Here  $\omega_1$  and  $\omega_2$  are the angular frequencies of the incident laser beams. Generation of an electric field at  $\omega_3$  is called sum-frequency generation (SFG) when  $\omega_1 \neq \omega_2$ , and second-harmonic generation (SHG) when  $\omega_1 = \omega_2 \equiv \omega$ . The nonlinear polarization is related to the incident beam as follows:

$$P_i^{(\omega_3)} = \chi_{ijk}^{(\omega_3)} : \mathbf{E}_j^{(\omega_1)} \mathbf{E}_k^{(\omega_2)} + \Gamma_{ijkl}^{(\omega_3)} \mathbf{E}_j^{(\omega_1)} \nabla_k \mathbf{E}_l^{(\omega_2)}. \quad (2.3)$$

The first part is the second-order term in the expansion of  $P$  as a function of local electric field. This is the dipole contribution. The second term arises from the nonlocal response of the system, which is the expansion of  $P$  as a function of the derivative of the electric field. This term carries the electric quadrupole and magnetic dipole contributions. The higher order term of  $P$  can be written [37, 38, 39, 40]

$$P_i^{(2\omega)} = (\delta - \beta - 2\gamma)(\mathbf{E} \cdot \nabla) E_i + \beta E_i (\nabla \cdot \mathbf{E}) + \gamma \nabla_i (\mathbf{E} \cdot \mathbf{E}) + \zeta E_i \nabla_i E_i. \quad (2.4)$$

Here  $\delta, \beta, \gamma$ , and  $\zeta$  are phenomenological constants. It should be noted that the first three terms are isotropic in character, and the last term is anisotropic with respect to the orientation of the crystal. The relationship between  $\delta, \beta, \gamma, \zeta$ , and  $\Gamma_{ijkl}$  will be discussed later in this chapter.

The dipole contribution in the system under investigation dominates and will be discussed in more detail. Under the dipole approximation the nonlinear polarization,

$P^{NLS}$ , for SHG can be written as:

$$P_i^{(2\omega)} = \chi_{ijk}^{(2\omega)} : \mathbf{E}_j^{(\omega)} \mathbf{E}_k^{(\omega)}. \quad (2.5)$$

The second-order susceptibility,  $\chi^{(2)}$ , is the response of the system at  $2\omega$  and couples the incident photons to the medium. The underlying physics of the second-order nonlinear optics can be explained via this susceptibility. In the next few sections we will discuss some of the physical aspects of this susceptibility in more detail.

## 2.1 Second-order Nonlinear Susceptibility

There are several methods to formulate and discuss the second-order nonlinear susceptibility [41, 42, 43, 36]. A general and useful derivation for  $\chi^{(2)}$  uses the one body density matrix. The details of this approach are given in many text books [36] and are not reproduced here. The resultant expression for  $\chi_{ijk}^{(2)}$  is

$$\chi_{ijk}^{(2)} = -N \frac{e^3}{\hbar^2} \sum_{g,n,n'} \frac{\langle g|r_i|n'\rangle \langle n'|r_j|n\rangle \langle n|r_k|g\rangle}{(2\omega - \omega_{ng} + i\Gamma_{ng})(\omega - \omega_{n'g} + i\Gamma_{n'g})} + \dots \quad (2.6)$$

where  $N$  is the number density of electrons and  $r_i$  is the space operator in the  $i$ th direction. The states  $|g\rangle, |n\rangle$  and  $|n'\rangle$  are eigenstates of the *unperturbed* system, and  $\Gamma$  is a damping factor. The expression for  $\chi_{ijk}^{(2)}$  carries eight terms describing the different time ordering of the photons. The multiplication of three matrix elements in each term presents the coupling of the photons with matter in three separate steps. As an example  $(r_i)_{gn'}(r_j)_{n'n}(r_k)_{ng}$  corresponds to: (1) the coupling of the ground state,  $|g\rangle$ , to the excited state,  $|n\rangle$ , with the  $k$  component of the field in the

first step of the mixing, (2) the coupling of the excited state,  $|n\rangle$ , to another excited state,  $|n'\rangle$ , with the  $j$  component of field in the second step, and (3) the coupling of the excited state,  $|n'\rangle$ , with the ground state,  $|g\rangle$ , with the  $i$  component of the field in the final step. The summation indicates that the process must go over all possible excited states. One of the possible mixing processes is shown in Fig. 2.1.

The odd number of matrix elements in the numerator of each term also shows the sensitivity of  $\chi^{(2)}$  to the symmetry of the system. For example, if a system is invariant under inversion symmetry the product of  $(r_i)_{gn'}(r_j)_{n'n}(r_k)_{ng}$ , independent of the subscripts  $i, j$ , and  $k$ , is always zero. The non-zero value of  $\chi^{(2)}$  appears in the presence of a broken symmetry. This property of  $\chi^{(2)}$  makes second-order nonlinear optics a powerful tool for studying the interfaces, where symmetry in the normal direction to the junction is broken. We will discuss the symmetry dependence of  $\chi^{(2)}$  in more detail in Section 2.1.1.

The resonant nature of  $\chi^{(2)}$ , as expressed in the denominator of each term, is another important aspect of the second-order susceptibility. Whenever the energy of the input beam (fundamental) or output beam (upconverted photon) matches a transition,  $\chi^{(2)}$  becomes a large pure imaginary number. This results in a peak in the SH or SF spectra. Of course, to estimate the peak intensity we must also consider the joint density of states of the system. This part of the discussion will be explained in chapter 5, and the result will be compared to the experimental data.

### 2.1.1 $\chi^{(2)}$ and Symmetry

The second-order susceptibility tensor,  $\chi^{(2)}$ , has 27 elements. However, in most practical applications many elements of  $\chi^{(2)}$  are zero and some of the non-zero terms are related. This greatly simplifies any investigation involving  $\chi^{(2)}$ . Our studies, described in Appendix A, show that the non-zero elements of  $\chi^{(2)}$  for  $C_{4v}$  symmetry (e.g. surface of fcc[001]) are:

$$\chi_{xxz} = \chi_{yyz}$$

$$\chi_{xzx} = \chi_{yzy}$$

$$\chi_{zxx} = \chi_{zyy}$$

and

$$\chi_{zzz}.$$

In the same Appendix we show that the only non-zero elements of  $\chi^{(2)}$  in GaAs(001) or ZnSe(001) with  $\bar{4}3m$  symmetry are:

$$\chi_{ijk} \text{ with } i \neq j \neq k.$$

## 2.2 Isotropic and Anisotropic Properties of $P^{(2\omega)}$

With the use of symmetry the number of nonzero elements of  $\chi^{(2)}$  can be appreciably reduced (see Appendix A), and with the knowledge of the relationships between the non-zero elements of the  $\chi^{(2)}$  tensor, we can predict the dependence of the second-order polarization,  $\mathbf{P}^{(2\omega)}$ , on second-order susceptibility,  $\chi^{(2)}$ , and azimuthal angle

$\phi$ , which is the angle between plane of incidence and a fixed axis of the crystal. This section will describe the calculation of  $\mathbf{P}^{(2\omega)}$  as a function of  $\chi^{(2)}$  and  $\phi$  for  $C_{4v}$  (non-reconstructed GaAs[001] surface) and  $\bar{4}3m$  (bulk of GaAs[001]) symmetry in a P-in/S-out polarization configuration. Calculations for the other polarization configurations should then be straightforward, and the results are tabulated in Table 2.1.

First we write the expression of  $P^{(2\omega)}$  in the lab frame (see Fig. 2.2). In the following we will take  $x \equiv 1$ ,  $y \equiv 2$ , and  $z \equiv 3$  for convenience. Summation over repeated indices is understood.

$$P_2^{(2\omega)} = \chi_{2jk}^{(L)} E_i E_j = \chi_{233}^{(L)} E_3 E_3 + \chi_{211}^{(L)} E_1 E_1 + 2\chi_{213}^{(L)} E_1 E_3 \quad (2.7)$$

The tensor elements of  $\chi_{ijk}^{(L)}$  in the lab frame are related to the  $\chi_{ijk}^{(C)}$  in the crystal frame through the rotation operator,  $R(\phi)$ ,

$$\chi_{ijk}^{(L)} = R(\phi)_{i\alpha} R(\phi)_{j\beta} R(\phi)_{k\gamma} \chi_{\alpha\beta\gamma}^{(C)} \quad (2.8)$$

where

$$R(\phi) = \begin{pmatrix} \cos \phi & -\sin \phi & 0 \\ \sin \phi & \cos \phi & 0 \\ 0 & 0 & 1 \end{pmatrix} \quad (2.9)$$

Thus,

$$\chi_{233}^{(L)} = R_{2i} R_{3j} R_{3k} \chi_{ijk}^{(C)} = R_{2i} R_{33} R_{33} \chi_{i33}^{(C)} = R_{2i} \chi_{i33}^{(C)}. \quad (2.10)$$

Here  $\phi$  is the angle between the [100] direction and the plane of incidence. For the  $C_{4v}$  system the value of  $i$  must be equal to 3, however,  $R_{23}$  is zero and thus  $\chi_{233}^{(L)} = 0$ . The situation for the  $\bar{4}3m$  system is simpler since  $\chi_{233}^{(C)}$  is zero independent of  $i$ .

With the same method we can deduce that the tensor element of  $\chi_{211}^{(L)}$  is also zero.

The last element,  $\chi_{123}^{(L)}$  is worth looking at in more detail:

$$\chi_{213}^{(L)} = R_{2i}R_{1j}R_{3k}\overset{C}{\chi}_{ijk}^{(X)} = R_{2i}R_{1j}\overset{C}{\chi}_{ij3}^{(X)} \quad (2.11)$$

For the  $\bar{4}3m$  symmetry  $ij3 = 123 = 213$  and  $C_{4v}$  requires that  $ij3 = 113 = 223$ .

This leads to

$$\begin{cases} \chi_{213}^{(L)} = 0, & \text{for } C_{4v} \text{ and} \\ \chi_{123}^{(L)} = \cos(2\phi)\overset{C}{\chi}_{123}^{(C)}, & \text{for zinc-blende(001) crystal} \end{cases} \quad (2.12)$$

This indicates that the SHG *intensity* in the P-in/S-out polarization configuration varies as a function of  $\cos^2(2\phi)$  for the  $\bar{4}3m$  symmetry and is zero for  $C_{4v}$  systems.

The results for  $\bar{4}3m$  system are compared with the experimental data in Fig. 2.3.

There is excellent agreement. The details of the experiments will be discussed in the next chapter.

## 2.3 Higher Order Bulk Contributions

We have seen that the higher order bulk contribution is non-local and can be written as:

$$P_i = \Gamma_{ijkl}E_j\nabla_kE_l \quad (2.13)$$

The fourth rank tensor,  $\Gamma_{ijkl}$ , can be studied using the symmetry of the system. For cubic materials such as GaAs and ZnSe (with  $\bar{4}3m$  symmetry), the only nonzero elements are:

$$\Gamma_{xxxx} = \Gamma_{yyyy} = \Gamma_{zzzz}$$

$$\begin{aligned}
\Gamma_{yzyz} &= \Gamma_{zxxx} = \Gamma_{xzzx} = \Gamma_{yxyx} = \Gamma_{xyxy} \\
\Gamma_{yyzz} &= \Gamma_{zzyy} = \Gamma_{zzxx} = \Gamma_{xxzz} = \Gamma_{xxyy} = \Gamma_{yyxx} \\
\Gamma_{yzzz} &= \Gamma_{zyyz} = \Gamma_{zxxx} = \Gamma_{xzzx} = \Gamma_{yxyx} = \Gamma_{xyxy}
\end{aligned} \tag{2.14}$$

These relationships were derived in a similar way as those discussed in Appendix A. With S-in/S-out polarization configuration the second order polarization along the  $y$ -axis is:

$$P_y = \Gamma_{yyiy}^{(L)} E_y k_i E_y \tag{2.15}$$

The subscript  $i$  can only be equal to  $x$  and  $z$ . The fourth rank tensor element  $\Gamma_{yyiy}^{(L)}$  represents its value in the lab frame and can be transformed to the crystal frame by a rotation operator as seen before. Using equation 2.14 and 2.15 we can rewrite the expression as:

$$P_y = -\frac{1}{4} \sin(4\phi) (\Gamma_{xyyx}^{(C)} + \Gamma_{yxyx}^{(C)} - \Gamma_{xxxx}^{(C)} + \Gamma_{xxyy}^{(C)}) E_y^2 k_x. \tag{2.16}$$

With

$$\zeta = \Gamma_{xxxx} - \Gamma_{xyyx} - \Gamma_{yxyx} - \Gamma_{xxyy}$$

the polarization can be rewritten in the form:

$$P_y = \zeta \frac{\sin 4\phi}{4} E_y^2 k_x. \tag{2.17}$$

Clearly in this polarization configuration one can study the isotropic contribution of higher order nonlinearity (i.e.  $\zeta$ ).

Using the same method with the S-in/P-out polarization configuration, the first and third components of the polarization can be written as:

$$P_x = \Gamma_{xijk}^{(L)} E_i k_j E_k = \Gamma_{xyjy}^{(L)} E_y^2 k_j = \Gamma_{xyxy}^{(L)} E_y^2 k_x + \Gamma_{xyzy}^{(L)} E_y^2 k_z, \quad (2.18)$$

and after transforming  $\Gamma^{(L)}$  to the crystal frame we have

$$P_x = -2\sin^2 \phi \cos^2 \phi [\Gamma_{xxxx}^{(C)} + \Gamma_{xxyy}^{(C)} + \Gamma_{xyyx}^{(C)}] E_y^2 k_x + \Gamma_{xyxy}^{(C)} (\sin^4 \phi + \cos^4 \phi) E_y^2 k_z \quad (2.19)$$

With conventional parameters [38]

$$\Gamma_{xxxx}^{(C)} = \gamma + \zeta \quad (2.20)$$

$$\Gamma_{xxyy}^{(C)} = \beta \quad (2.21)$$

$$\Gamma_{xyyx}^{(C)} = \gamma - \beta - 2\gamma \quad (2.22)$$

$$\Gamma_{xyxy}^{(C)} = 2\gamma \quad (2.23)$$

we can rewrite the polarization as

$$P_x = -2\zeta E_y^2 k_x \sin^2 \phi \cos^2 \phi + 2\gamma E_y^2 k_z (\sin^4 \phi + \cos^4 \phi) \quad (2.24)$$

and

$$P_z = \Gamma_{zyiy} E_y^2 k_i = \Gamma_{zyxy}^{(L)} E_y^2 + \Gamma_{zyzy}^{(L)} E_y^2 k_z = \Gamma_{zxzx}^{(C)} E_y^2 k_z = \frac{\gamma}{2} E_y^2 k_z. \quad (2.25)$$

This relationship suggests that in the S-in/P-out polarization configuration one can study the tensor element  $\gamma$  at  $\phi = 0$ . However, at this orientation the surface or interface also contributes to the radiation. *Thus, one can only study the linear combination of  $\gamma$  and the surface tensor elements.*

## 2.4 Second-order Nonlinear Electronic Fields

Now that we have established how the second-order order nonlinear source polarization depends on the susceptibilities, we can study the field generated by this polarization. The complete form of the nonlinear field is quite complex. This is mostly due to the boundary conditions and the coupling to the linear fields. In the following section, we will describe the second harmonic field in a simple semi-infinite slab. Because our experiments utilize the p-in/s-out polarization configuration, calculation of p-in/s-out will be given in detail. Calculation of the s-in/p-out and p-in/p-out polarization configurations are straightforward extensions of the p-in/s-out results.

We choose the coordinate system so that the vacuum/crystal boundary is at  $z = 0$ , and the plane of incidence contains the  $z$ - and  $x$ -axis (Fig. 2.4). For all the expressions below, the subscript “1” is used for the semi-infinite medium. The subscript “ $Rlm$ ” refers to the reflected harmonic wave which is generated in medium “ $l$ ” and propagates through medium “ $m$ ”. We also assume that the second-order susceptibilities and dielectric constants change discontinuously at all interfaces.

### 2.4.1 Review of Semi-Infinite Medium Results

In the semi-infinite problem, first solved by Bloembergen and Pershan [46], a monochromatic plane wave with frequency  $\omega$  impinges from vacuum onto a crystal that lacks inversion symmetry. The incident wave is refracted into the crystal, and the transmitted field interacts with the nonlinear medium to produce a second harmonic

source polarization,  $\mathbf{P}^{(2\omega)}$ , and thus an electric field,  $\mathbf{E}^{(2\omega)}$ . The propagation of this field is described by equation 2.1. The wavevector of the source term in Eq. (2.5) is  $\mathbf{k}_b = 2\mathbf{k}_t$ .

In the following calculations we assume that  $\mathbf{P}^{(2\omega)}$  is independent of position inside the semi-infinite medium. The exact solution to Eq. (2.1) under this circumstance is

$$\nabla \cdot \mathbf{E}^{(2\omega)} = \mathbf{E}_f^{(2\omega)} e^{i(\mathbf{k}_f \cdot \mathbf{r} - 2\omega t)} - \frac{4\pi(4\omega^2/c^2)P}{k_f^2 - k_b^2} \left[ \hat{\mathbf{p}} - \frac{\mathbf{k}_b(\mathbf{k}_b \cdot \hat{\mathbf{p}})}{k_f^2} \right] e^{i(\mathbf{k}_b \cdot \mathbf{r} - 2\omega t)}, \quad (2.26)$$

where  $\hat{\mathbf{p}}$  is a unit vector in the direction of  $\mathbf{P}^{(2\omega)}$ . The first term of Eq. (2.26) is the free wave solution. This wave propagates in the direction of  $\mathbf{k}_f$ , and its amplitude is determined by boundary conditions. The second term is a particular solution of the nonlinear wave equation. This field is *bound* to the fundamental wave, and propagates with wavevector  $\mathbf{k}_b$ . The subscripts “f” and “b” refer to free and bound waves respectively, and  $k_{fi}$  ( $k_{bi}$ ) represents the magnitude of the free (bound) wavevector in medium  $i$ .

A harmonic wave is also radiated into the vacuum. Since there is no source term in the vacuum, the solution of Eq. (2.1) is simply

$$\mathbf{E}_{R10}^{(2\omega)} = \hat{e}_{R10} E_{R10}^{(2\omega)} e^{i(\mathbf{k}_{f0} \cdot \mathbf{r} - 2\omega t)}, \quad (2.27)$$

where  $\hat{e}_{R10}$  is the unit vector in the direction of  $\mathbf{E}_{R10}^{(2\omega)}$ . The wavevector of the reflected SH,  $\mathbf{k}_{f0}$ , has the same direction as the reflected fundamental field and the magnitude of  $\mathbf{E}_{R10}^{(2\omega)}$  is determined using standard boundary conditions at the interface, i.e.

continuity for the tangential components of the electric and the magnetic fields. The s-polarized component of  $\mathbf{E}_{R10}^{(2\omega)}$ , i.e.  $E_{\perp,R10}^{(2\omega)}$ , is proportional to the component of P along the  $y$ -axis in medium 1,  $P_{\perp,1}$ , (see Appendix B). In particular we have

$$E_{\perp,R10}^{(2\omega)} = \frac{4\pi P_{\perp,1}}{\epsilon_{b1} - \epsilon_{f1}} \left[ \frac{k_{f1,z} - k_{b1,z}}{k_{f1,z} - k_{f0,z}} \right]. \quad (2.28)$$

Here,  $k_{ij,z}$  is the  $z$  component of  $\mathbf{k}_{ij}$  and  $\epsilon_{bj}(2\omega) = \epsilon_j(\omega)$ ,  $\epsilon_{fj}(2\omega) = \epsilon_j(2\omega)$ , and  $\epsilon_j(\omega)$  is the  $\omega$ -dependent linear dielectric constant of medium  $j$ . Conservation of  $k_{\parallel}$  at all frequencies ( Snell's law) enables one to determine the components of each wavevector as a function of the incident wavevector.

For zinc blende crystals such as GaAs(001) and ZnSe(001) in the p-in/s-out polarization configuration, the second-order bulk polarization has the form

$$P_{\perp,1}^{(2\omega)} = \frac{-k_{t1,z} k_{t1,x}}{k_{t1}^2} 2 \cos(2\phi) t_{\parallel,01}^{(\omega)2} \chi_{xyz}^{(2)} E_{\parallel}^{(\omega)2}, \quad (2.29)$$

where  $t_{\alpha,ij}^{(\omega)}$  ( $r_{\alpha,ij}^{(\omega)}$ ) is the Fresnel refraction (reflection) coefficient for an  $\alpha$ -polarized light beam with angular frequency  $\omega$  propagating from medium  $i$  to medium  $j$ , and  $E_{\parallel}^{(\omega)}$  is the component of the incident p-polarized input field parallel to the plane of incidence.  $k_{t1,z}$  and  $k_{t1,x}$  are the  $z$  and  $x$  wavevector components, respectively, of the transmitted fundamental field in medium 1. Using Eqs. (2.28) and (2.29) we have

$$E_{\perp,R10}^{(2\omega)} = \chi_{xyz}^{(2)} Y E_{\parallel}^{(\omega)2}, \quad (2.30)$$

where

$$Y = \frac{-k_{t1,z} k_{t1,x}}{k_{t1}^2} \frac{4\pi}{\epsilon_{b1} - \epsilon_{f1}} \frac{k_{f1,z} - k_{b1,z}}{k_{f1,z} - k_{f0,z}} 2 \cos(2\phi) t_{\parallel,01}^{(\omega)2}. \quad (2.31)$$

The coefficient  $Y$  depends only on the linear properties of the bulk medium and can be calculated. Using a calculated  $Y$  and measured  $|\mathbf{E}_{L,R10}^{(2\omega)}|^2$  we can determine  $|\chi_{xyz}^{(2)}|$ . In Fig. 2.5 and Fig. 2.6 we plot measured values of  $|\mathbf{E}_{L,R10}^{(2\omega)}|^2$  and  $|\chi_{xyz}^{(2)}|$  for GaAs(001), respectively.

The  $E_0$  transition of GaAs is responsible for the small peak at 1.4 eV shown in Fig. 2.5. The GaAs peak is less pronounced than the ZnSe because the joint density of states (JDOS) at the  $\Gamma$  point in GaAs is  $\sim 20$  smaller than in ZnSe. Previous measurements of  $\chi_{xyz}^{(2)}$  in GaAs [47, 48, 49, 50] did not exhibit the  $E_0$  transition of this semiconductor. This may have been a result of poor resolution of the apparatus and/or sample quality. The broad peak at  $\sim 2.96$  eV in Fig. 2.6 corresponds to the  $E_1$  transition of GaAs.

In some physical situations the magnitude of the second-order susceptibility can vary as a function of position within the semi-infinite medium. This can arise as a result of local stresses or electric fields near the interface. In Appendix C we give a solution for the special case where the susceptibility decays exponentially with distance from the vacuum/crystal interface.

Table 2.1: Angular dependence of  $P^{(2\omega)}$  for  $\bar{4}3m$  and  $C_{4v}$  symmetry.

Polarization	$C_{4v}$	$\bar{4}3m(001)$
$P_{\text{in}}/P_{\text{out}}$	$2\chi_{113}E_1E_3\hat{x} + (\chi_{311}E_1^2 + \chi_{333}E_3^2)\hat{z}$	$-\chi_{123}(2E_1E_3\hat{x} + E_1^2\hat{z})\sin(2\phi)$
$P_{\text{in}}/S_{\text{out}}$	0	$2\chi_{123}E_1E_3\cos(2\phi)\hat{y}$
$S_{\text{in}}/P_{\text{out}}$	$\chi_{311}E_2^2\hat{z}$	$\chi_{123}E_2^2\sin(2\phi)\hat{z}$
$S_{\text{in}}/S_{\text{out}}$	0	0

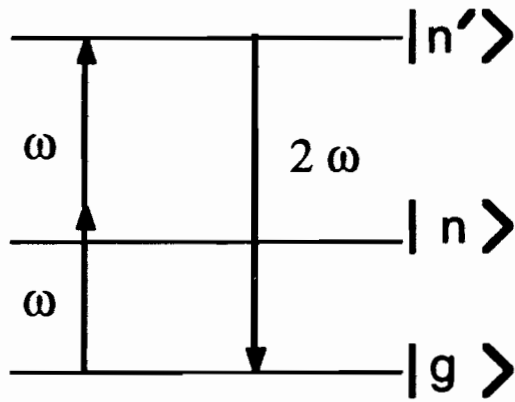


Figure 2.1: A possible mixing process in a three-level system.

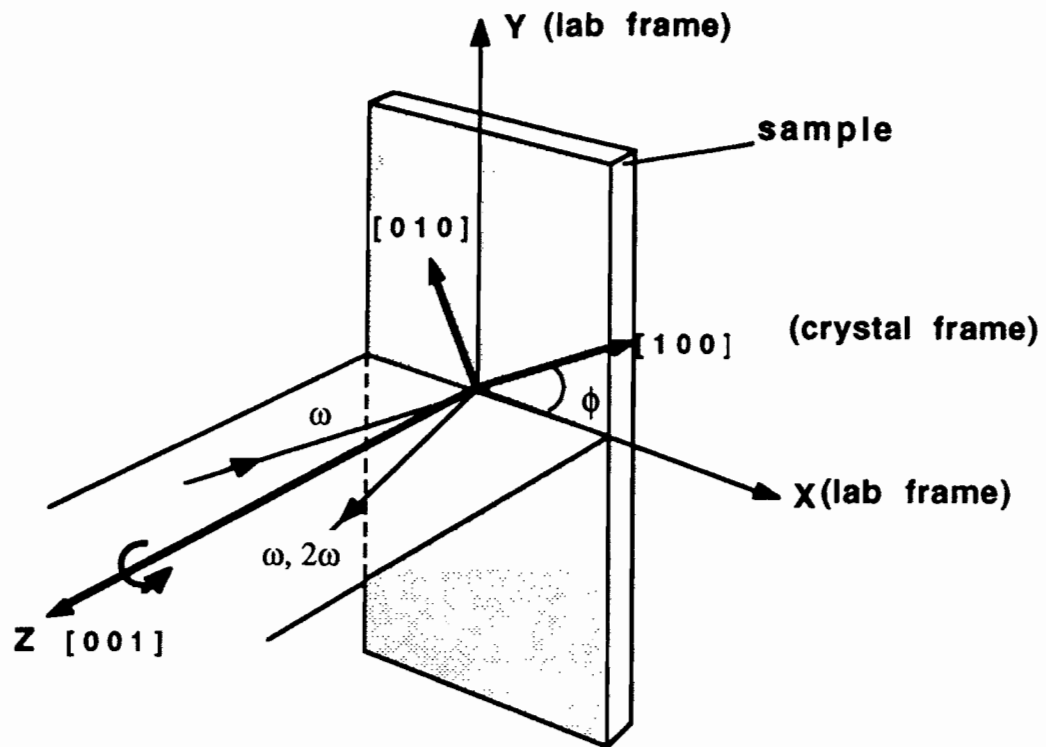


Figure 2.2: A simplified schematic of crystal and lab frames. The  $\hat{z}$ -axis is common in both frames.

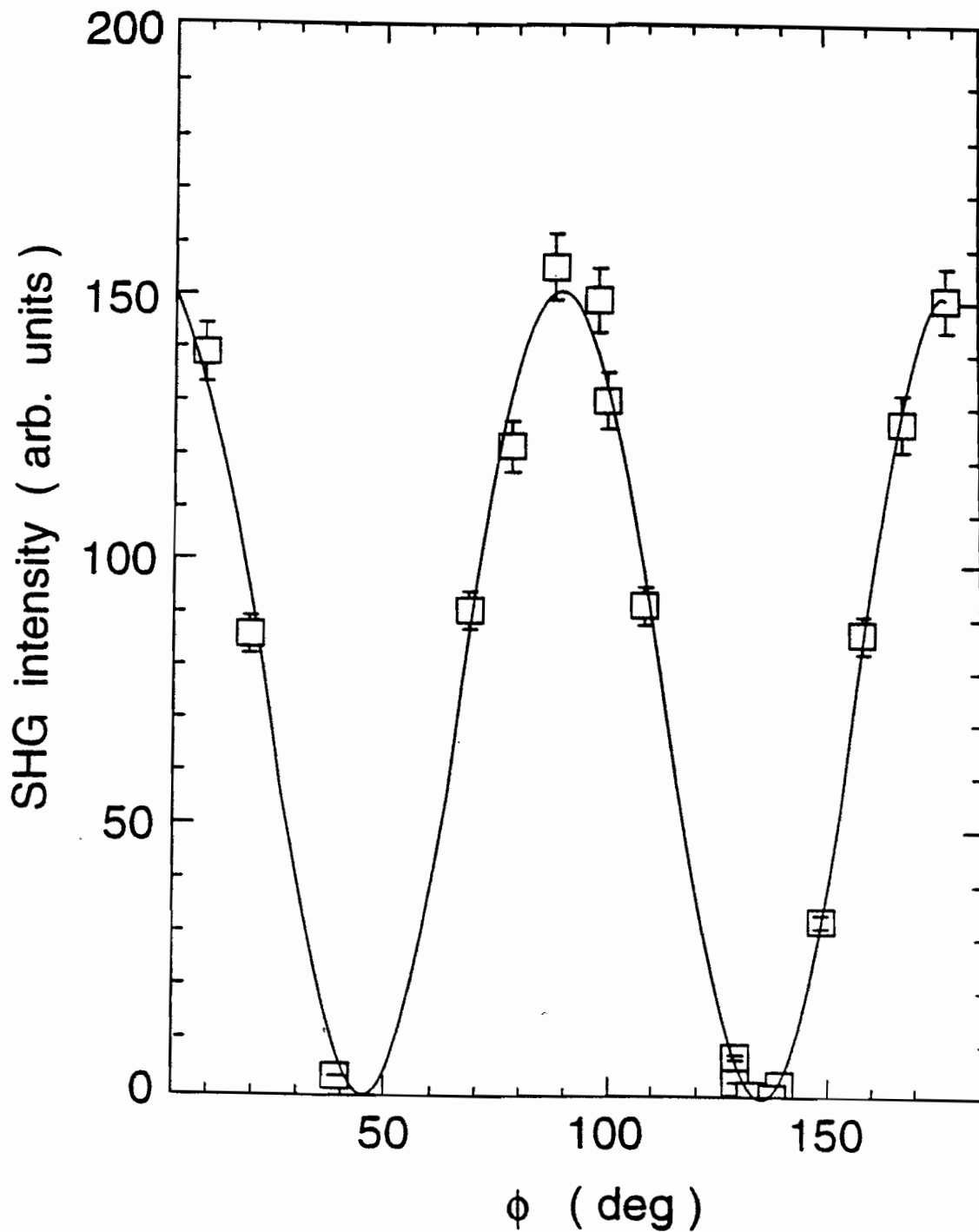


Figure 2.3: Reflected SHG intensity at a fixed frequency from the ZnSe/GaAs(001) crystal as a function of rotation angle  $\phi$  (degrees). Here  $\phi$  is the angle between the [100] direction and the plane of incidence. The input is p-polarized and the output is s-polarized. The ratio of the peak signal to the null signal is  $\geq 5000$ . The solid line is a theoretical prediction of this signal variation.

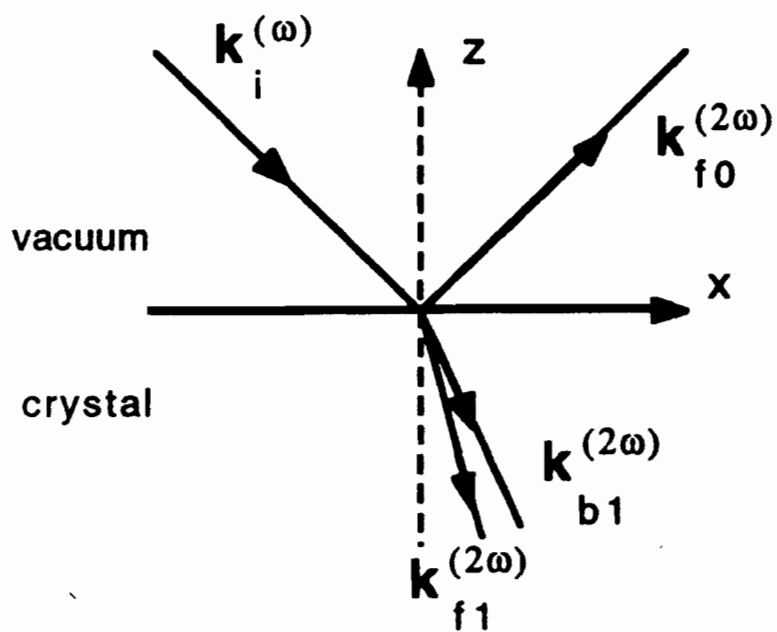


Figure 2.4: Simplified coordinate system that defines the boundaries and the direction of fundamental and second-harmonic electric fields for the case of a semi-infinite slab. All angles between the wavevectors and the  $z$ -axis are positive and less than  $90^\circ$ .

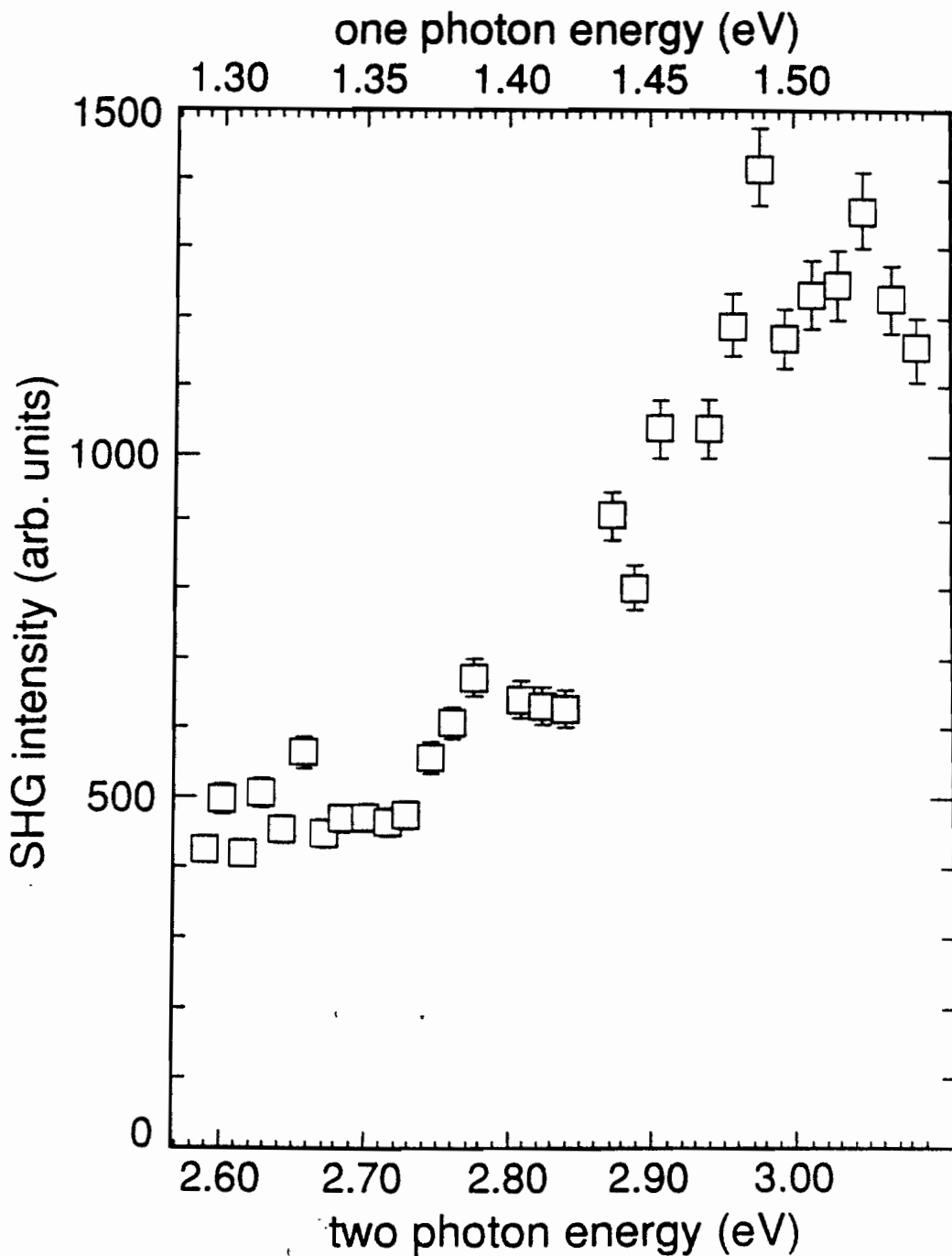


Figure 2.5: Normalized bulk SHG intensity of GaAs(001) as a function of one- and two-photon energy. The error bars represent the range of values obtained from several measurements.

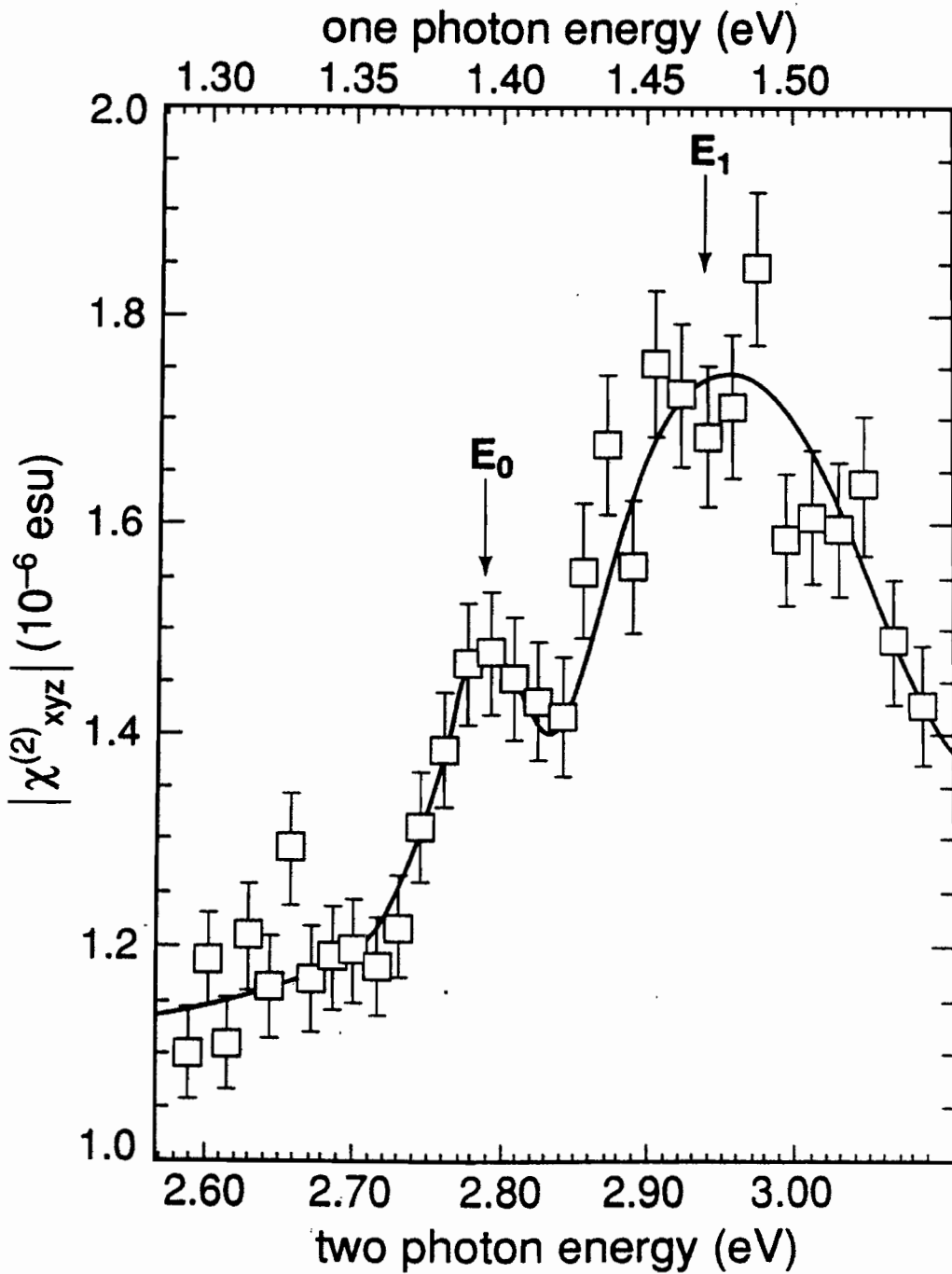


Figure 2.6:  $|\chi_{xyz}^{(2)}|$  as a function of one and two photon energy for GaAs as derived from data on the previous page. The  $E_1$  and  $E_0$  peaks correspond to a two- and a one-photon resonances at  $\sim 2.96$  eV and  $\sim 1.4$  eV, respectively. The solid line is only a guide for the eye.

# Chapter 3

## Experimental

In this chapter we discuss the generation and detection of SF and SH signals as a function of time, azimuthal angle, and more importantly, frequency. Since the key to accurate nonlinear spectroscopic studies is the correct experimental set-up, a detailed description of our experimental arrangements is necessary. The layout of the experimental set-up is shown in Fig. 3.1 and 3.2.

### 3.1 Optical Arrangements

A rough schematic of the optical set-up for SHG and SFG is shown in Fig. 3.1. In these experiments polarized beams of laser light with frequencies of  $\omega_1$  and  $\omega_2$  are sent to a sample where photons with frequency of  $\omega_3 = \omega_1 + \omega_2$  are generated. Then, the fundamental photons are stopped by a spectral filter and the intensity of the second-order field is measured.

Second-order nonlinear optics requires a field of  $\sim 1$  KV/cm [51] which corresponds to a beam intensity of  $2.7$  KW/cm<sup>2</sup>. This high intensity can only be achieved by a laser. In our work we have used several lasers which are shown in a more detailed schematic of our apparatus in Fig. 3.2.

In our experiments the main laser was a DCR-3 Nd:YAG, made by Spectra-Physics. It produced pulses of 10 nsec in duration at a 10 Hz repetition rate. The average power of the 1064 nm output of this laser was  $\sim 900$  mJ/pulse. A heated phase-matched KDP SH crystal with an efficiency of 45% was used to generate pulses at 532 nm. The output of the Nd:YAG laser had a fixed frequency and could only produce its harmonic using nonlinear crystals. Therefore, it was not tunable and could not be used for spectroscopy. However, this output could be used to pump a dye laser, which is a tunable light source.

Our dye laser was a Spectra-Physics PDL-2, and it was pumped by the output of the Nd:YAG laser at 532 nm. The schematic of this laser is shown in Fig. 3.3. A PDL-2 dye laser consists of an oscillator, pre-amplifier, and amplifier. We were able to cover a broad range of frequencies using different types of dye materials. Each dye solution covered a short range of energy. For all dyes used, the amplifier was longitudinally pumped, and the oscillator was transversely pumped. A typical output spectra of this laser with LDS751 dye is shown in Fig. 3.4.

A standard 532 nm pumped PDL-2 dye laser can cover a range of 1.38 eV (900 nm) to 2.22 eV (560 nm), but the most interesting part of the spectra in our case was

in the range of 900 nm to 1000 nm. To generate such an output we have modified our PDL-2 dye laser with a new grating from Milton Roy Co. This grating contains 1200 grooves/mm with efficiency greater than 70 % in the red-IR. With this grating and using the pre-amp, the LDS925 Exciton dye can cover a range of 905 nm to 970 nm. It was determined through trial and error that 144 mg/l and 10 mg/l of this dye in methanol for the oscillator and for the amplifier, respectively, gave optimal output power. The power spectra of this dye is shown in Fig. 3.5.

Here we will describe the optical arrangement which was used to send the output of the dye laser to the sample for use in optical spectroscopy. The output of the dye laser was first collimated and then sent into the far field in order to spatially filter out the hot spots in the beam. This prevented sample damage. In the SFG experiments the remainder of the 1064 nm output of the Nd:YAG laser had to be sent to a delay line for temporal matching with the dye laser output. After filtering, the beam was again collimated and sent to a wedged fused silica beam splitter. The beam splitter sent  $\sim 10\%$  of the total intensity to a wedged quartz plate for normalization purposes. Because our experiments utilize the P-in/S-out polarization configuration, and the dye laser output is S-polarized, the polarization of the dye laser beam needed to be rotated by 90 degrees. This was accomplished by using a prism combination and a polarizer in the sample line. The prism combination is shown in Fig. 3.6. The beam was then passed through a spectral filter to stop any background light at  $2\omega$  before illuminating the sample.

The angle of incidence was  $75^\circ$ . At this angle,  $> 50\%$  of the fundamental light was transmitted into the ZnSe overlayer. The collimated beam was  $\sim 1.5$  mm in diameter and had a fluence of  $\sim 5$  mJ/cm<sup>2</sup>. This fluence could produce a SHG signal on average of  $\sim 50$  photons/laser pulse and signal/background of  $\sim 100$ . The background signal was measured by blocking the laser beam and the value of signal/background was obtained by averaging over 1000 laser pulses. The reflected SH or SF beam of the sample was accompanied by the fundamental beam with an average of  $\sim 10^{16}$  photons/pulse. To stop the fundamental we used a monochromator and spectral filters. The filters attenuate the fundamental beam by 12 orders of magnitude. A polarizer was used to select the polarization state of the SF or SH signal. The output of the polarizer was focused with a UV enhanced quartz lens to the slit of a Jarrel Ash Mono Spec 18 monochromator. To eliminate background UV, another spectral filter was used at the entrance slit of the monochromator. The SF and SH light was then detected at the exit slit of the monochromator by a Hamamatsu R943-02 photomultiplier tube. The alignment and position of the beam on the sample was monitored using a video camera and TV monitor.

## 3.2 Normalization

In chapter 2 we saw that the SH intensity was related to the square of the laser intensity. Systematic and uncontrolled variations in intensity must be compensated as a function of frequency and time. We have measured the SH or SF intensity of a

well-known nonlinear crystal and used it to normalize the SH or SF intensity of the sample. This procedure is essential because:

1- At a fixed frequency both the spatial and temporal beam profile of the laser fluctuate. This affects the signal to noise ratio of the SH results.

2- The power of the dye laser is a strong function of frequency. Without the correct normalization, this frequency dependence of power introduces a false structure in to the spectra.

These variations call for a reference sample and a reference arm with the following specifications:

a- The nonlinear output of the reference sample must be well understood and should be free of spectral structures.

b- The beam splitter must be an equal distance from both the sample and reference. This assures that both the sample and the reference are illuminated by the same beam spatial profile.

c- The reference and sample arms must be identical; that is, all optics in both arms must have the same *spectral* specifications.

d- Because of the polarization dependence of the monochromators, both the reference and the sample monochromator must detect the same polarization output.

Our reference was a y-cut (i.e. the y-axis was normal to the face of the crystal) wedged quartz plate. This face of the crystal was used for the following reasons. This face of the crystal, in contrast to z-cut quartz, does not have any optical activity,

and since  $\chi_{ijk}^{(2)}$  of a quartz crystal does not couple to the  $z$ -direction of an electric field, the birefringence property of a  $y$ -cut crystal does not effect the SHG output. However, the reflected SH and SF of quartz is quite small, and the transmitted SH or SF signal had to be used.

At each frequency we have normalized the sample signal to the maximum SH or SF output of the reference. Because of phase matching and interference, the transmitted SH intensity of the reference sample oscillates as a function of the angle of incidence (Maker fringes [52]) and the fundamental frequency. We could not maximize the signal by changing the angle of incidence at each frequency. This results from the fact that the maximum is not a simple function of fundamental intensity. To demonstrate this fact, we studied the output transmitted intensity of a quartz plate. Details are given in Appendix E; the result is

$$E_{Trans.}^{(2\omega)} = Q \left\{ -\frac{2\sqrt{\epsilon_{f1}} \cos \theta_{f1} [\cos \theta_i + \sqrt{\epsilon_{b1}} \cos \theta_{b1}]}{[\sqrt{\epsilon_{f1}} \cos \theta_{f1} + \cos \theta_i]^2} e^{id(k_{0,z} - k_{f1,z})} + \frac{\sqrt{\epsilon_{f1}} \cos \theta_{f1} + \sqrt{\epsilon_{b1}} \cos \theta_{b1}}{\sqrt{\epsilon_{f1}} \cos \theta_{f1} + \cos \theta_i} e^{id(k_{0,z} - k_{b1,z})} \right\} \quad (3.1)$$

A description of the parameters is given in Chapter 2. Using Eq. ( 3.1) we have plotted the SH intensity as a function of the angle of incidence for two different input frequencies in Fig. 3.7. The fundamental intensity is the same for these two cases.

One can readily see that the position of the intensity maxima is shifted, and also that the maxima have different values. This is due to the fact that the envelope function of the Maker fringes is not a flat curve. It demonstrates that two input beams, with the same intensity, but different frequencies could result in different

output intensities. We must remember that *this frequency dependence is not due to the band structure of quartz but is due to the interference.*

We simply need to flatten the envelope function of the Maker fringes to solve this problem. This can be achieved by using a *wedged* quartz plate with a small apex angle. With this condition the beam impinges on the plate at normal incidence and the fringes result by translation of the plate normal to the beam direction. The resultant SH intensity for two input beams with the same intensity is shown in Fig. 3.8. The plot shows that even though the position of the maxima is not constant, the envelope is flat and all of the maxima are at the same value. In this case we can simplify Eq. ( 3.1) to

$$I^{(2\omega)} = C_1^2 + C_2^2 + 2C_1C_2 \cos(d\Delta\phi) \quad (3.2)$$

where

$$C_1 = Q \frac{-2\sqrt{\epsilon_{f1}}[1 + \sqrt{\epsilon_{b1}}]}{[\sqrt{\epsilon_{f1}} + 1]^2}, \quad (3.3)$$

$$C_2 = Q \frac{\sqrt{\epsilon_{f1}} + \sqrt{\epsilon_{b1}}}{\sqrt{\epsilon_{f1}} + 1} \quad (3.4)$$

and

$$\Delta\phi = (k_{f1,z} - k_{b1,z}). \quad (3.5)$$

This also shows that the minimum of the intensity for the quartz crystal is zero (see Fig. 3.8).

### 3.2.1 Beam Size Effect

The finite size of the beam width also introduces a complication to the output power of the reference. Each section of the beam travels a different length in the plate, which affects the amplitude of the output intensity. However, this effect does not introduce any new systematic on our normalization procedure. To calculate this effect we approximate the beam profile by a disk of constant intensity and diameter  $w$ . Thus, the total intensity is approximately equal to the integration of  $I^{(2\omega)}$  over the disk area; that is

$$I_{total} = \int_{area} \{C_1^2 + C_2^2 + 2C_1C_2 \cos[\Delta\phi(R\alpha \cos \theta + l_o)]\} da \quad (3.6)$$

where  $l_o$  is the thickness of the crystal at the center of the disk. With proper choice of coordinates, this reduces to

$$I_{total} = (C_1^2 + C_2^2)\pi\left(\frac{w}{2}\right)^2 + 4C_1C_2\left(\frac{w}{2}\right)^2\Phi \quad (3.7)$$

where

$$\Phi = \int_0^\pi \cos[\Delta\phi(R\alpha \cos \theta + l_o)] \sin^2 \theta d\theta \quad (3.8)$$

A plot of  $\Phi$  as a function of  $l_o$  is shown in Fig. 3.9. It is evident from this plot that the minimum of the fringes for the quartz crystal is non-zero since the value of  $\Phi$  is too small. This can be seen more clearly if we approximate  $C_1 = -C_2$ .

### 3.3 Samples

Our heterostructure sample consists of an epitaxial layer of undoped ( $n \leq 1 \times 10^{15} \text{ cm}^{-3}$ ) ZnSe[001], with thickness ranging from 50 Å to 1  $\mu\text{m}$ , grown on a 0.5  $\mu\text{m}$  undoped ( $n \leq 5 \times 10^{15} \text{ cm}^{-3}$ ) GaAs film, terminated with a 2x4 surface reconstruction (see Fig. 3.10). The films were grown by molecular beam epitaxy (MBE) on a  $n^+$  silicon doped GaAs substrate in a MBE dual chamber at Bellcore [65]. One chamber was designed for the growth of GaAs and the other was used to grow the ZnSe overlayer. These two growth chambers were connected by UHV transfer modules. Our only 3x1 buried GaAs surface reconstructed sample consisted of a 215 Å ZnSe overlayer; the procedure used to grow this sample is explained in reference [27]. At present there is substantial technological interest in the ZnSe/GaAs heterostructure, because ZnSe has been demonstrated to lase at  $\sim 2.67 \text{ eV}$ [26]. As a result of this interest our samples have been well characterized morphologically, chemically, and to some extent electrically [53].

### 3.4 Data Acquisition

The output of the reference PMT was sent directly to a Stanford Research Boxcar Averager model SR250, but the output of the sample PMT was first amplified using a Canberra Timing Filter Amplifier model 2111, and then sent to another Boxcar. The Boxcar averager produced a 10 nsec gate for the integration of the signals. To have

an active background subtraction, we triggered the boxcar at 20 Hz, twice the laser repetition rate, with an electrical frequency doubler (see Fig. 3.11), and operated the boxcar in toggle mode. In toggle mode the boxcar averager assigned an alternative sign to each incoming signal. With a 10 Hz signal, the boxcar averager received a signal and then received the background 50 msec after. In toggle mode, all signals carried the same sign, and all backgrounds carried the opposite sign; in this way the average dc output was proportional to the signal minus the background. The dc output of the boxcar was digitized using an A-D converter in a SR245 Stanford Research computer interface, and then sent to a AT&T 6321 WGS computer. The computer interface communicated with the computer through a National Instrument GPIB board.

With the "sampling" setting on the boxcar averager set on 100, the output dc voltage was a dynamical average of 100 laser shots. Using this set-up, total of 5000 shots were averaged for both the reference and the sample. For each data point on the spectra, the dye laser monochromator was set at the desired wavelength, then both sample and reference monochromators were optimized, and the wedged quartz plate was moved for maximum SH output before the data acquisition began. This procedure was repeated to cover all wavelengths available in the range of the particular dye. The entire operation was automated using computer controlled stepper motors. The programs were written in ASYST. Figs. 3.12 and 3.13 show a schematic of the stepper motor and a typical SH spectra, respectively. The error bars in Fig.

3.13 represent the range of values obtained from several measurements.

## 3.5 Other Optical Methods

We have also measured linear reflectivity as a function of wavelength and the angle of incidence to characterize our samples. These two techniques are briefly described here. The formulation for these techniques is given in Appendix F.

### 3.5.1 Linear Spectroscopy

It has been seen that the accurate interpretation of nonlinear optical results is highly related to the correct knowledge of the linear properties of the sample. One of these properties is the dielectric constant. These data were available for ZnSe and GaAs in the literature [54, 55, 56, 57]. We checked the accuracy and applicability of these data for our systems by performing linear spectroscopy experiments. The schematic for the linear reflectivity experiments is shown in Fig. 3.14. The light source in these experiments was a tungsten and  $D_2$  lamp-monochromator-chopper and the signal detector was a silicon photodiode and a lock-in amplifier. The results of the samples with various thicknesses are shown in Fig. 3.15. There was good agreement between our calculation based on Eq. (F.3) and the experimental results. This indicated that the values for the dielectric constant in reference [54, 55] were applicable for our samples.

### 3.5.2 Thickness Measurements

To measure the thickness of the ZnSe overlayer in our heterostructure samples, linear reflectivity experiments were performed as a function of the angle of incidence. In these measurements a HeNe laser in the p-polarization configuration along with a  $\theta - 2\theta$  table was used. A schematic of the experimental arrangement is shown in Fig. 3.16. The experimental result was then fitted to Eq. (F.3) for only one free parameter, thickness. The results for the two samples with thicknesses of 215 Å and 10280 Å are shown in Fig. 3.17.

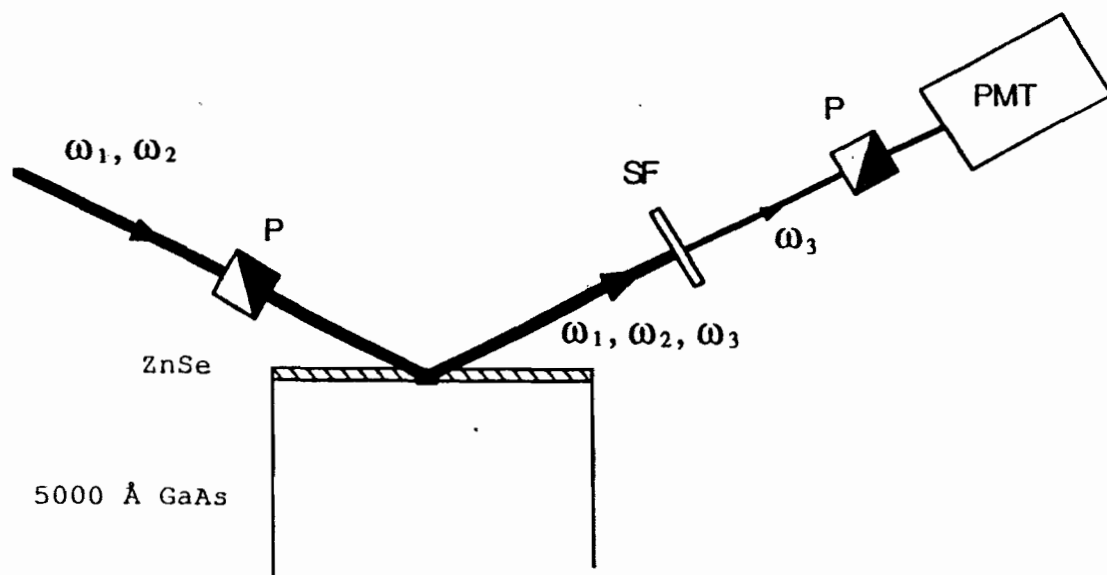


Figure 3.1: A rough schematic of the optical setup for SFG and SHG measurements.

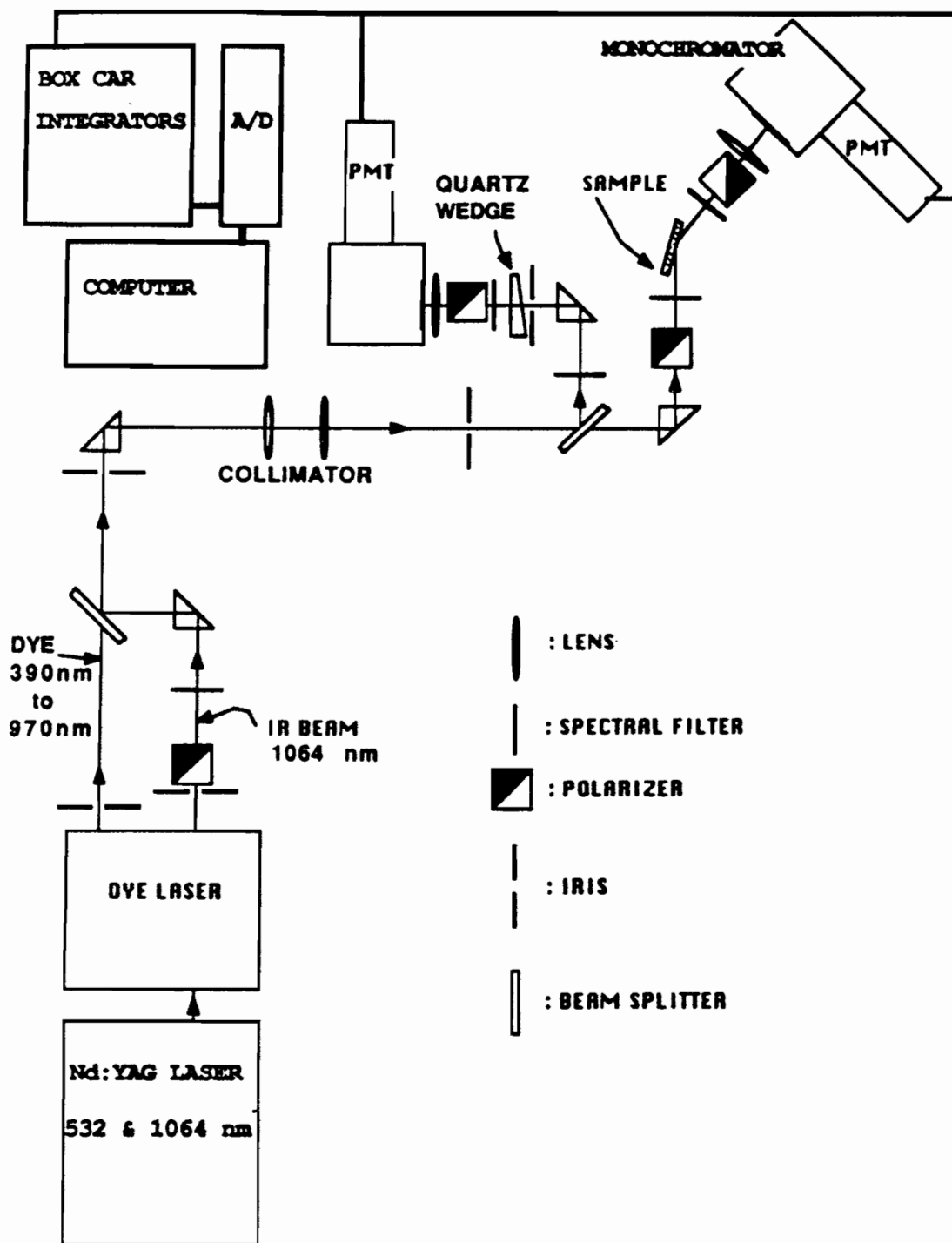


Figure 3.2: Schematic of experimental setup for SFG and SHG measurements.

- |       |                          |   |                                     |
|-------|--------------------------|---|-------------------------------------|
| A,B   | Beamsplitter             | N | 90° Prism                           |
| C     | 90° Prism                | O | 90° Prism for side-pumped amplifier |
| D,E   | Cylindrical Lens         | P | Mirror for side-pumped amplifier    |
| F     | Amplifier Dye Cell       | Q | Lens for side-pumped amplifier      |
| G     | Grating                  | R | Output 90° prism                    |
| H     | Oscillator Dye Cell      | S | Compensator for preamp. cell        |
| I     | Oscillator Output Mirror |   |                                     |
| J     | Preamplifier Dye Cell    |   |                                     |
| K,L,M | Lenses                   |   |                                     |

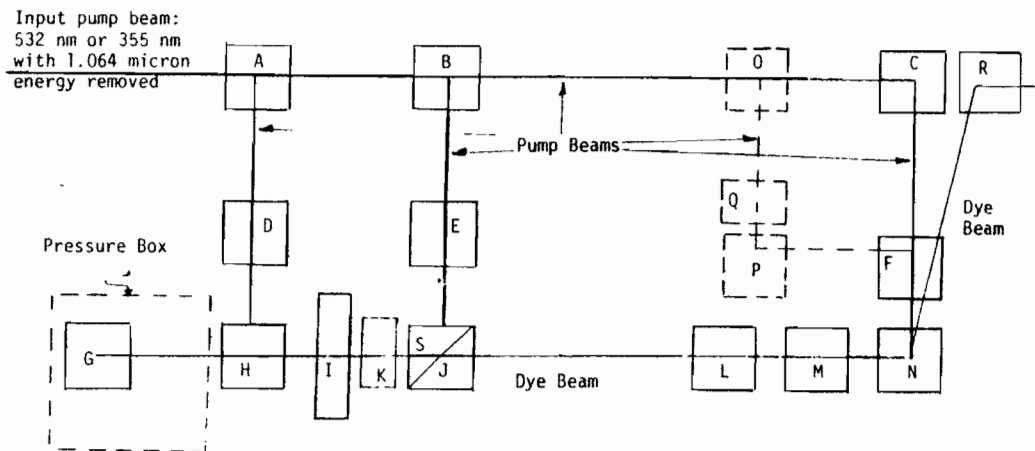


Figure 3.3: A schematic of PDL-2 dye laser. This laser was pumped by the output of the Nd:YAG laser at 532 nm

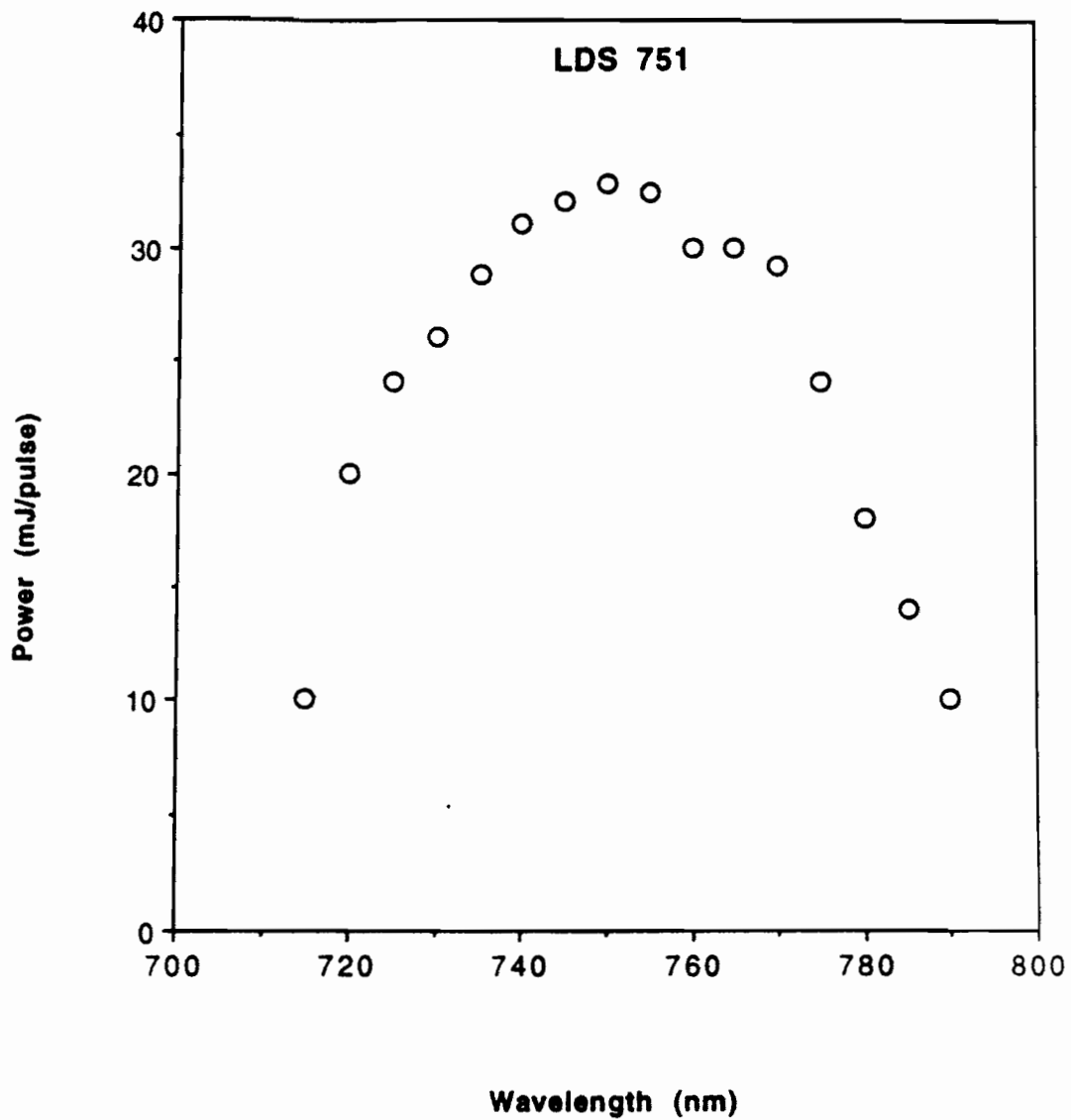


Figure 3.4: A typical power spectra of LDS751 dye.

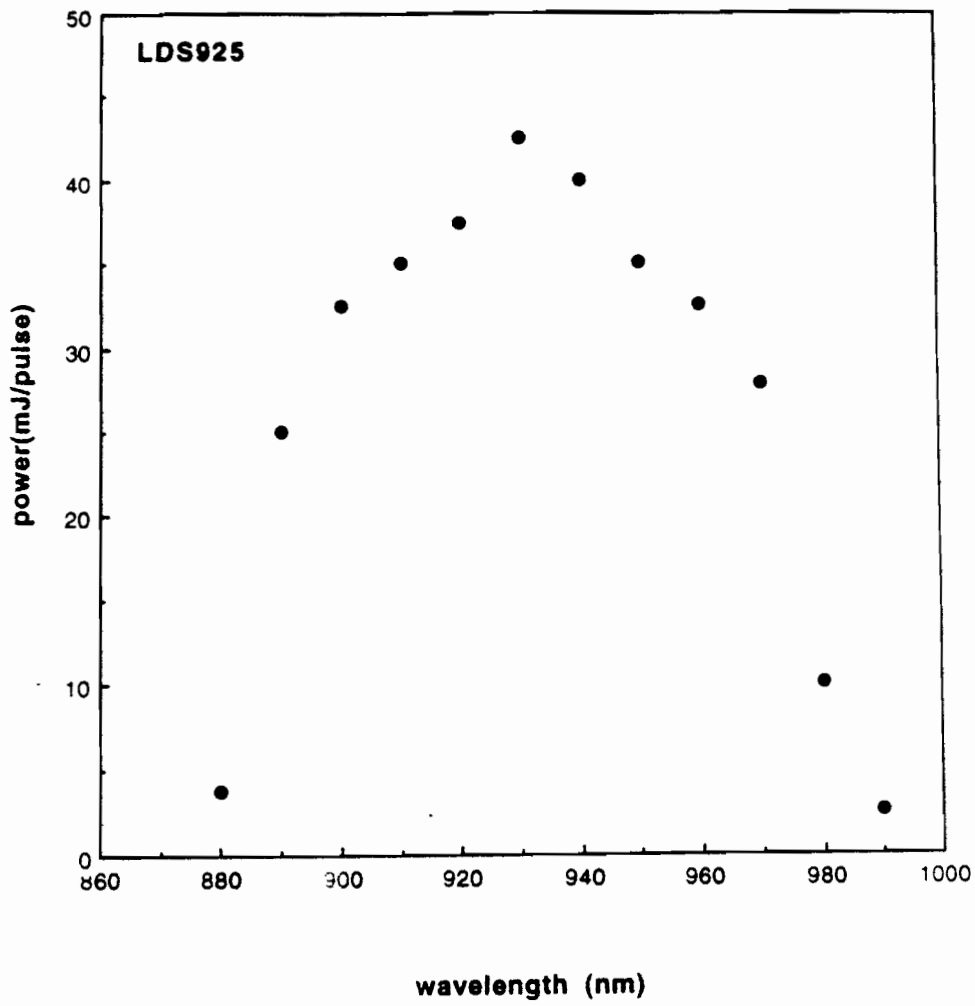


Figure 3.5: A typical power spectra of LDS925 dye.

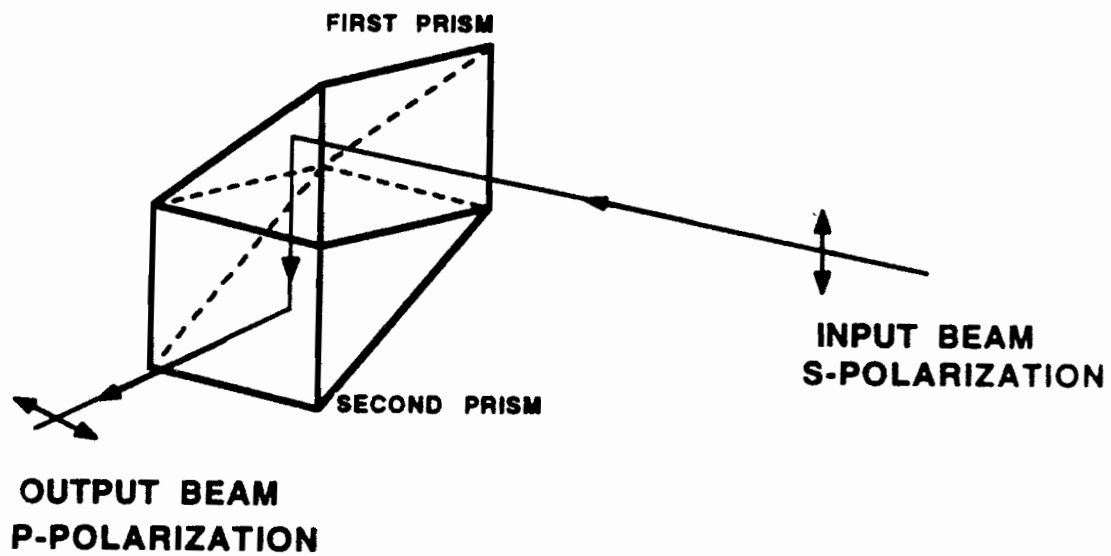


Figure 3.6: A schematic of the prism combination. This combination was used to rotate the polarization by 90 degrees, independent of wavelength.

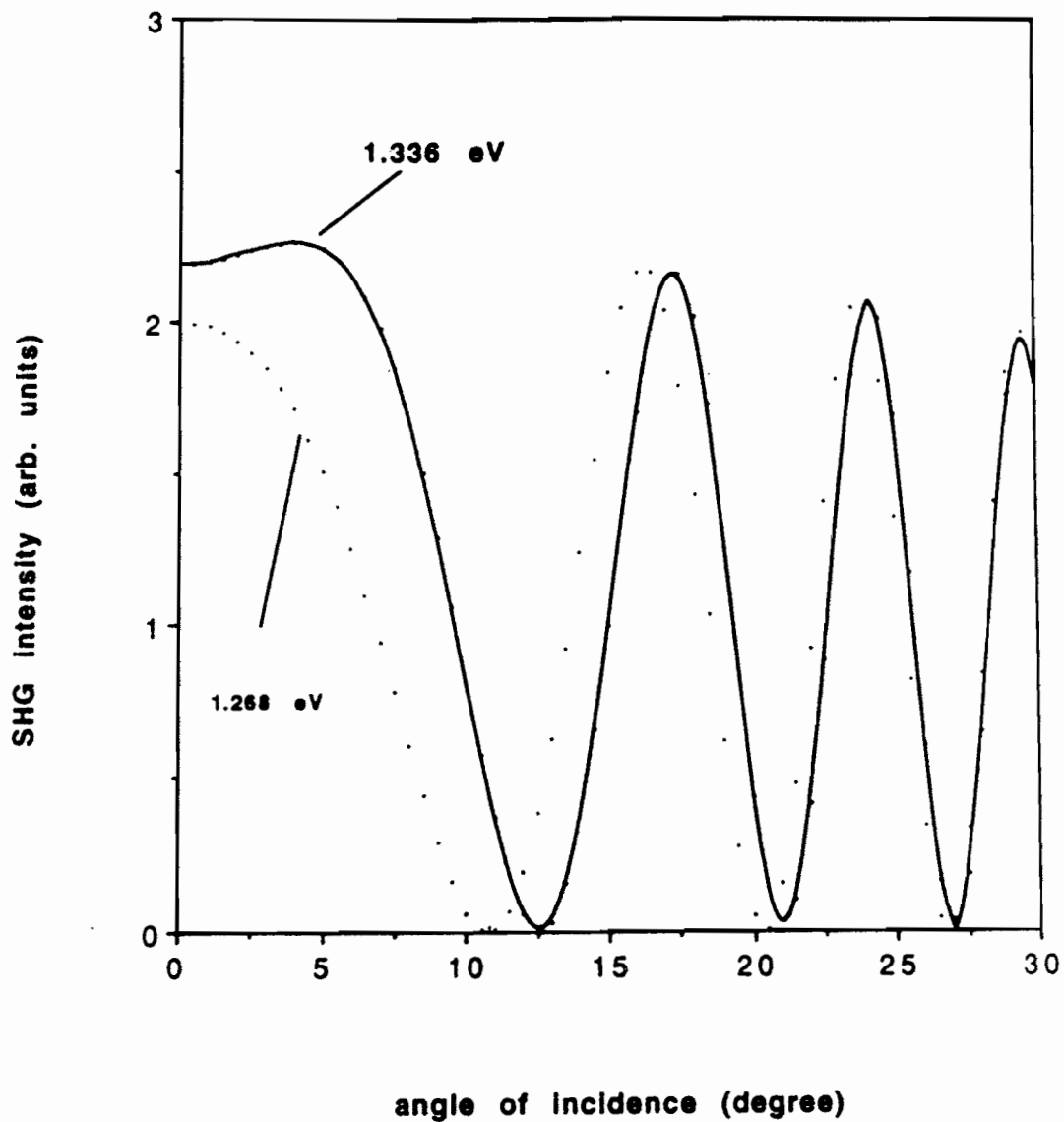


Figure 3.7: The variation in the transmitted SH intensity of a quartz plate as a function of the angle of incidence for two different fundamental frequencies. The intensity of the fundamental beams are the same for both cases. The position and the value of the maxima are different.

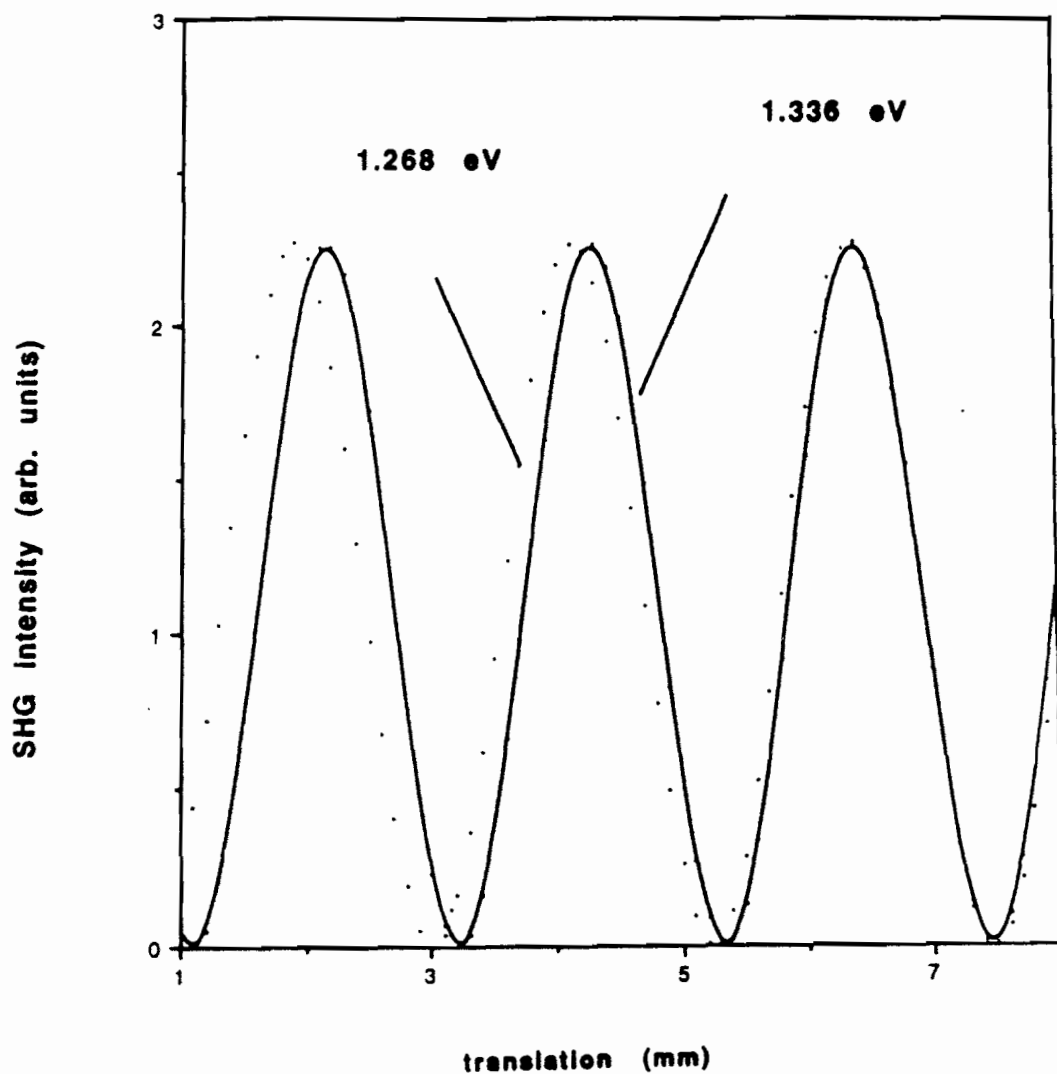


Figure 3.8: The variation in the transmitted SH intensity of a wedged quartz plate as a function of the translation for two different fundamental frequencies. The intensity of the fundamental beams are the same for both cases. Even though the position of the maxima are not fixed, their value is constant.

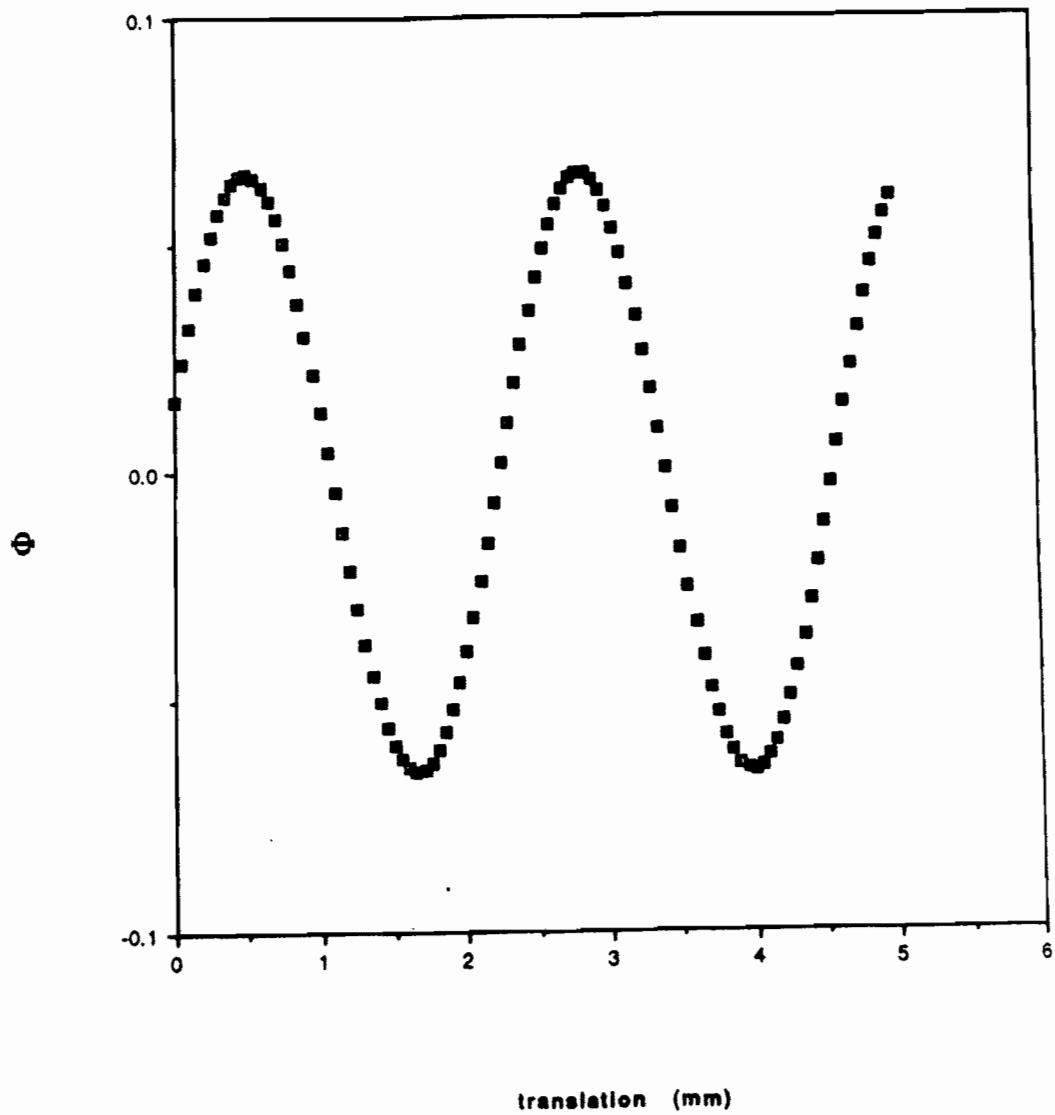


Figure 3.9: Variation of  $\Phi$  as a function of  $l_0$ . The parameter  $\Phi$  was introduced by the finite size of the beam width.

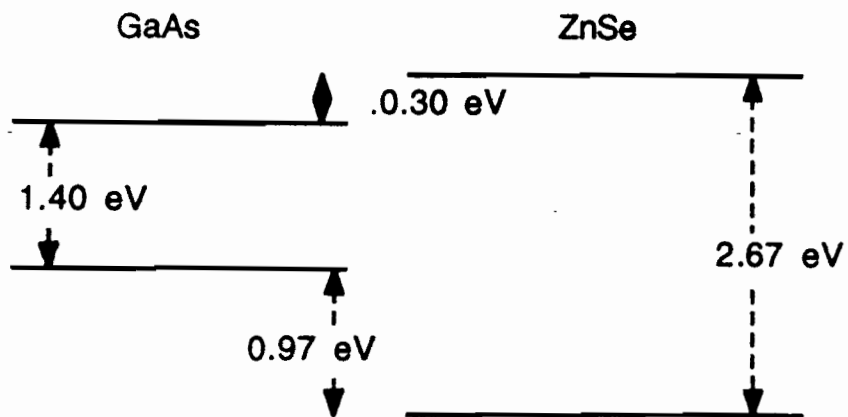
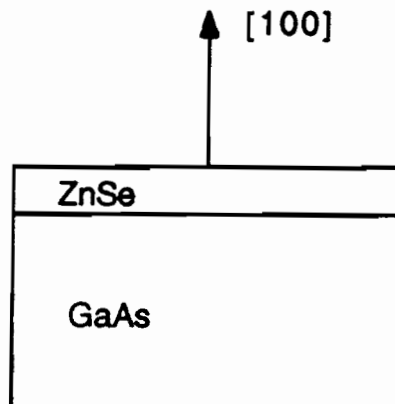


Figure 3.10: The layout of the ZnSe/GaAs(001) sample. The optical band gap of two semiconductors is also shown in the lower portion of the figure.

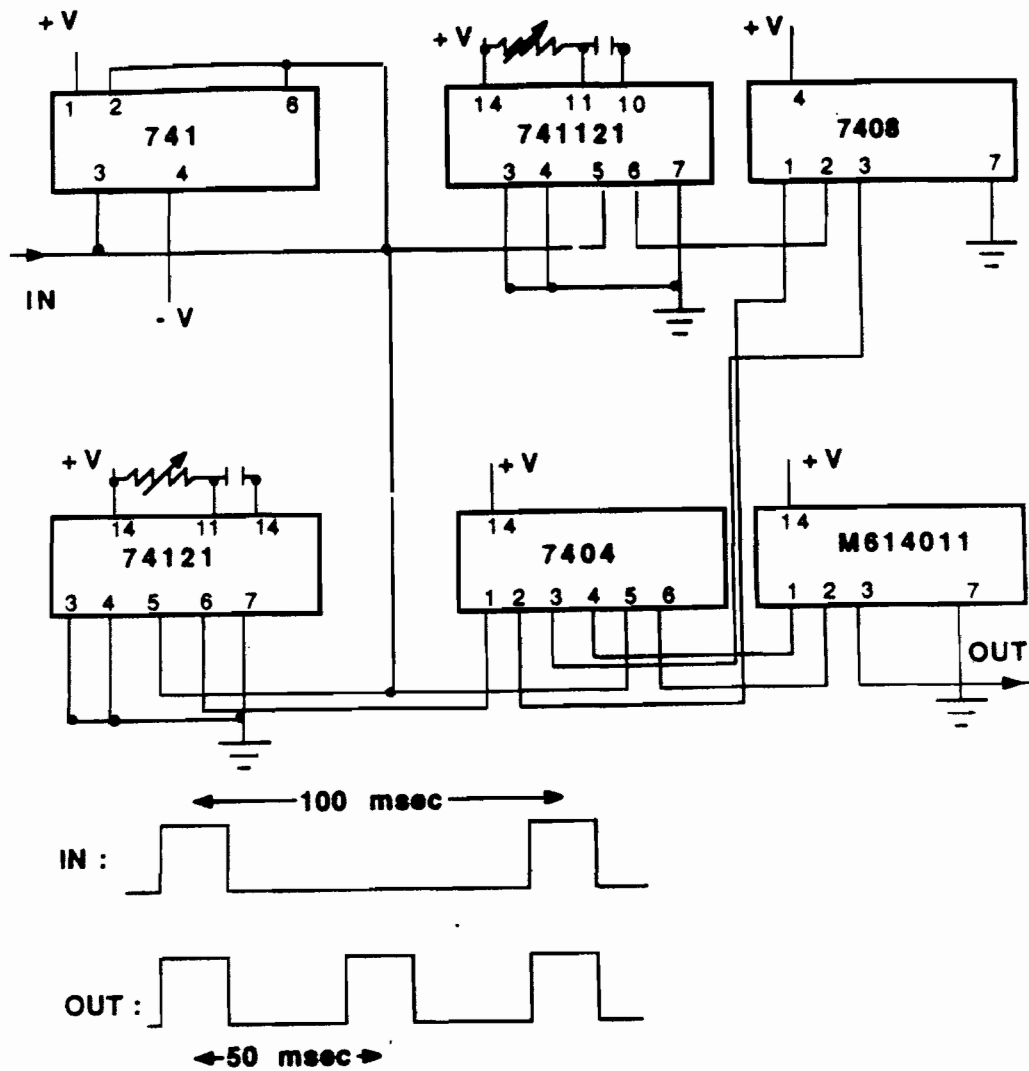


Figure 3.11: A schematic of the frequency doubler. The frequency doubler was used to generate 20 Hz trigger signals for active background subtraction.

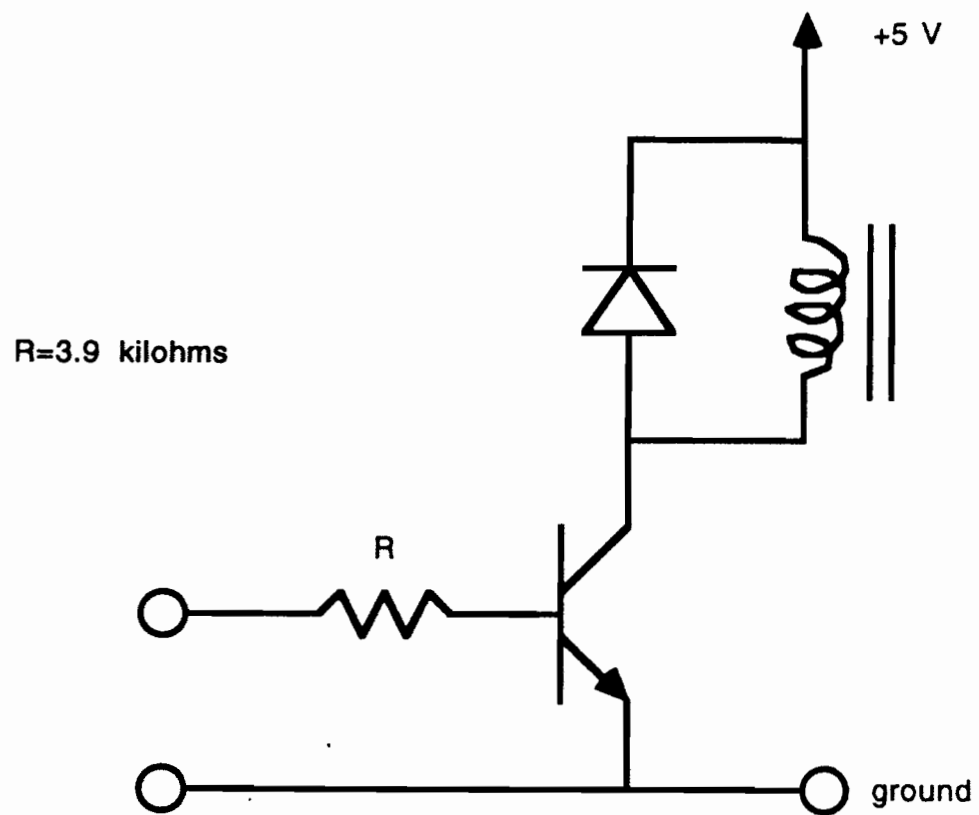


Figure 3.12: Schematic of stepper motor

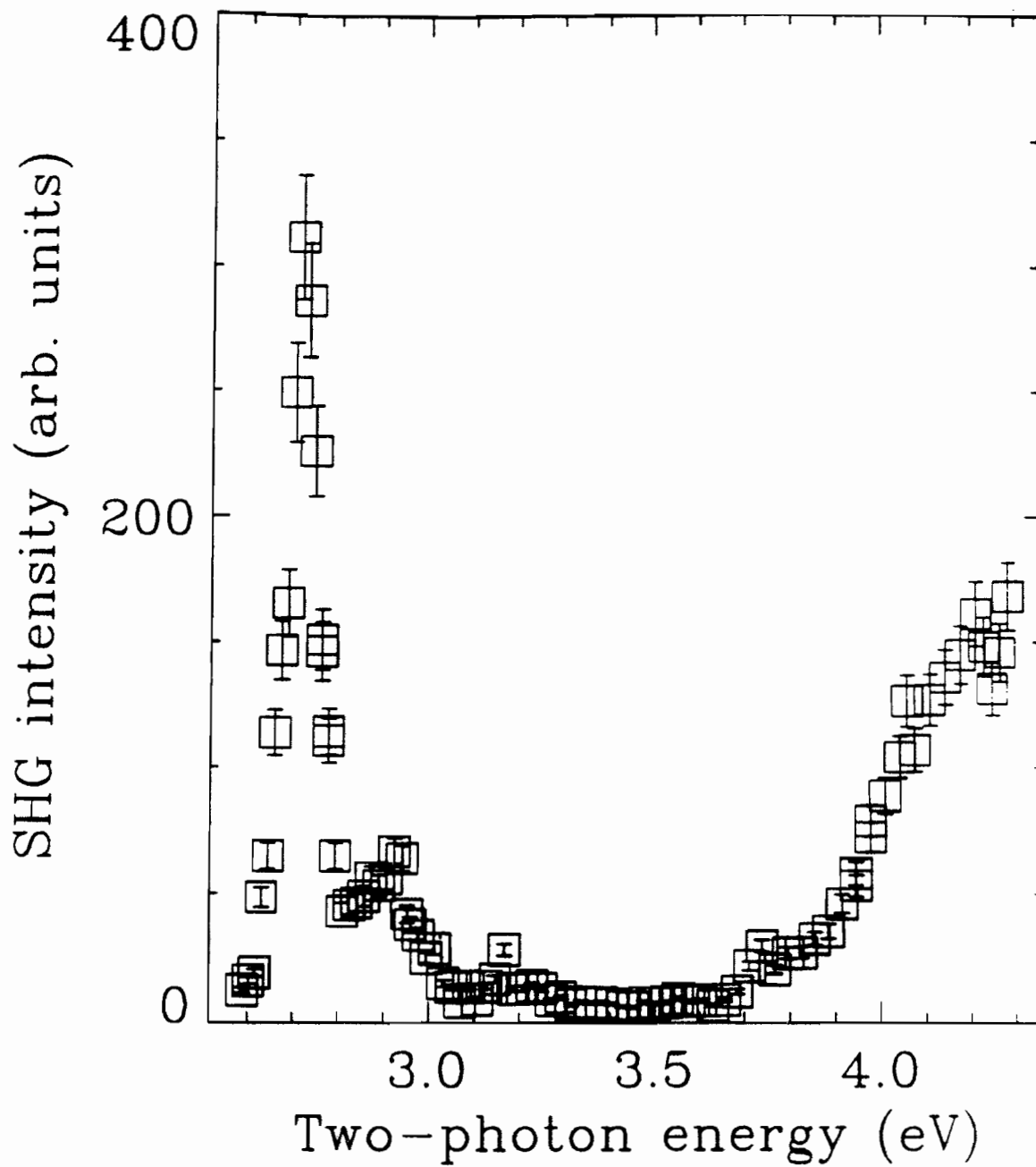


Figure 3.13: A typical interfacial SH spectrum of ZnSe/GaAs(001) heterostructure. The thickness of the overlayer is 215 Å.

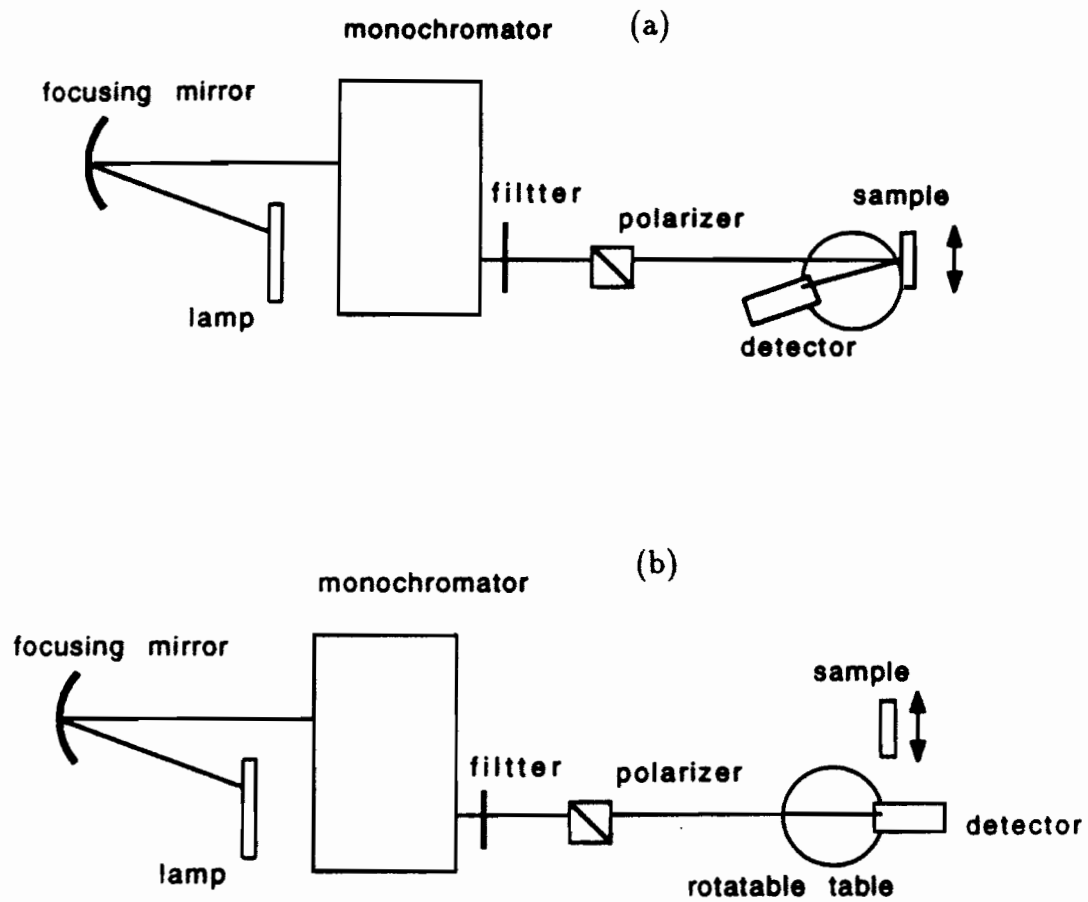


Figure 3.14: Optical setup for linear reflectivity measurements. In these experiments (a) the intensity of the reflected beam from the sample was measured and then (b) the sample was removed and the intensity of the incident beam was recorded.

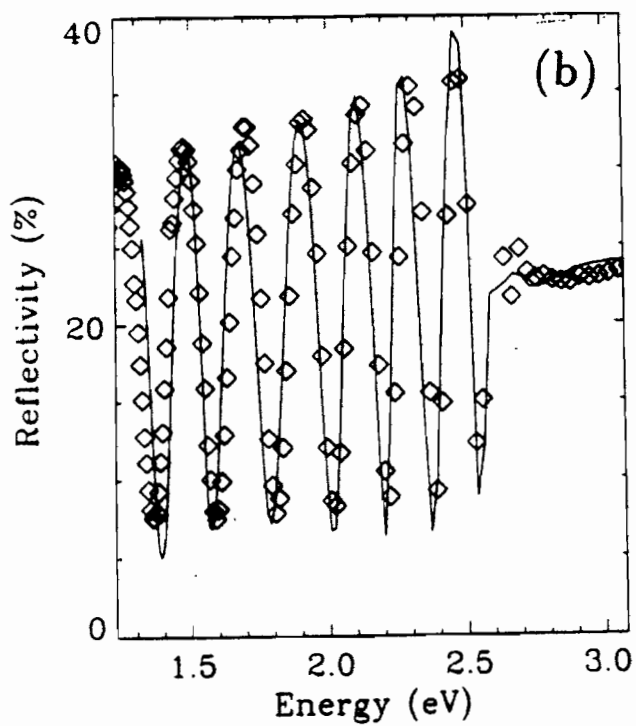
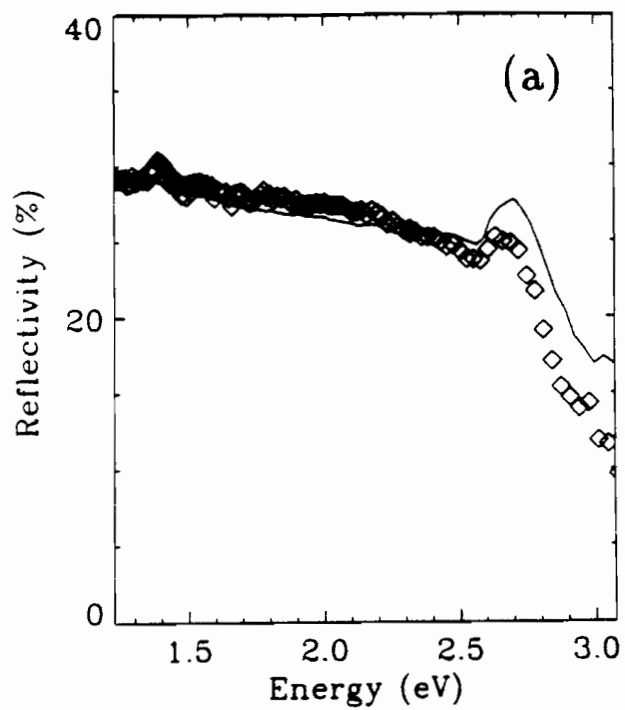


Figure 3.15: A typical linear spectrum of the sample. The overlayer thickness of these samples was (a) 215 Å and (b) 10280 Å. The solid line is the calculated reflectivity.

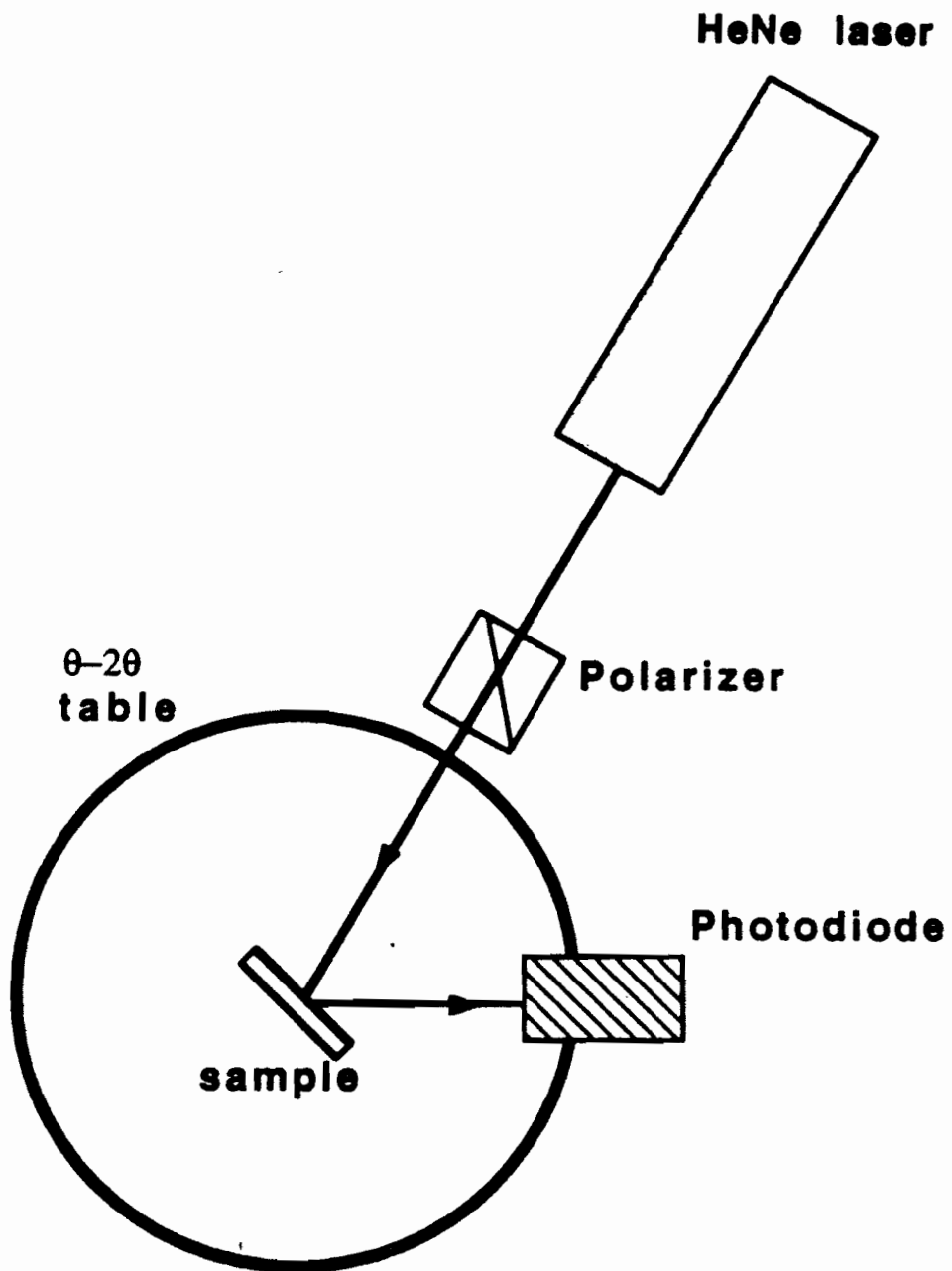


Figure 3.16: Experimental setup for thickness measurements. The linear reflectivity as a function of the angle of incidence was measured.

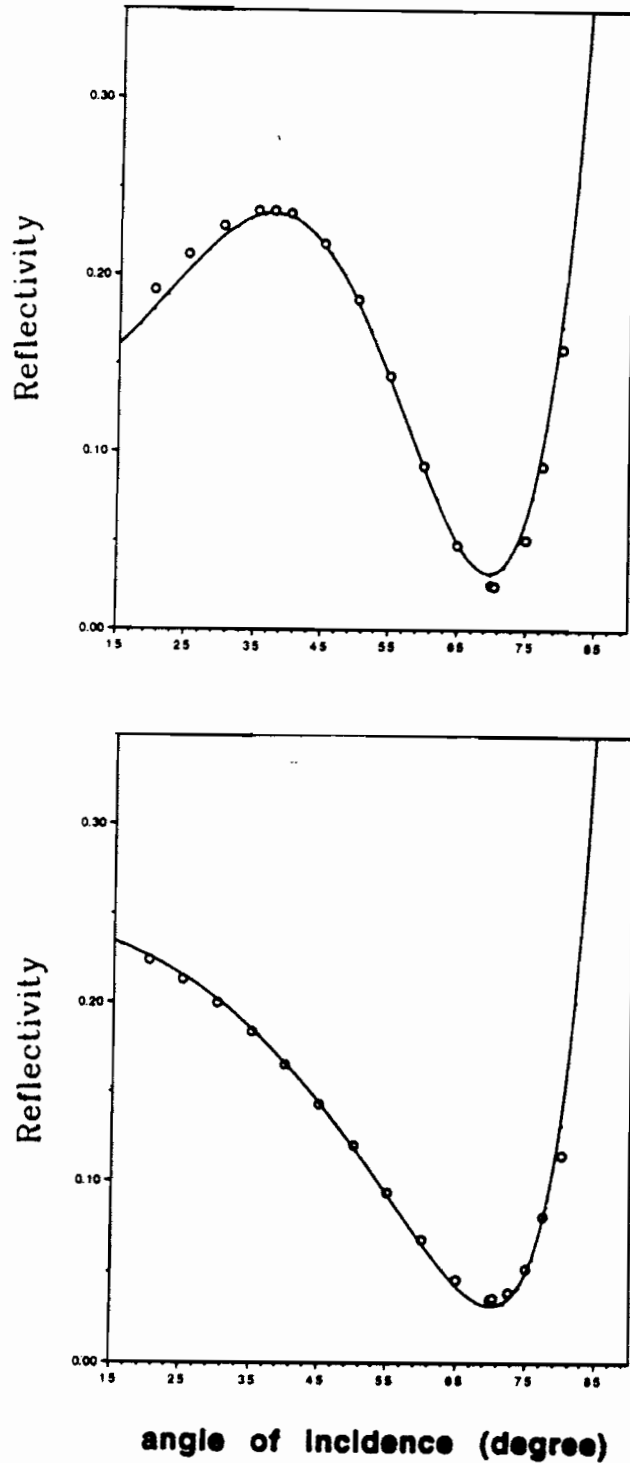


Figure 3.17: Linear reflectivity as a function of the angle of incidence. The solid line is the best fit of the optimum value of the overlayer thickness. Thickness of the overlayers were found to be 10280 Å (a) and 215 Å (b).

# Chapter 4

## Physical Properties of ZnSe and GaAs

The model system for our studies is the ZnSe/GaAs(001) heterostructure. This system was chosen because it exhibits many interesting fundamental physical problems and as a result of its practical application has been carefully characterized. This chapter discusses some of the basic physical properties of the ZnSe and GaAs bulk materials and introduces concepts required to discuss allowed optical transitions.

### 4.1 Crystalline Properties

Both ZnSe and GaAs crystallize in a zinc-blende structure. This structure consists of two face-center cubic lattices which are displaced from each other by a fourth of the lattice constant in the direction of (111) (Fig. 4.1). Each elementary cell contains

two atoms (e.g. Zn and Se or Ga and As) located at  $(0,0,0)$  and  $(a/4, a/4, a/4)$ , where  $a$  is the lattice constant. The lattice constants for GaAs and ZnSe at room temperature are  $5.6533 \text{ \AA}$  and  $5.6684 \text{ \AA}$ , respectively [58, 59]. This corresponds to a lattice mismatch of  $|a_{GaAs} - a_{ZnSe}|/a_{GaAs} = .27\%$ . The first Brillouin zone (BZ) of ZnSe and GaAs crystal is a truncated octahedron. The first BZ is shown in Fig. 4.2. We have also indicated several high symmetry points in the figure.

It should be noted that different cuts of ZnSe or GaAs result in different surface fields. The (111) or (001) surfaces contain only one atom type (e.g. Ga or As). This produces a polar surface. However the (110) zinc blende surface contains equal numbers of both atom types and thus, is electrically neutral and is considered a non-polar face.

## 4.2 Electronic Structures

There are 8 outer electrons in both GaAs (III-V) and ZnSe (II-VI). These electrons are shared by two atoms to generate band combinations. The other electrons are localized around the nuclei and are not involved in the optical transition in our energy range. The eight outer electrons are hybridized to form  $sp^3$  orbitals. These orbitals generate a tetrahedral bond combination within the two atoms.

For further discussion of the electronic structure of these two semiconductors we need to establish a general idea about the band structure of the system.

We can start with the Hamiltonian of a solid crystal [60]. That is

$$H = \sum \frac{P_i^2}{2m} + \frac{1}{2} \sum \frac{e^2}{|\mathbf{r}_i - \mathbf{r}_j|} + \sum V_n(\mathbf{r}_i - \mathbf{R}_n)$$

where the first and second terms are the summation of the electron kinetic energy and electron-electron Coulomb interaction, respectively. The last term represents the Coulomb interaction between the electron and the positively charged lattice. With the use of a mean field approximation where we assume each electron moves in an average field produced by all other electrons, the Hamiltonian reduces to the simple form of

$$H = \sum H_i$$

where  $H_i$  is the one electron Hamiltonian of the  $i$ th electron. This can be written as

$$H_i = \frac{\mathbf{P}_i^2}{2m} + V(\mathbf{r}).$$

The potential  $V(\mathbf{r})$  contains both the electron-lattice and electron-electron interactions. As a result, the wave function of the total Hamiltonian is the product of one electron wave function. It should be noted that the  $V(\mathbf{r})$  carries the same symmetry as the solid, that is  $V(\mathbf{r}) = V(\mathbf{r} - \mathbf{a})$  where  $a$  is the lattice spacing in the system.

For simplicity, the one dimensional problem will be discussed below, that is  $H(x, p) = \frac{p^2}{2m} + V(x)$ . Because of the periodicity of  $V(x)$ , we have

$$H(x, p) = H(x + a, p).$$

This suggested that the eigenfunction can be written as an eigenfunction of the translation operator,  $T$ .

The eigenfunctions of  $T$  can be written in the form  $\langle x|T|\psi\rangle = \lambda\langle x|\psi\rangle$ . By defining  $\lambda = e^{ika}$ , we can write

$$\psi(x+a) = e^{ika}\psi(x).$$

We also define  $u_k = e^{-ikx}\psi(x)$ , which leads to  $u_k(x+a) = u_k(x)$  and

$$\psi(x) = e^{ikx}u_k(x)$$

where  $\psi(x)$  is a plane wave modulated by a function with periodicity of the lattice. This wave function is called a Bloch wave. It is clear that the bulk of the crystal must have real  $k$ , otherwise  $\psi(x)$  diverges for large  $x$ .

Now we can write the Schödinger equation as

$$H\psi_{n,k}(r) = E_{kn}\psi_{n,k}(r). \quad (4.1)$$

The eigenvalue  $E$  also carries a subscript  $n$ , which represents the band index. The eigenvalue,  $E$ , as a function of  $k$ , for both ZnSe and GaAs are shown in Fig. 4.3. At the highest symmetry point, ( $\Gamma$ ), both semiconductors show minimum energy gaps. The transition between the valence band and the conduction band at  $\Gamma$  is called the  $E_0$  transition. Other important transitions are also shown in Fig. 4.3. We must note that the valence band at  $k = 0$ , in the absence of the spin-orbit coupling, is six-fold degenerate. The spin-orbit coupling breaks the degeneracy to a two- ( $j=1/2$ ) and a four-fold ( $j=3/2$ ) degeneracy. These three valence bands, the heavy hole, the light hole, and the split-off band, are displayed in Fig. 4.3.

### 4.2.1 Joint Density of States

To obtain an optical transition between two energy levels not only must the energy of the incident photon match the transition energy, but also a nonzero density of states in the levels must exist. To describe this transition mathematically and its relationship to susceptibility we start with the expression of  $\chi_{zz}^{(1)}$  and  $\epsilon_{zz}$  and relate the imaginary part of the dielectric constant to the joint density of states (JDOS), (see Appendix G for details of the derivation),

$$Im[\epsilon_{zz}(\omega)] = 8(\pi e/m\omega)^2 |P_{cv}|^2 J_{cv}(\omega) \quad (4.2)$$

where

$$J_{cv}(\omega) = \frac{1}{(2\pi)^3 \hbar} \int_{\mathbf{S}_{\omega_{cv}=\omega}} \frac{d\mathbf{S}_{cv}}{|\nabla_k \omega_{cv}|_{\omega_{cv}=\omega}}. \quad (4.3)$$

Here  $Im(\epsilon)$  presents the imaginary part of  $\epsilon$  and the function  $J_{cv}$  is the joint density of states (JDOS). For a description of the parameters see Appendix G.  $J_{cv}$  of GaAs and ZnSe, were calculated using known values of  $Im\epsilon(\omega)$ , and are plotted in Fig. 4.4. We must note that in calculating  $J_{cv}$ ,  $m$  and  $|P|^2$  are taken to be constant. Thus, we are able to obtain the JDOS necessary to interpret second order optical processes from linear optical measurements.

### 4.2.2 Absorption Coefficient

The absorption coefficient,  $\alpha$ , of ZnSe and GaAs is related to the imaginary part of the dielectric constant and thus, the electronic structure of the system. This

coefficient can be calculated for a given value of dielectric constant by

$$\alpha(\omega) = \frac{4\pi}{\lambda} \text{Im}\sqrt{\epsilon(\omega)}. \quad (4.4)$$

The absorption coefficients of ZnSe and GaAs are plotted in Fig. 4.5. It is clear that there is no absorption for energies less than the energy gap.

### 4.3 Selection Rules: Bulk

In addition to knowing the band structure and JDOS, it is also essential to know the selection rules that govern the system and determine which optical transitions are allowed, and which are forbidden. This section will explain the selection rules of all optical transitions involved in  $\chi^{(2)}$  and  $\chi^{(1)}$  at  $k = 0$  ( $\Gamma$  point). We will show that those transitions between the two highest valence bands and the two lowest conduction bands of ZnSe or GaAs are allowed and that the intraband transition between the conduction bands is forbidden. We will elaborate in more detail about the use of selection rules in determining allowable and forbidden transitions. This discussion relies heavily on group theory and can be skipped without any loss of content.

The existence of a certain symmetry in a system results in selection rules. The most systematic way to approach a symmetry problem is through group theory. Although an explanation of group theory is not included here, the important terminology and theorems will be briefly explained wherever necessary.

The zinc-blende crystals are invariant under the symmetry operators  $E, 8C_3, 3C_2, 6\sigma_d$  and  $6S_4$  [44, 45]. The collection of these operators forms the group  $T_d$ , that is

$$T_d = \{E, 8C_3, 3C_2, 6\sigma_d, 6S_4\}. \quad (4.5)$$

Since a group is a closed set, the result of “multiplication” of the two elements is an element of the set. The “multiplication” of elements is usually summarized in a multiplication table. A group *representation* is used to describe the symmetry operators. A representation of a group is a collection of mathematical entities that has the same multiplication table as the original set, for this case  $T_d$  [44, 45]. These entities are taken to be matrices with the following properties:

- 1- square
- 2- non singular (i.e. the determinants of these matrices are nonzero)
- 3- form a group

This simply means that, for example, the operator  $E$  in 2 dimensions can be represented by a 2 dimensional unitary matrix. Since it is easier to work with matrices than the symmetry operators themselves, matrices are a good choice for the representation of a group. However, one problem still remains unsolved. That is for a given dimension, the matrix representation is not unique. We can start with any representation, apply a similarity transformation (i.e.  $A' = S^{-1}AS$ ), and get a new representation. To solve this problem, groups are represented by the trace of the matrices, called the character. This new representation is unique because the trace of a matrix remains unchanged under any similarity transformation. The character

table of  $\bar{T}_d$  ( $\bar{T}_d$  is the double group of  $T_d$  which includes the spin) is given in Table 4.1. Each row of the table is labeled with  $\Gamma_i$ , which is the character representation of the group. Since  $E$  is the unitary operator, the trace of  $E$  is equal to the dimension of the representation. For example,  $\Gamma_2(E) = 1$  means that the  $\Gamma_2$  is a one dimensional representation; similarly,  $\Gamma_3$  is a two-dimensional representation, and so on. It can be shown that the eigenfunctions of the Hamiltonian of a system transform as one of the irreducible representations of the group. The dimension of the irreducible representation is equal to the degeneracy of the energy level. For example, Table 4.1 shows that the maximum degeneracy in GaAs or ZnSe is four-fold.

### 4.3.1 Basis Function

In addition to the representation, the “form” of the basis function of each representation is needed. The importance of this will be clear in the next section. By “basis function” we do not mean the exact mathematical expression of the wavefunction, but rather a very simple mathematical expression which transforms exactly like the irreducible representation. As an example for the 1-dimension representation,  $\Gamma_1$ , we have to introduce a function,  $\psi_1$ , such that it will be invariant under all operators. The usual choice for this function is  $xyz$ . A systematic way to describe the basis function is with projection operators. This method is described in reference [44] and the resultant basis function for  $T_d$  is tabulated in Table 4.1.

Now we can discuss the transition between the different energy levels of GaAs or

ZnSe. Let's take  $H^1$  as the transition operator. We are interested in studying the matrix element of

$$\langle \psi^\alpha | H^1 | \psi^\beta \rangle = \langle \psi^\alpha | H^1 \psi^\beta \rangle. \quad (4.6)$$

Here  $\psi^\alpha$  ( $\psi^\beta$ ) is the basis function for the energy level with irreducible representation  $\Gamma_\alpha$  ( $\Gamma_\beta$ ). Let  $H^1$  be described by one of the irreducible representations of the group, say  $\Gamma_{H^1}$ .  $\psi^\alpha$  transforms as  $\Gamma_\alpha$ , and  $H^1 \psi^\beta$ , in general, contains parts that transform as different irreducible representations of the group. In other words,  $H^1 \psi^\beta$  transforms as the direct product of  $\Gamma_{H^1}$  and  $\Gamma_\beta$ . Because of the orthogonality of the basis functions, the above matrix element is zero if the direct product of  $\Gamma_\beta$  and  $\Gamma_{H^1}$  does not contain  $\Gamma_\alpha$ . The direct product of  $\bar{T}_d$  is given in Table 4.2.

A dipole transition operator is represented by  $\Gamma_5$  (consult Table 4.1). Now if we consider the transition between the valence band ( $\Gamma_8$ ) and the conduction band ( $\Gamma_6$ ) at  $k = 0$  (see Fig. 4.6a), then the transition can be described by the following matrix element:

$$\langle \Gamma_6 | \Gamma_5 | \Gamma_8 \rangle = \langle \Gamma_6 | \Gamma_5 \times \Gamma_8 \rangle. \quad (4.7)$$

Using Table 4.2 we can write

$$\Gamma_5 \times \Gamma_8 = \Gamma_6 + \Gamma_7 + 2\Gamma_8. \quad (4.8)$$

The direct product of  $\Gamma_5$  and  $\Gamma_8$  includes  $\Gamma_6$ , thus the dipole transition between these bands at  $k=0$  is allowed. This result indicates that  $\chi^{(1)}$  could have resonance due to the transition between  $\Gamma_8$  and  $\Gamma_6$ . This is consistent with the observation of the  $E_0$  transition in linear reflectivity.

It is also interesting to investigate the possibility of observing the  $E_0 + \Delta_0$  transition. The matrix element for this transition is written as

$$\langle \Gamma_6 | \Gamma_5 | \Gamma_7 \rangle = \langle \Gamma_6 | \Gamma_5 \times \Gamma_7 \rangle. \quad (4.9)$$

Using Table 4.2 we can write

$$\Gamma_5 \times \Gamma_7 = \Gamma_6 + \Gamma_8. \quad (4.10)$$

Since it includes  $\Gamma_6$ ,  $E_0 + \Delta_0$  is also possible (see Fig. 4.6b). It must be emphasized that the symmetry only tells us if the matrix elements are zero or nonzero. *It does not give any information about the actual strength of the matrix elements.*

### 4.3.2 Bulk Intraband Transition at $k = 0$ : Two-level Processes

A second-order susceptibility can involve an intraband transition. In this case the usual three level process, explained in Chapter 2, reduces to a two level process (see Fig. 4.7a). This type of process was first observed by M. Jiang *et. al.* in Cu(110) [61]. The analogous process at  $k = 0$  in GaAs or ZnSe bulk can be shown by the irreducible representation as follows:

$$\Gamma_8 \rightarrow \Gamma_6 \rightarrow \Gamma_6 \rightarrow \Gamma_8. \quad (4.11)$$

The first step of this transition is an interband transition from valence band to conduction band. An intraband transition in the conduction band is the second

step, and the last step is an interband transition from conduction band back to the valence band. We know now that all the interband transitions between  $\Gamma_6$  and  $\Gamma_8$  are allowed, therefore we need only to check the intraband transition. The matrix element is

$$\langle \Gamma_6 | \Gamma_5 | \Gamma_6 \rangle = \langle \Gamma_6 | \Gamma_5 \times \Gamma_6 \rangle. \quad (4.12)$$

Using a direct product multiplication table we can also write

$$\Gamma_5 \times \Gamma_6 = \Gamma_7 + \Gamma_8. \quad (4.13)$$

The result does not include  $\Gamma_6$ , thus

$$\langle \Gamma_6 | \Gamma_5 | \Gamma_6 \rangle = 0. \quad (4.14)$$

Another possible two level process is (see Fig. 4.7b)

$$\Gamma_8 \rightarrow \Gamma_8 \rightarrow \Gamma_6 \rightarrow \Gamma_8. \quad (4.15)$$

This is an allowed process based on the symmetry consideration. However, this process can not be strong, because under normal conditions, the number of unoccupied states in the valence band is very small.

### 4.3.3 Possible Three Level Process at $k = 0$

A three level process which contains three interband transitions is shown in Fig. 4.8.

We can describe this transition as

$$\Gamma_8 \rightarrow \Gamma_7 \rightarrow \Gamma_6 \rightarrow \Gamma_8. \quad (4.16)$$

This process makes it possible to observe the  $E_0$  transition in either GaAs or ZnSe. For  $E_0$  resonance of  $\chi^{(2)}$  the  $\Gamma_8 \rightarrow \Gamma_7$  transition is the most probable first stage transition of the three-level process. This results from the energy consideration that appears in the denominator of the  $\chi^{(2)}$ . It implies that the transition with the smallest energy difference is the most probable one. In Chapter 5, we will calculate  $\chi^{(2)}$  of ZnSe and compare it to our experimental results.

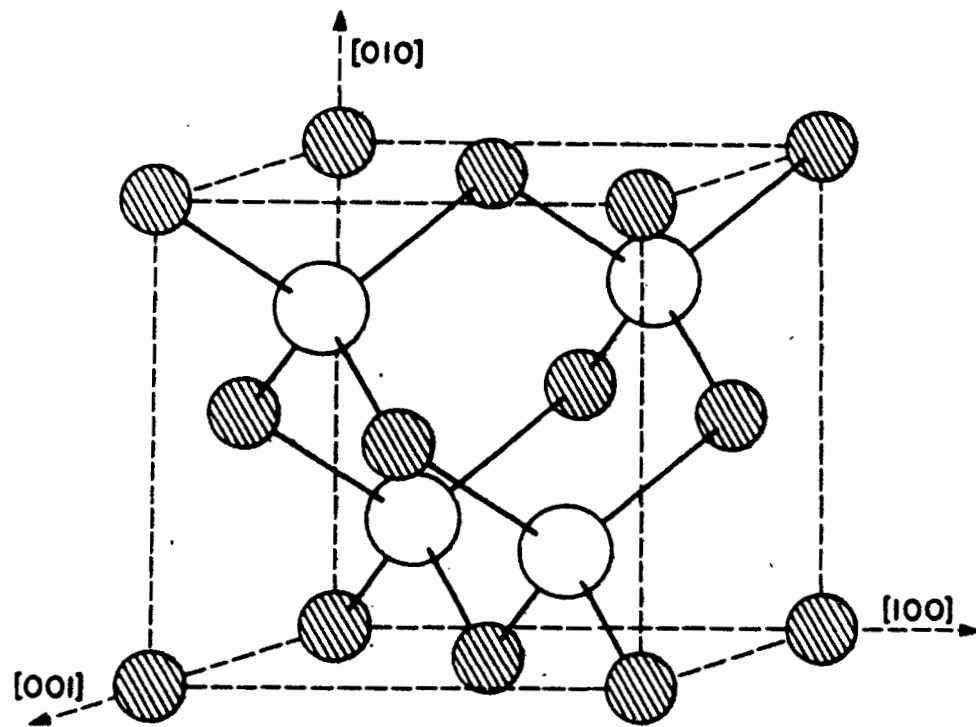


Figure 4.1: Atomic arrangement in a zinc-blende crystal.

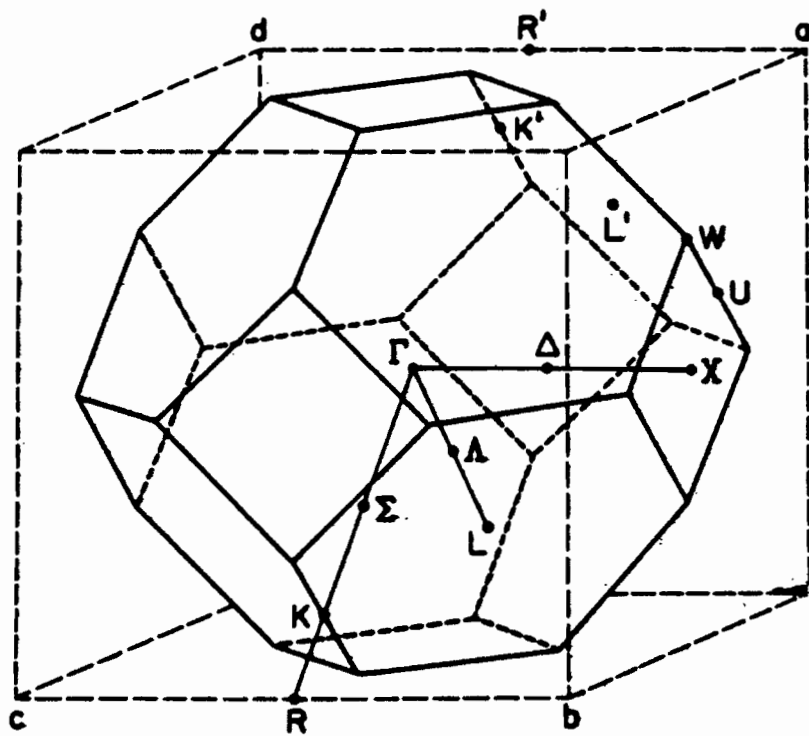


Figure 4.2: First Brillouin zone for the GaAs and ZnSe lattice. Some of the high symmetry points and lines are labeled.

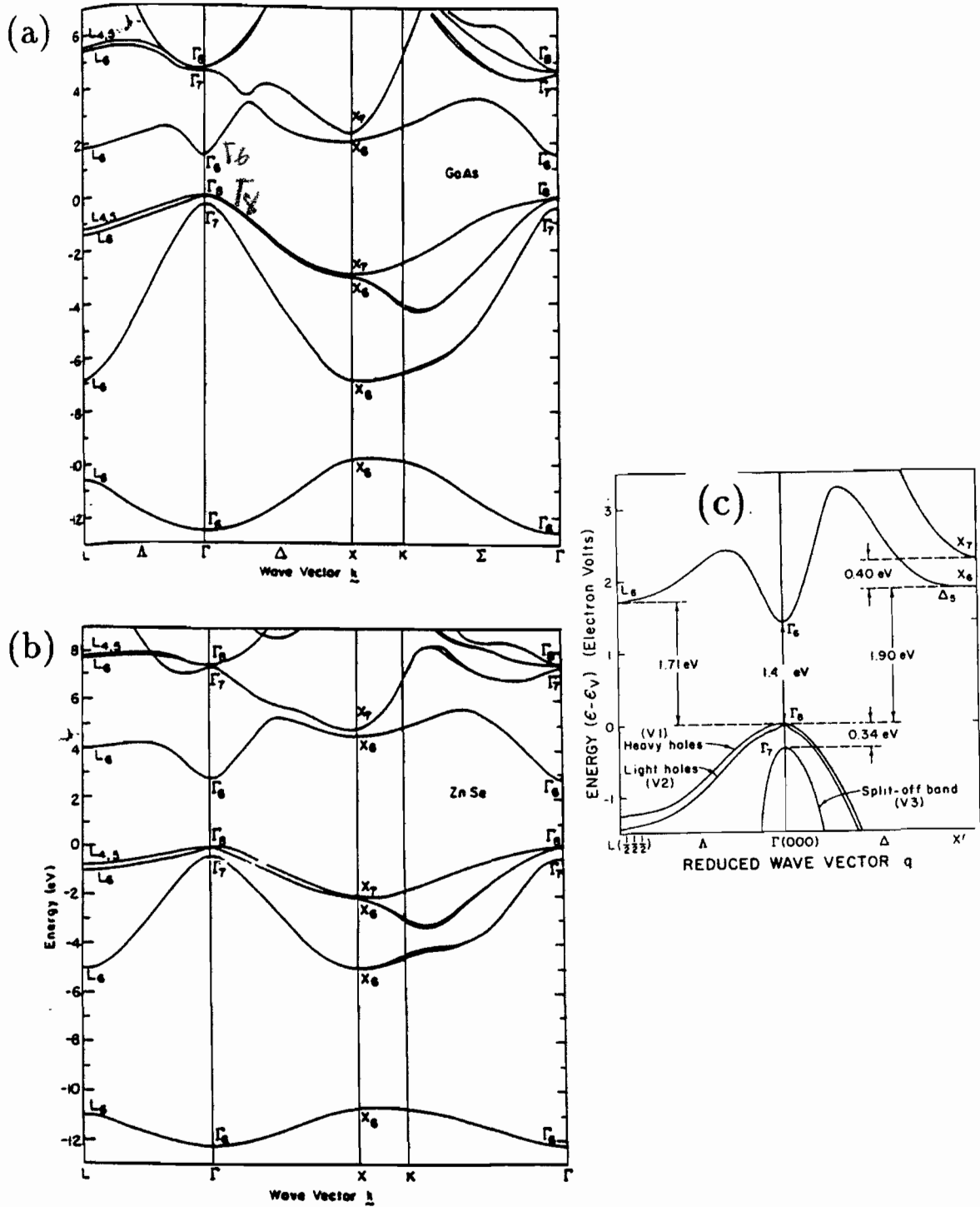


Figure 4.3: The electronic band structure of (a)GaAs and (b)ZnSe. Some important transitions are shown. The heavy hole, light hole and split-off band is shown in (c).

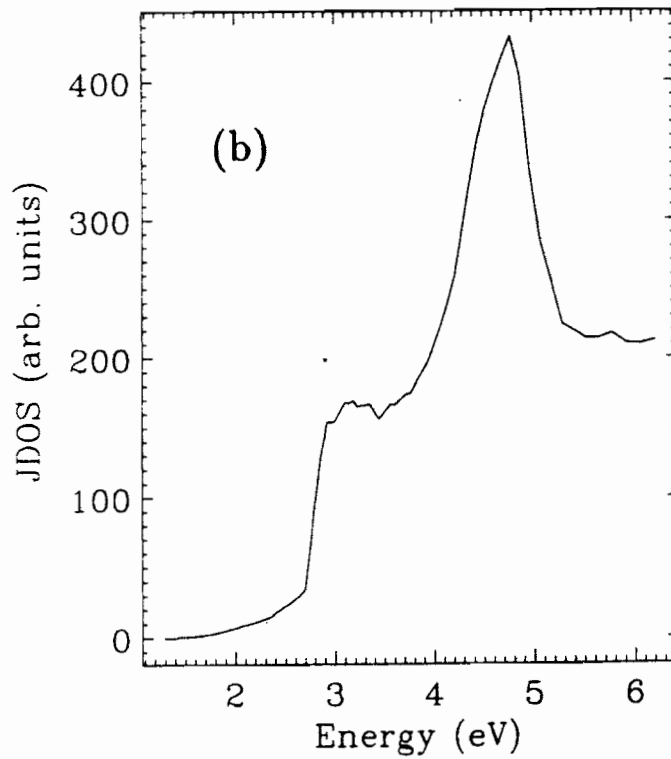
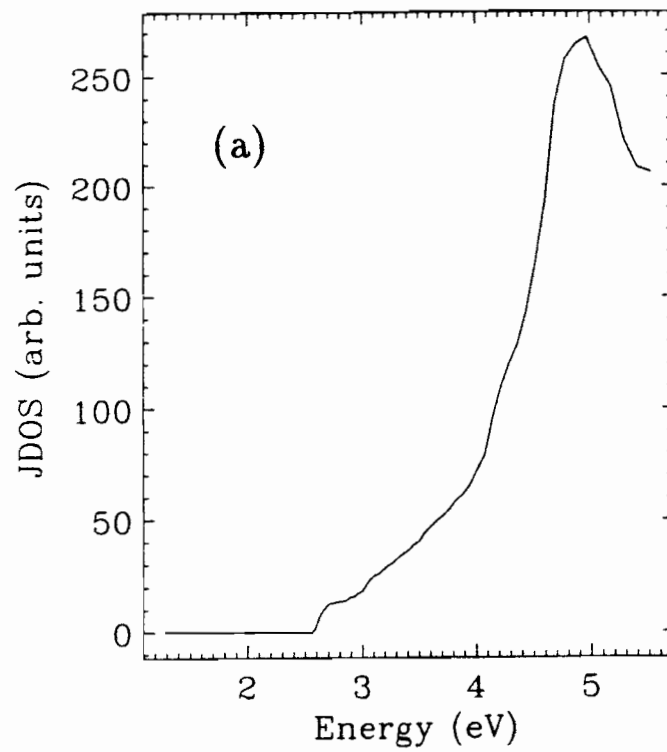


Figure 4.4: The calculated JDOS of (a) ZnSe and (b) GaAs as a function of energy.

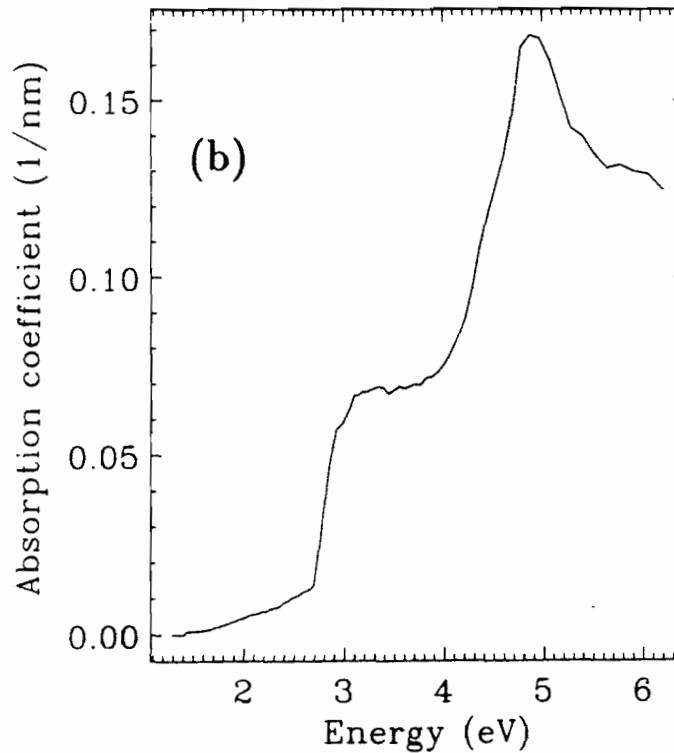
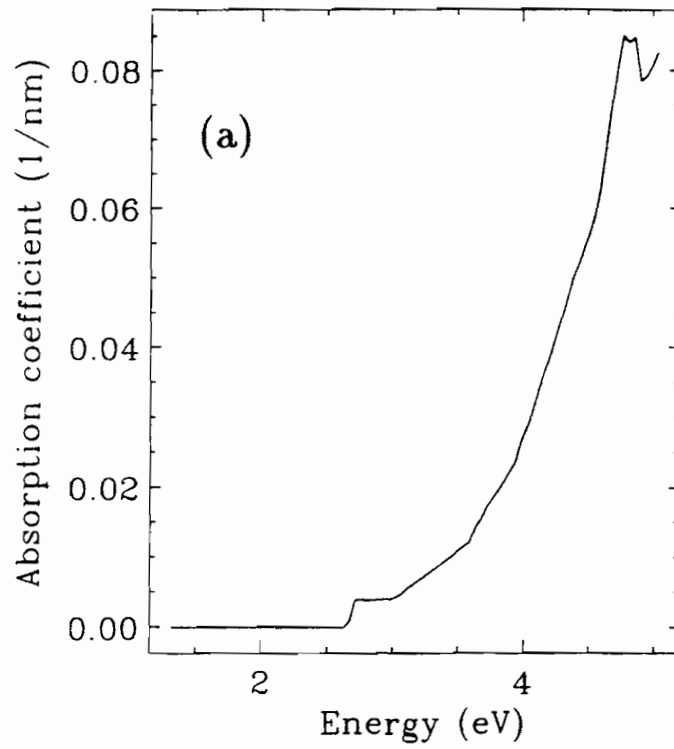


Figure 4.5: The absorption coefficient of (a) ZnSe and (b) GaAs as a function of energy.

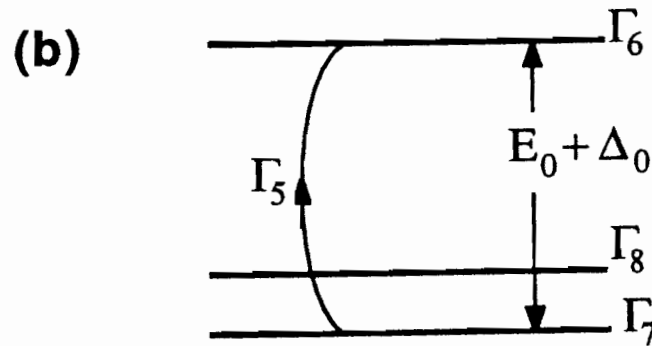
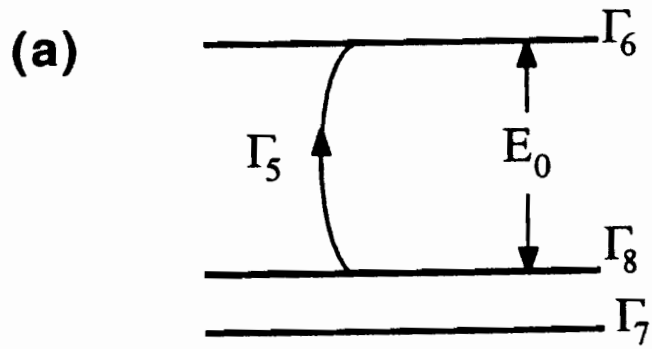


Figure 4.6: Linear optical transition between (a)  $\Gamma_8$  and  $\Gamma_6$ ,  $E_0$  transition, and (b)  $\Gamma_7$  and  $\Gamma_6$ ,  $E_0 + \Delta_0$  transition,. The dipole operator is represented by  $\Gamma_5$ .

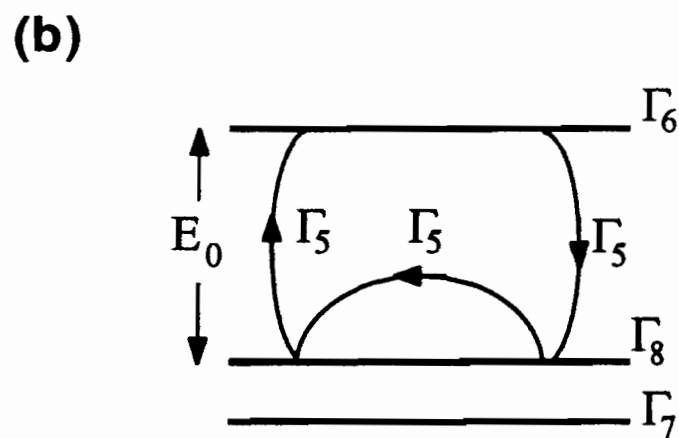
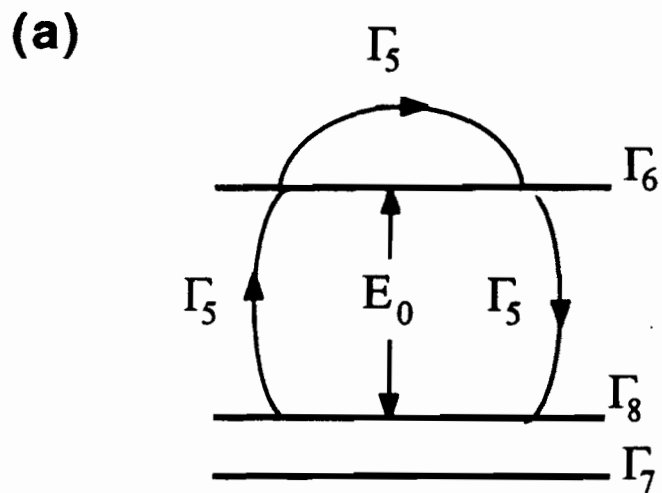


Figure 4.7: Two level process in GaAs and ZnSe systems. (a) The interband transition of  $\Gamma_6$  to  $\Gamma_6$  is forbidden. (b) The  $\Gamma_8$  to  $\Gamma_8$  transition is allowed by symmetry, however this process may not be strong.

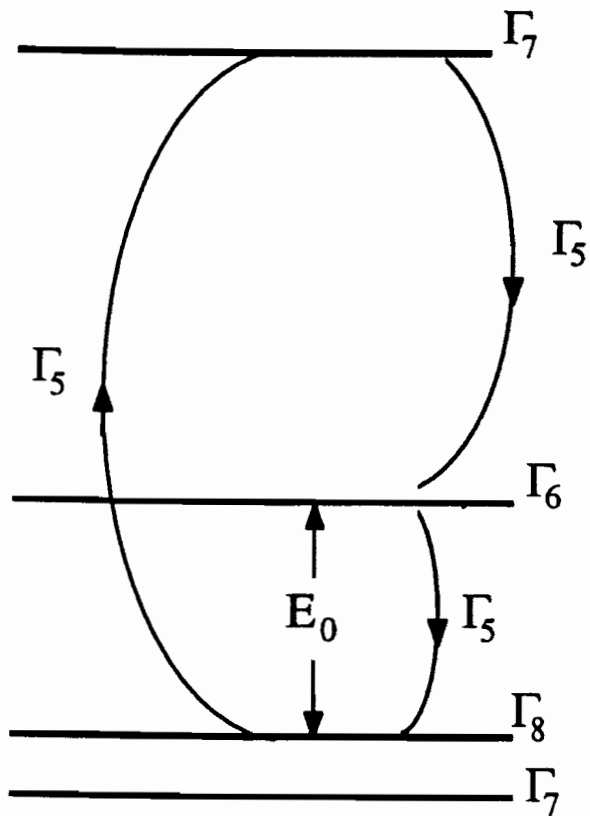


Figure 4.8: A possible three-level process in ZnSe or GaAs bulk system. The dipole operator is represented by  $\Gamma_5$ .

Table 4.1: Character table of  $\bar{T}_d$

$T_d$	E	$\bar{E}$	$8C_3$	$8\bar{C}_3$	$3C_2$ $3\bar{C}_2$	$6S_4$	$6\bar{S}_4$	Time Inv.	Bases for $T_d$	
$\Gamma_1$	1	1	1	1	1	1	1	a	xyz	
$\Gamma_2$	1	1	1	1	1	-1	-1	a	$8_x, 8_y, 8_z$	
$\Gamma_3$	2	2	-1	-1	2	0	0	a	$(2x^2 - x^2 - y^2),$ $\sqrt{3}(x^2 - y^2)$	
$\Gamma_4$	3	3	0	0	-1	1	1	a	$8_x, 8_y, 8_z$	
$\Gamma_5$	3	3	0	0	-1	-1	-1	a	x, y, z	
$\Gamma_6$	2	-2	1	-1	0	$\sqrt{2}$	$-\sqrt{2}$	0	c	$\phi(1/2, -1/2),$ $\phi(1/2, 1/2)$
$\Gamma_7$	2	-2	1	-1	0	$-\sqrt{2}$	$\sqrt{2}$	0	c	$\Gamma_6 \times \Gamma_3$
$\Gamma_8$	4	-4	-1	1	0	0	0	0	c	$\phi(3/2, -3/2),$ $\phi(3/2, -1/2),$ $\phi(3/2, 1/2),$ $\phi(3/2, 3/2)$

Table 4.2: Direct product table of  $\bar{T}_d$

$\Gamma_1$	$\Gamma_2$	$\Gamma_3$	$\Gamma_4$	$\Gamma_5$	$\Gamma_6$	$\Gamma_7$	$\Gamma_8$	
$\Gamma_1$	$\Gamma_2$	$\Gamma_3$	$\Gamma_4$	$\Gamma_5$	$\Gamma_6$	$\Gamma_7$	$\Gamma_8$	$\Gamma_1$
	$\Gamma_1$	$\Gamma_3$	$\Gamma_5$	$\Gamma_4$	$\Gamma_7$	$\Gamma_6$	$\Gamma_8$	$\Gamma_2$
		$\Gamma_1 + \Gamma_2 + \Gamma_3$	$\Gamma_4 + \Gamma_5$	$\Gamma_4 + \Gamma_5$	$\Gamma_8$	$\Gamma_4$	$\Gamma_6 + \Gamma_7 + \Gamma_8$	$\Gamma_3$
			$\Gamma_1 + \Gamma_3 + \Gamma_4 + \Gamma_5$	$\Gamma_2 + \Gamma_3 + \Gamma_4 + \Gamma_5$	$\Gamma_6 + \Gamma_8$	$\Gamma_7 + \Gamma_8$	$\Gamma_6 + \Gamma_7 + 2\Gamma_8$	$\Gamma_4$
				$\Gamma_1 + \Gamma_3 + \Gamma_4 + \Gamma_5$	$\Gamma_7 + \Gamma_8$	$\Gamma_6 + \Gamma_8$	$\Gamma_6 + \Gamma_7 + 2\Gamma_8$	$\Gamma_5$
					$\Gamma_1 + \Gamma_4$	$\Gamma_2 + \Gamma_3$	$\Gamma_3 + \Gamma_4 + \Gamma_5$	$\Gamma_6$
						$\Gamma_1 + \Gamma_4$	$\Gamma_3 + \Gamma_4 + \Gamma_5$	$\Gamma_7$
							$\Gamma_1 + \Gamma_2 + \Gamma_3$	
							$+2\Gamma_4 + 2\Gamma_5$	$\Gamma_8$

## Chapter 5

# Interference in Reflected SHG

## From Thin Nonlinear Slabs

### 5.1 A Method to Measure $\chi^{(2)}$ of Thin Overlayers

Although interference in reflection from thin multilayered dielectric films is an important and well understood phenomena in linear optics [62], the analogous problem in nonlinear optics is not well studied. Nearly thirty years ago Bloembergen and coworkers introduced electromagnetic nonlinearities into Maxwell's equations and derived the conditions for reflection and refraction at the surfaces of nonlinear dielectrics [46]. They showed that the solution of Maxwell's equations with the proper boundary conditions leads to the production of harmonic waves in reflection and transmission. The most widely studied *interference* phenomena in nonlinear optics

was connected with the generation of harmonics in transmission through a single nonlinear slab. Under these conditions one observes Maker fringes [63, 64]. These fringes arise because the source polarization and the free wave generated by this polarization have different phase velocities. In this chapter we investigate a new class of nonlinear optical interference phenomena that is more akin to linear reflection from a dielectric mirror. In particular we observe interference in the production of second harmonic (SH) waves as a result of reflection from two adjoined nonlinear optical slabs.

Besides its intrinsic interest as a new phenomena, interference in harmonic generation from thin nonlinear films is important for other reasons. For example, *the phenomena provides a methodology for measuring the second-order susceptibility of thin overlayer materials*. Since many unusual crystalline materials can only be grown in very thin layers above other high quality solids [65], the ability to measure nonlinearities in composite systems is valuable. In addition, as the use of three-wave mixing to probe solid interfaces grows [21, 22, 23, 24], it becomes essential to fully understand how interference phenomena can affect the intensity of these signals.

We have observed interference in reflected second harmonic generation (SHG) from a series of ZnSe/GaAs[001] heterostructures with varying overlayer thickness. A theoretical solution of the problem is presented, and used to analyze our measurements. Our solution combines results from reference [46] with new boundary

conditions that arise at the interface of two nonlinear media. We find that the reflected SH intensity oscillates as a function of overlayer thickness. In contrast to the simple Maker fringe result however, more than six Fourier components contribute to the spatial dependence of this oscillation. Finally, we use our interference data along with our theoretical solution to determine the frequency dependence of the bulk second-order susceptibility of ZnSe.

The remainder of this chapter is organized as follows. We first describe some of the experimental aspects then we present theoretical calculations of the nonlinear interference effect, and compare these calculations with experiment. Then, we present measurements of the frequency dependence of the ZnSe and GaAs bulk second-order nonlinearities as a function of the SH photon energy between 2.6 eV and 3.1 eV. Finally we discuss a simple theoretical model for the calculation of  $\chi_{xyz}^{(2)}$  of ZnSe at  $k = 0$ .

## 5.2 Experiment

The details of the experiments and apparatus were described in Chapter 3. In this section we discuss some of the experimental aspects concerned in the separation of bulk and the interface signals. The bulk signals from the ZnSe/GaAs[001] samples were separated from the interface signals by proper choice of sample orientation and light polarization [66]. GaAs and ZnSe are zinc blende crystals with  $\bar{4}3m$  symmetry. They both have a single non-zero bulk second-order susceptibility tensor element,

$\chi_{xyz}^{(2)}$ , [36] whose contribution to the output radiation is highly anisotropic. For the p-in/s-out polarization configuration, the SHG output intensity is proportional to  $\cos^2(2\phi)$ , where  $\phi$  is the angle between the [100] direction and the plane of incidence. The orientation dependence of our SHG signal is illustrated in Fig. 2.3. Frequency-dependent measurements were performed using the p-in/s-out polarization configuration at  $\phi = 0$ . Using this configuration we maximized our sensitivity to the bulk nonlinearity. In analyzing our results we have used the linear dielectric constants for GaAs and ZnSe given in references [54] and [55], respectively. These values were checked against our own linear reflectivity measurements, and agreement was good (see Chapter 3).

### 5.3 Two Adjoined Nonlinear Optical Slabs: Theory

In this section we will use the results of Chapter 2 and discuss the interference from two nonlinear slabs. For all the expressions below, the subscripts “0”, “1” and “2” refer to vacuum, first medium and second medium, respectively. The subscript “ $Rlm$ ” refers to the reflected harmonic wave which is generated in medium “ $l$ ” and propagates through medium “ $m$ ”. We also assume that the second-order susceptibilities and dielectric constants change discontinuously at all interfaces.

The second harmonic field produced in reflection from two nonlinear slabs is

more complex. This complexity arises as a result of the new interface, and the second nonlinear medium. Loosely speaking there are three fields which contribute to the total reflected second harmonic field in the vacuum: (1) a reflected SH field generated from the first slab, (2) a multiply reflected SH field produced as a result of the propagation of the free and bound harmonic waves in medium 1, and (3) a multiply reflected SH field generated from the second slab. We will see that the total reflected SH intensity in the vacuum oscillates with respect to overlayer thickness at spatial frequencies determined by  $k_{f1,z}$ ,  $k_{b1,z}$ , and  $k_{b2,z}$ .

The first reflected SH field is produced in slab one and propagates into the vacuum in the direction of the fundamental reflected field (Fig. 5.1a). The solution for this wave is given by Eq. (2.30) with values of  $\chi^{(2)}$  and  $Y$  appropriate to medium 1, which in our case is ZnSe[001].

The second field (depicted in Fig. 5.1b) is produced when both free and bound waves generated in medium 1 propagate to the buried interface at  $z = -d$ . Their propagation obeys Eq. (2.26). In general, both bound and free waves are reflected from the interface. The exact boundary conditions used to determine these fields are given in Appendix D. The reflection of the bound wave depends primarily on the linear reflection of the fundamental wave at the buried interface. If the reflection amplitude for the fundamental field is small, the reflected bound wave is also small and our solution simplifies. This is the case for the ZnSe/GaAs[001] interface in our measured energy range. The reflected fundamental intensity is at least 20x smaller

than the incident fundamental intensity, and we safely use the simpler result to find that

$$E_{\perp,R11}^{(2\omega)} = r_{\perp,12}^{(2\omega)} E_{f1} e^{-2idk_{f1,z}} + \left[ \frac{k_{b1,z} - k_{f2,z}}{k_{f1,z} + k_{f2,z}} \right] \frac{4\pi P_{\perp,1}}{\epsilon_{b1} - \epsilon_{f1}} e^{-id(k_{f1,z} + k_{b1,z})}. \quad (5.1)$$

This field propagates to the first boundary at  $z = 0$  where some harmonic light is transmitted into the vacuum. Multiple reflections change the amplitude of the transmitted field by a factor of

$$g = \left[ 1 - r_{\perp,10}^{(2\omega)} r_{\perp,12}^{(2\omega)} e^{-2idk_{f1,z}} \right]^{-1}. \quad (5.2)$$

The effects of multiple reflections are important for thin overlayers, and must be included to ensure that radiation from medium 1 reduces to zero as the first slab thickness approaches zero.

A third SH field is depicted in Fig. 5.1c, and discussed in detail in Appendix D. It arises when the fundamental field is transmitted through medium 1 into medium 2. In medium 2 the field interacts to produce a nonlinear polarization,  $\mathbf{P}_{\perp,2}^{(2\omega)}$ . This polarization radiates a field back into medium 1 given by Eq. (2.30). In our case we must insert values of  $\chi_{xyz}^{(2)}$  and  $Y$  appropriate to GaAs[001] and the ZnSe/GaAs[001] interface. The reflected second harmonic wave due to the second slab  $E_{\perp,R21}^{(2\omega)}$  is

$$E_{\perp,R21}^{(2\omega)} = \frac{4\pi P_{\perp,2}}{\epsilon_{b2} - \epsilon_{f2}} \left[ \frac{k_{f2,z} - k_{b2,z}}{k_{f1,z} + k_{f2,z}} \right] e^{-id(k_{f1,z} + k_{b2,z})}. \quad (5.3)$$

This field propagates to the first interface at  $z = 0$  where again some light at  $2\omega$  is transmitted into the vacuum. Multiple reflections also change the amplitude of this field by a factor of  $g$ . The total reflected field is the sum of all harmonic fields in the

vacuum. This field can be written in a fairly simple form that clearly delineates the linear and nonlinear contribution of the two layers,

$$E_{\perp,tot}^{(2\omega)} = (Y_1 \chi_{xyz-1}^{(2)} + Y_2 \chi_{xyz-2}^{(2)}) E_{\parallel}^{(\omega)2}. \quad (5.4)$$

Here,

$$Y_1 = g t_{\perp,10}^{(2\omega)} Q_1 \left[ r_{\perp,12}^{(2\omega)} \left( \frac{k_{f0,z} - k_{b1,z}}{k_{f1,z} - k_{f0,z}} \right) e^{-2idk_{f1,z}} + \left( \frac{k_{b1,z} - k_{f2,z}}{k_{f1,z} + k_{f2,z}} \right) e^{-id(k_{f1,z} + k_{b1,z})} + \frac{1}{g t_{\perp,01}^{(2\omega)}} \left( \frac{k_{b1,z} - k_{f1,z}}{k_{f0,z} - k_{f1,z}} \right) \right], \quad (5.5)$$

$$Y_2 = g t_{\parallel,12}^{(\omega)2} t_{\perp,10}^{(2\omega)} Q_2 \left[ \frac{k_{f2,z} - k_{b2,z}}{k_{f2,z} + k_{f1,z}} \right] e^{-id(k_{f1,z} + k_{b2,z})}, \quad (5.6)$$

$$Q_j = \frac{4\pi t_{\parallel,01}^{(\omega)2}}{\epsilon_{bj} - \epsilon_{fj}} \frac{-k_{tj,z} k_{tj,x}}{k_{tj}^2} 2 \cos(2\phi). \quad (5.7)$$

and the detected harmonic intensity,  $I_{tot}^{(2\omega)}$  is

$$I_{tot}^{(2\omega)} = \frac{c}{8\pi} |E_{\perp,tot}^{(2\omega)}|^2. \quad (5.8)$$

The  $Y_i$  depend on overlayer thickness  $d$ , incidence angle, and various constants that are derived from the linear properties of the media. This function is a complex exponential and is responsible for the oscillation of the intensity of the total reflected SH field and the decay of the SH power with increasing overlayer thickness.

The intensity of  $E_{\perp,tot}$ , without multiple reflections, contains six oscillatory terms of the form  $\sin^2(d(k_{f1,z} \pm k_{\beta,z})/2)$ , and  $\sin^2(d(k_{b1,z} - k_{b2,z})/2)$  where  $\beta = b1, b2,$  and  $f1$ . This is to be contrasted with the Maker fringe result, that has only one oscillatory term when multiple reflections are omitted, i.e.  $\sin^2(d(k_{f1,z} - k_{b1,z})/2)$ . The number of oscillatory terms *increases* when multiple reflections are included. None of the

differences discussed above arise unless the second-order susceptibility in the second slab is non-zero.  
zero

## 5.4 Results

We have measured the SHG spectra of nine ZnSe/GaAs[001] samples with different overlayer thicknesses (Fig. 5.2). In this way we determined the thickness dependence of the reflected SH intensity at various photon energies. The result at 2.67 eV is shown in Fig. 5.3. The intensity shows a strong oscillation with respect to the thickness of the overlayer. For large values of thickness,  $d$ , the intensity approaches the SH intensity of a semi-infinite slab of ZnSe. We have observed this two-slab interference effect for SH photon energies between 2.6 eV and 3.1 eV.

The second-order susceptibility of GaAs[001] deduced from our separate SHG measurements, along with literature values for the dielectric constants of ZnSe and GaAs, were used to fit each set of interference data to Eqs. (5.4-5.8). The solid line in Fig. 5.3 is a theoretical fit to our experimental data. The agreement is good. It lends support for our assumption that the second-order bulk susceptibility of our samples is independent of position in each medium within the sample, and it corroborates our primary theoretical results.

The magnitude of the second-order susceptibility of ZnSe, and its relative phase with respect to  $\chi_{xyz}^{(2)}$  of GaAs, were the only two free parameters in our fitting routine. Thus, we are able to use our interference data to deduce the frequency-dependent

magnitude of the second-order susceptibility of ZnSe. Our deduced  $|\chi_{xyz}^{(2)}|$  for ZnSe are shown in Fig. 5.4. This susceptibility exhibits a relatively sharp resonance at  $\sim 2.67$  eV. This peak corresponds to the  $E_0$  transition of ZnSe. In addition we see that the phase between the ZnSe and GaAs susceptibilities changes by  $180^\circ$  near this resonance (Fig. 5.5). The GaAs peak (Fig. 2.5) is less pronounced than the ZnSe because the joint density of states (JDOS) at the  $\Gamma$  point in GaAs is  $\sim 20$  smaller than in ZnSe (see Chapter 4).

## 5.5 $\chi_{xyz}^{(2)}$ Calculation of ZnSe

The dispersion of  $E(k)$  can be approximately described by a simple parabolic curve for very small  $k$ . This approximation method simplifies the calculation of the susceptibility and was successfully used to compute the  $\chi^{(1)}$  by M. Cardona [67]. Bell [68] and Fong [69] carried out a similar calculation for  $\chi^{(2)}$ . Their results were compared to the experimental data [69] of narrow band gap semiconductors. However there has not been a comparison of this method of calculation for wide band gap semiconductors. This is due to a lack of experimental results for wide band gap systems. In this section we will discuss the calculation and compare the outcome with the experimental results.

### 5.5.1 Method of Calculation

The second-order susceptibility tensor,  $\chi_{xyz}^{(2)}$ , is written in the form

$$\begin{aligned} \chi_{xyz}^{(2)} = & \left(\frac{-Ne^3}{\hbar}\right) \sum_{nn'} M \left\{ \frac{1}{(2\omega - \omega_{ng} + i\Gamma_{ng})(\omega - \omega_{n'g} + i\Gamma_{n'g})} \right. \\ & + \frac{1}{(2\omega + \omega_{ng} + i\Gamma_{ng})(\omega + \omega_{n'g} + i\Gamma_{n'g})} - \frac{1}{(2\omega - \omega_{n'n} + i\Gamma_{n'n})} \\ & \left. \times \left[ \frac{1}{\omega + \omega_{ng} + i\Gamma_{ng}} + \frac{1}{\omega - \omega_{n'g} + i\Gamma_{n'g}} \right] \right\} \end{aligned} \quad (5.9)$$

with

$$M = (r_x)_{gn}(r_y)_{nn'}(r_z)_{n'g} + (r_x)_{gn}(r_z)_{nn'}(r_y)_{n'g}. \quad (5.10)$$

After changing the summation to the integral, we will use the following assumptions:

- 1- The matrix elements are constant within the range of the integration. In this way we are able to bring the matrix elements out of the integral. To calculate the matrix elements as a function of energy a better approximation method must be used.
- 2- We only use a valence band ( $\Gamma_8$ ) and two conduction bands ( $\Gamma_6$  and  $\Gamma_7$ ) of ZnSe.

The dispersion of both  $\Gamma_6$  and  $\Gamma_8$  are approximated by quadratic curves. They are

$$E_8(k) = -\frac{\hbar^2 k^2}{2m_8} + E_g \quad (5.11)$$

and

$$E_6(k) = \frac{\hbar^2 k^2}{2m_6}. \quad (5.12)$$

Here  $E_8$  and  $E_6$  are the energy bands of  $\Gamma_8$  (valence band) and  $\Gamma_7$  (lowest level conduction band), respectively.  $E_g$  is the optical band gap.  $m_8$  and  $m_7$  stand for electron mass of  $\Gamma_8$  and  $\Gamma_7$  bands. In these calculations  $\Gamma_7$  is taken to be flat, and

since  $\omega_{78}$  is  $\sim 3$  times larger than the band gap, we assume this value is also constant in the range of the integration.

3- All damping parameters are constant and equal.

With these assumptions the susceptibility can be reduced to a closed form

$$\begin{aligned}
\chi_{xyz}^{(2)} = & \left( \frac{-Ne^2 M}{\pi^2 \sqrt{\omega_g \hbar^2}} \right) \left( \frac{2\mu}{\hbar} \right)^{3/2} \\
& \left\{ \frac{-1}{(\hat{\omega} - \omega_{78} + i\hat{\gamma})} \right. \\
& \left. \begin{cases} \hat{k}_c - \sqrt{1 - 2\hat{\omega} - i\hat{\gamma}} \tan^{-1} \frac{\hat{k}_c}{\sqrt{1 - 2\hat{\omega} - i\hat{\gamma}}} & \text{if } \hat{\omega} < 0.5; \\ \hat{k}_c - \sqrt{2\hat{\omega} - 1 + i\hat{\gamma}} \tanh^{-1} \frac{\hat{k}_c}{\sqrt{2\hat{\omega} - 1 + i\hat{\gamma}}} & \text{if } \hat{\omega} > 0.5; \end{cases} \right\} \\
& + \frac{1}{(\hat{\omega} + \omega_{78} + i\hat{\gamma})} \left( \hat{k}_c - \sqrt{2\hat{\omega} + 1 + i\hat{\gamma}} \tan^{-1} \frac{\hat{k}_c}{\sqrt{2\hat{\omega} + 1 + i\hat{\gamma}}} \right) \\
& + \frac{1}{(\hat{\omega} - \omega_{78} + i\hat{\gamma})} \left( \hat{k}_c - \sqrt{1 + \hat{\omega} + i\hat{\gamma}} \tan^{-1} \frac{\hat{k}_c}{\sqrt{1 + \hat{\omega} + i\hat{\gamma}}} \right) \\
& + \frac{-1}{(2\hat{\omega} - \omega_{78} + i\hat{\gamma})} \left( \hat{k}_c - \sqrt{1 - \hat{\omega} - i\hat{\gamma}} \tan^{-1} \frac{\hat{k}_c}{\sqrt{1 - \hat{\omega} - i\hat{\gamma}}} \right) \\
& + \frac{1}{(2\hat{\omega} + \omega_{78} + i\hat{\gamma})} \left( \hat{k}_c - \sqrt{1 + \hat{\omega} + i\hat{\gamma}} \tan^{-1} \frac{\hat{k}_c}{\sqrt{1 + \hat{\omega} + i\hat{\gamma}}} \right) \\
& + \frac{2\hat{\omega} - \hat{\omega}_{67} + 2i\hat{\gamma}}{2\hat{\omega} - \hat{\omega}_{67} + i\hat{\gamma}} \frac{1}{(2\hat{\omega} + \omega_{78} + i\hat{\gamma})} \\
& \left. \left( \hat{k}_c - \sqrt{1 - \hat{\omega} - i\hat{\gamma}} \tan^{-1} \frac{\hat{k}_c}{\sqrt{1 - \hat{\omega} - i\hat{\gamma}}} \right) \right\} \tag{5.13}
\end{aligned}$$

where  $k_c$  is the cutoff wavevector and

$$\hat{k}_c = k_c \sqrt{\frac{\hbar}{2\omega_g \mu}},$$

$$\hat{\omega} = \frac{\omega}{\omega_g},$$

$$\hat{\gamma} = \frac{\Gamma}{\omega_g}$$

and

$$\mu^{-1} = m_8^{-1} + m_6^{-1}.$$

In Fig. 5.6 we have fit the lower energy part of the data to Eq. (5.13). The best value for  $\hat{k}_c$  and  $\hat{\gamma}$  were found to be .08 and .011, respectively.

The lower energy side of the curve agrees with the calculation within the experimental accuracy. However, the experimental results of the higher energy side of the resonance disagree with the computations. This could result from higher energy non-resonant contributions to  $\chi^{(2)}$ . Thus, a better model which includes variable matrix elements and the higher energy transition such as  $E_1$ , and  $E_1 + \Delta_1$  must be considered.

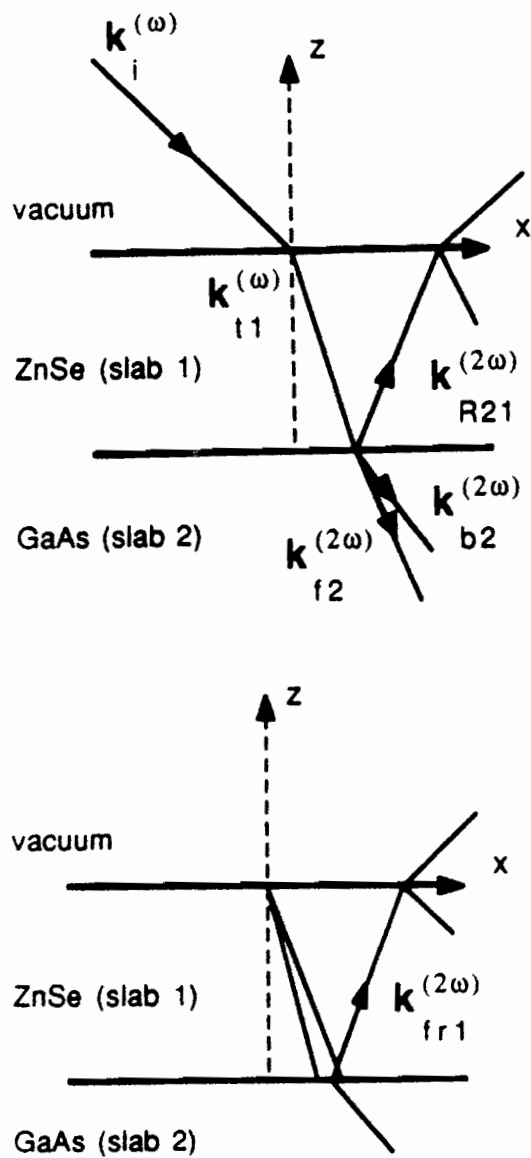


Figure 5.1: Simplified coordinate system that defines the boundaries and the direction of fundamental and second-harmonic electric fields for the case of the two slab problem. All angles between the wavevectors and  $z$ -axis are positive and less than  $90^\circ$ .

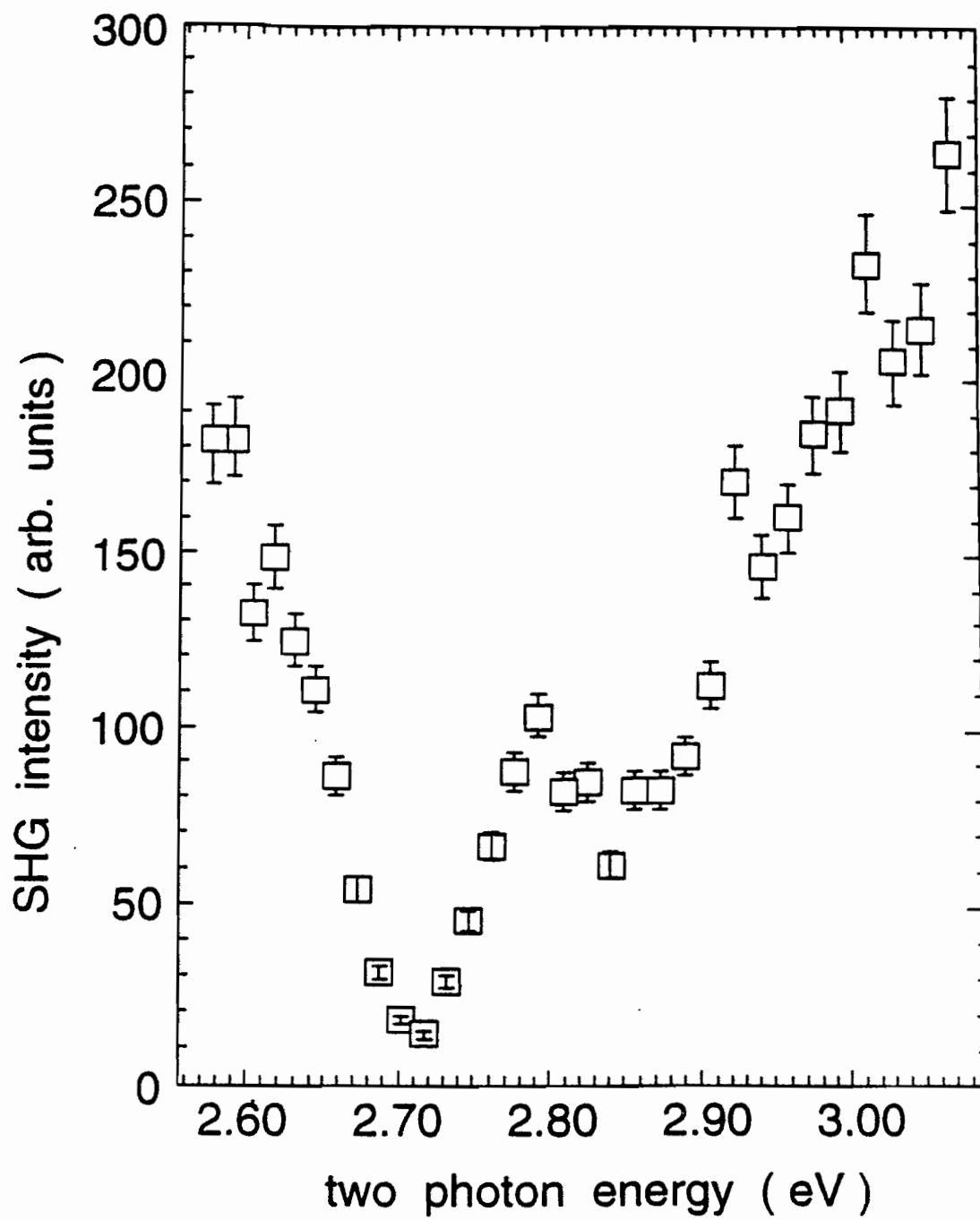


Figure 5.2: Normalized SH intensity signals from the bulk of our ZnSe/GaAs(001) sample as a function of two photon energy. The ZnSe overlayer thickness was 215 Å. The error bars represent the range of values obtained from several measurements.

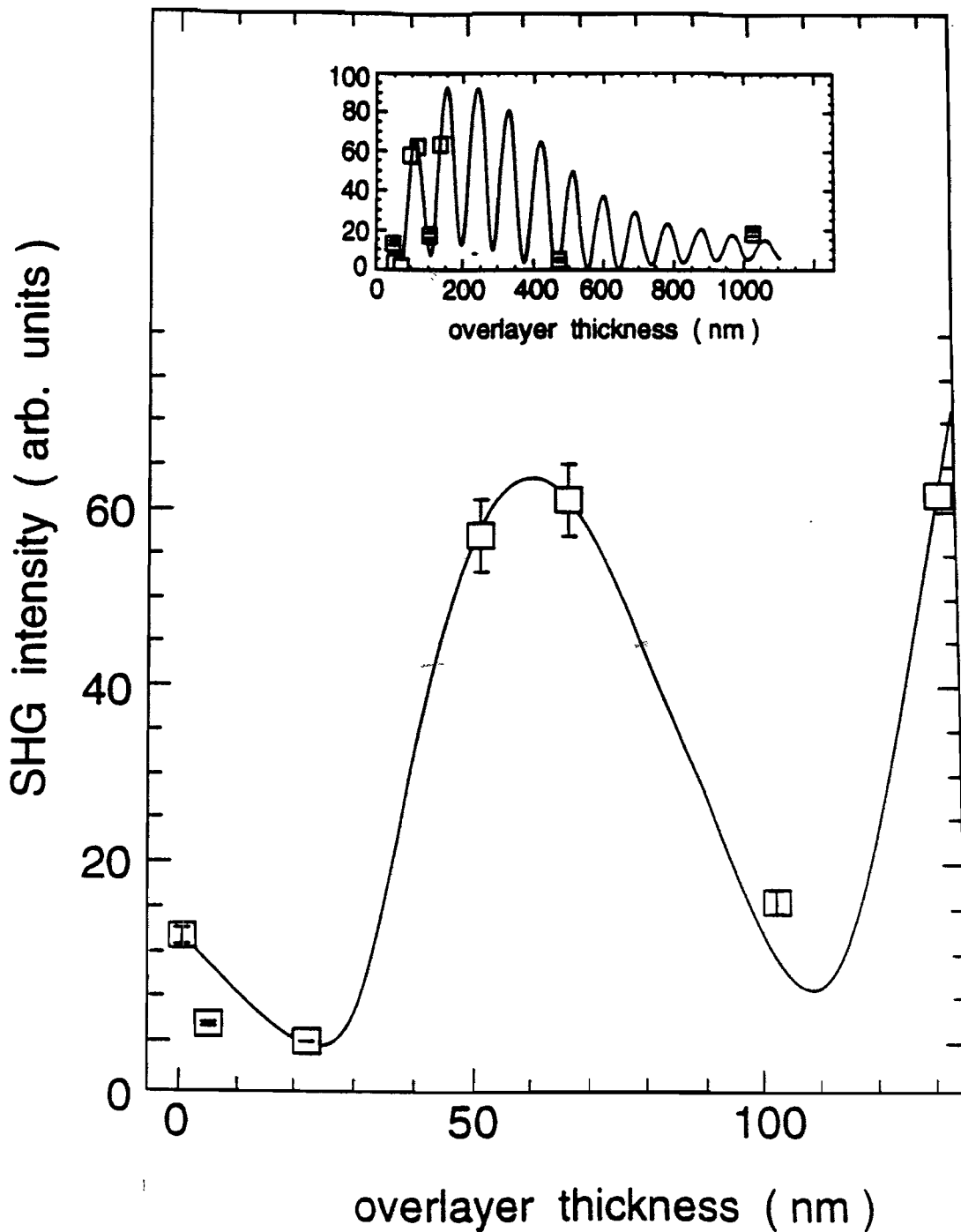


Figure 5.3: Variation in the the normalized SH intensity reflected from ZnSe/GaAs(001) as a function of the overlayer thickness at 2.67 eV. The solid line is a theoretical fit using Eq. (5.4). The lower portion of the figure is a reproduction of the overlayer data for a smaller range of thicknesses.

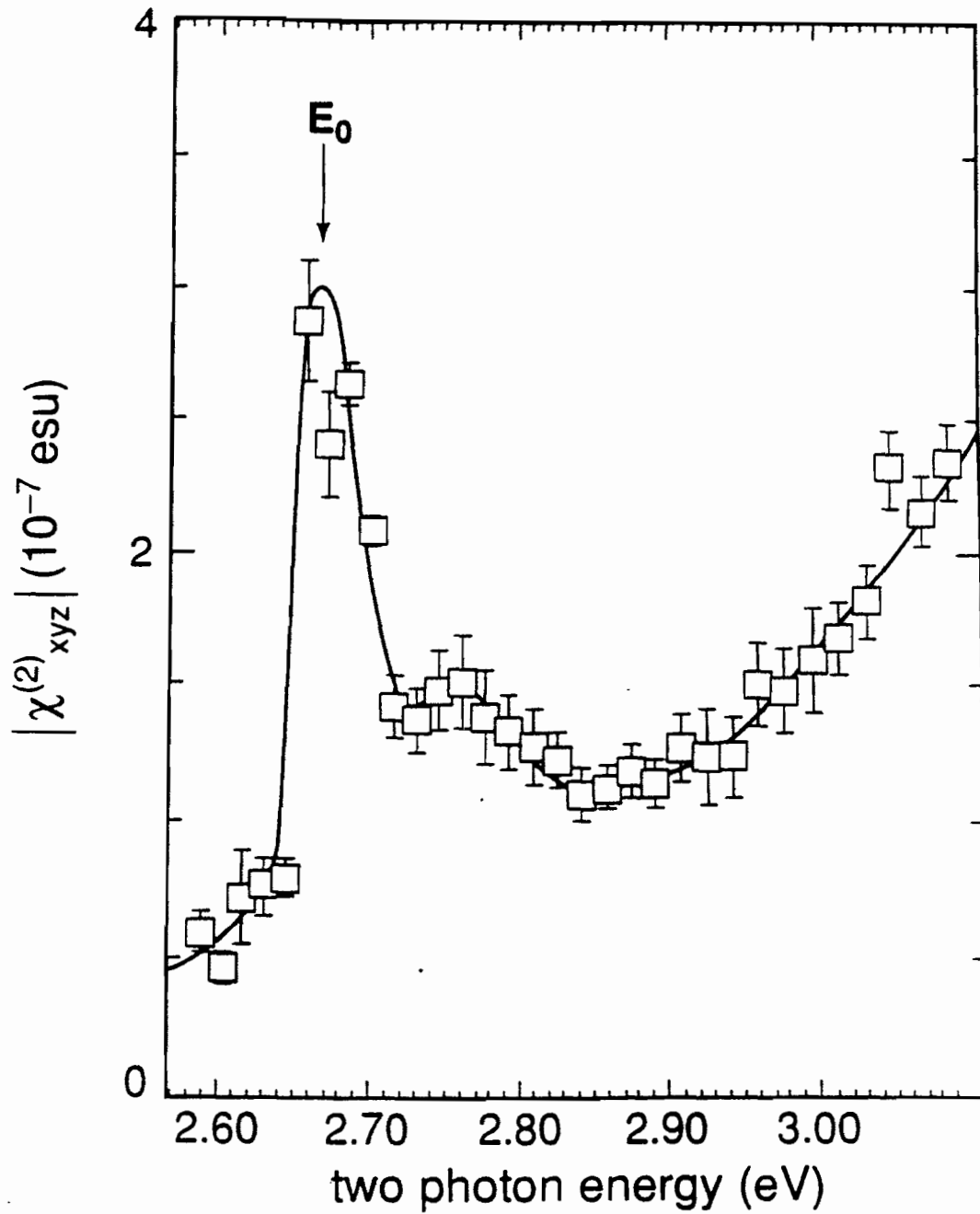


Figure 5.4: Magnitude of the second-order susceptibility of the bulk ZnSe(001) for energies between 2.6 and 3.1 eV. The solid lines are only a guide for the eye.

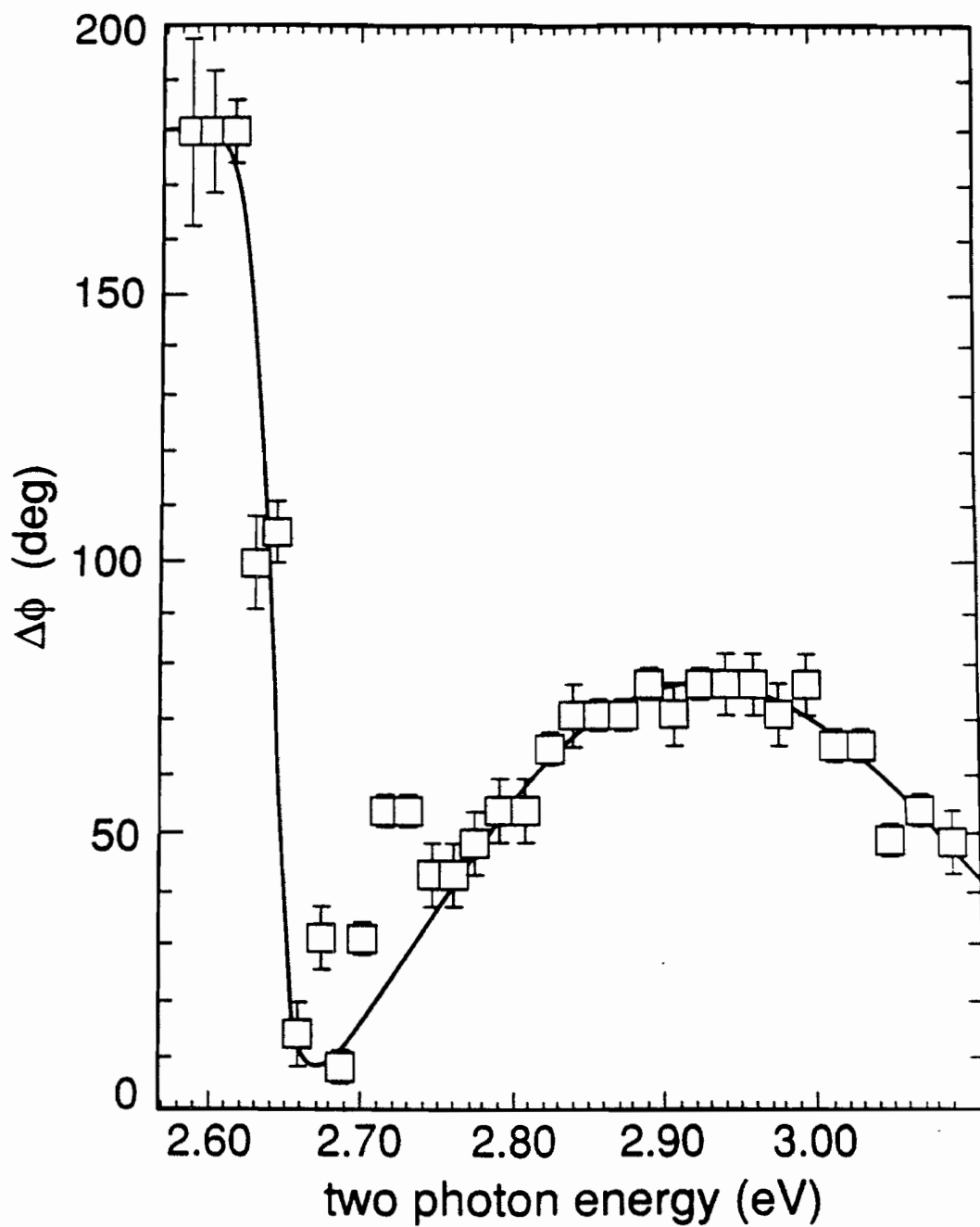


Figure 5.5: The relative phase of ZnSe susceptibility with respect to  $\chi_{xyz}^{(2)}$  of GaAs. The solid lines are only a guide for the eye.

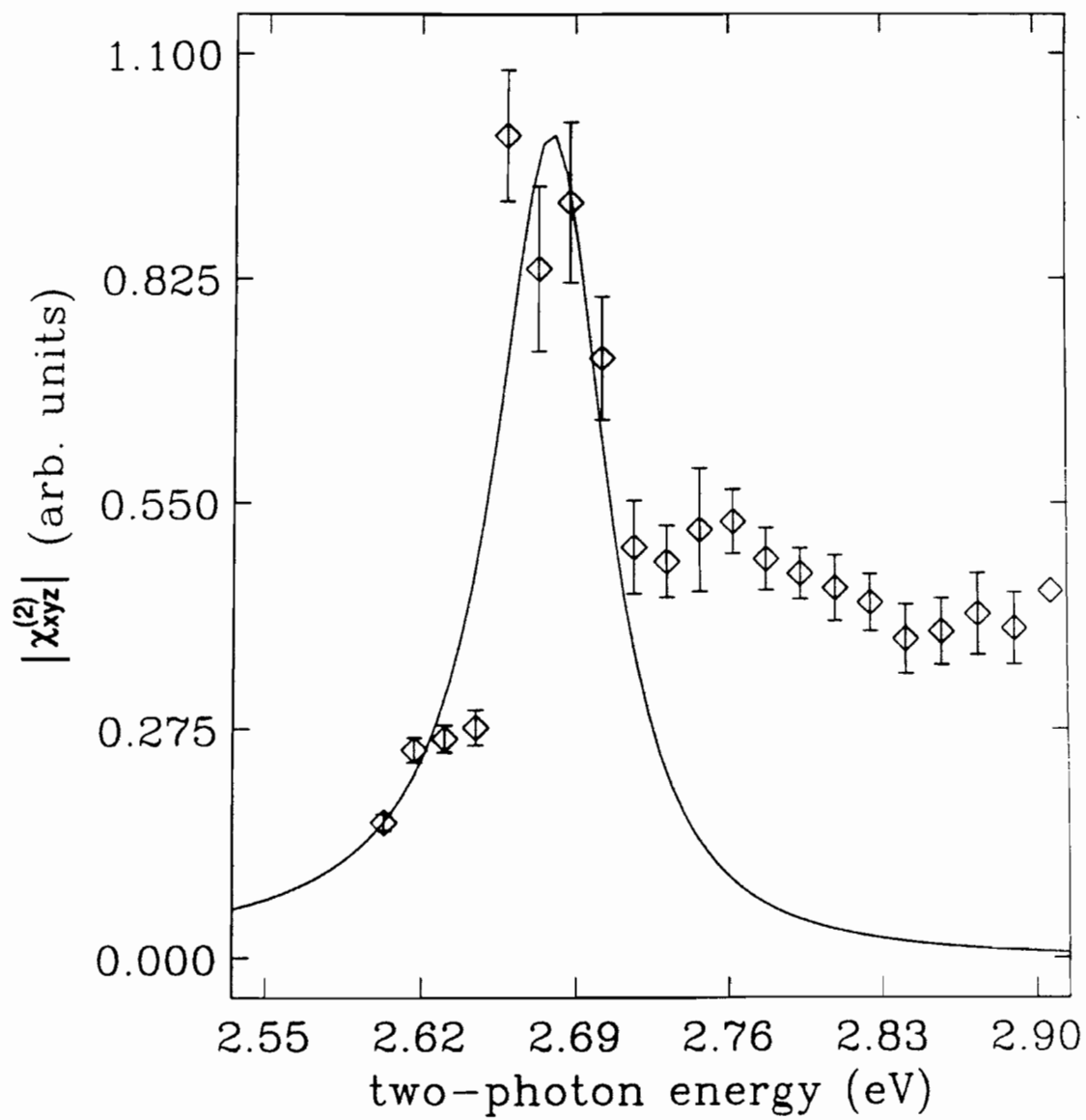


Figure 5.6: Calculated  $\chi_{xyz}^{(2)}$  of ZnSe (solid line) is compared to the experimental results.

# Chapter 6

## The Interface

The macroscopic properties of a solid/solid system strongly depend on the microscopic characteristics of the junction, and in particular the electronic structure of the interface. This chapter will describe the SHG and SFG experiments designed to probe the electronic structure of ZnSe/GaAs heterointerfaces.

### 6.1 SHG Experiments and Results

To detect the interface signal we have used a P-in/P-out polarization configuration and have oriented the sample such that the [001] direction was parallel to the plane of incidence ( $\phi = 0$ ). The details of the experimental set-up are described in Chapter 2. The interfacial and bulk SHG spectra for samples with thickness of 215 Å as a function of upconverted photon energy is shown in Fig. 6.1. Since the thickness of this sample is less than the critical thickness (see Chapter 7), it is pseudomorphic

and free of misfit dislocations. The interfacial SH spectra of this heterostructure exhibits sharp features at 2.92 and 2.72 eV. These two features were not observed in the bulk SH spectra (Fig. 6.2). To understand these interesting spectral differences we have performed a series of experiments which will be explained below.

## 6.2 Two-photon Resonance

It was shown that the second-order susceptibility, and thus, the second-order non-linear signals could have a resonance if the photon energy of the input beam (fundamental) or output beam (upconverted) matched a transition in the system. The first case is one-photon resonance and the second case is two-photon resonance. To identify the type of resonance, one must perform SFG and SHG experiments and compare the data as a function of one- and two-photon energy. We have compared the SFG and SHG spectra as a function of one- and two-photon energy for the sample with a 215 Å overlayer thickness in Fig. 6.3 and Fig. 6.4, respectively. It is evident that both the interfacial features in the SF and SH spectra match when the data is plotted as a function of two-photon energy. This identifies that the features at 2.72 and 2.92 eV are two-photon resonances, and therefore, transitions with energy splittings of  $\sim 2.72$  and  $\sim 2.92$  eV in ZnSe/GaAs heterostructure exist. In order to obtain a better understanding of the physical phenomena of these transitions, their spatial and spectral origins must be identified.

## 6.3 Spatial Origin

The interface signals, in principle, can contain contributions from the surface and/or higher-order bulk nonlinearities. It was not possible to measure these contributions using thick ZnSe samples ( $> 2\mu m$ ), because these samples exceeded the critical thickness ( $\sim 1500 \text{ \AA}$ ), and therefore, were no longer pseudomorphic. Consequently, we undertook different experiments to investigate these effects.

### 6.3.1 Surface Contribution

First, we modified the surface by chemical etching to check the contribution of the front surface to the signal. We had etched the surface using a solution of  $\text{NH}_4\text{Cl}$  in water (55 g/l) and  $\text{HCl}$  in water (1/3 by volume). Auger electron spectroscopy (Fig. 6.5) and scanning electron microscopy revealed that the front surface was roughened and chemically modified. The SH spectra of the sample, before and after chemical etching, are shown in Fig. 6.6. There is no detectable change in the signals.

In another experiment we sputtered the front surface with an  $\text{Ar}^+$  beam in a UHV chamber. The SHG spectra remained qualitatively unchanged. These results indicate that the SH signals are not very sensitive to variation of the front surface.

### 6.3.2 Higher Order Bulk Contribution

In Chapter 2, we showed that the isotropic contribution of higher order nonlinearity,  $\zeta$ , can be detected by a SHG experiment with an S-in/S-out beam polarization

configuration. Our data, shown in Fig. 6.7, show that the bulk anisotropic contribution was not detectable since it was less than the level of the noise of the system. We also have measured the contribution of the linear combination of  $\gamma$  and  $\chi_{|| \perp}^{(2)}$  in an S-in/P-out polarization configuration (see Chapter 2). This contribution was  $\sim 40$  times smaller than that of the interface signal, seen in Fig. 6.7. In summary, it is evident that the signal does not originate from the surface or higher order bulk nonlinearity.

## 6.4 Thickness Dependent Measurements

In the course of this work it was discovered that the thickness dependent SH measurement was a valuable tool to investigate the spatial origin of the signals. *Signals with different spatial origin behave differently as a function of the overlayer thickness.* To illustrate this fact we can consider the following examples.

### 6.4.1 Bulk Data

We have seen already that bulk SH signals oscillate as a function of the overlayer thickness. The oscillation was produced from nonlinear interference. We have introduced this interference phenomena as a new method to measure the second-order susceptibility of the ZnSe overlayer (for more details see Chapter 5).

## 6.4.2 Interfacial Resonance at 2.92 eV

The intensity of the interfacial resonance at 2.92 eV decreases almost exponentially with respect to thickness of the ZnSe overlayer. This behavior suggests that the signal is generated in the buried GaAs and decays in the ZnSe overlayer. In this section we will describe a simple model that can predict this thickness dependent behavior. In this model we will take the ZnSe overlayer as an absorbent medium, and assume that the signal is generated at the interface or below the junction.

Consider the geometry shown in Fig. 6.8, where the ZnSe/GaAs junction is at  $z = 0$  and the air/ZnSe interface is at  $z = d$ .  $d$  is the thickness of the ZnSe overlayer. With the beam polarization parallel to the plane of incidence (S polarization), we can write

$$\frac{E_{total}^{(2\omega)}}{E_0^{(2\omega)}} = t_{10}e^{i\phi_1} + t_{10}r_{10}r_{12}e^{i\phi_1}e^{i\phi_2} + t_{10}r_{10}^2r_{12}^2e^{i\phi_1}e^{2i\phi_2} + \dots \quad (6.1)$$

with

$$t_{10} = \frac{2n_1 \cos \theta_1}{\cos \theta_1 + \cos \theta_0}, \quad (6.2)$$

$$r_{10} = \frac{n_1 \cos \theta_0 - n_0 \cos \theta_1}{n_1 \cos \theta_0 + n_0 \cos \theta_1}, \quad (6.3)$$

$$r_{12} = \frac{n_1 \cos \theta_2 - n_2 \cos \theta_1}{n_1 \cos \theta_2 + n_2 \cos \theta_1}, \quad (6.4)$$

$$\phi_1 = \frac{4\pi d}{\lambda}(n_1 \cos \theta_1 - \cos \theta_0) \quad (6.5)$$

and

$$\phi_2 = \frac{4\pi d}{\lambda} \cos \theta_1 n_1. \quad (6.6)$$

$E_0^{(2\omega)}$  is the second harmonic field, generated in GaAs, at the ZnSe side of the junction.  $n_i$  is the complex index of refraction (i.e.  $n_i = \sqrt{\epsilon}$ ) and all angles are shown in Fig. 6.8. Eq. (6.1) reduces to a closed form

$$\frac{E_{total}^{(2\omega)}}{E_0^{(2\omega)}} = \frac{t_{10}e^{i\phi_1}}{1 - r_{10}r_{12}e^{i\phi_2}}. \quad (6.7)$$

This shows that for small reflectivity Eq. (6.7) reduces to a *purely exponential* form. The effect of the multiple reflection is to mix the exponential with an oscillation. The intensity of  $E_{total}^{(2\omega)}$  along with the experimental results is displayed as a function of thickness in Fig. 6.8. The theoretical curve for  $E_{total}^{(2\omega)}$  was generated using the following parameters [54, 55]:

$$\epsilon_{GaAs} = 18.18 + i18.1 \text{ and } \epsilon_{ZnSe} = 8.087 + i0.826 \text{ at } \lambda = 425 \text{ nm.}$$

The angle  $\theta_0$  is 75 degrees and all other angles were found by Snell's relationships. The only adjustable parameter in this computation is the amplitude of the intensity at  $d = 0$ . The theoretical calculation matches the second-harmonic intensity at 2.92 eV within the experimental accuracy. This agreement suggests that the origin of the interfacial resonance at 2.92 eV is in GaAs. The energy of this feature is consistent with the  $E_1$  transition of GaAs [56] and we therefore have assigned it to the  $E_1$  transition in the buried GaAs.

### 6.4.3 Interfacial Resonance at 2.72 eV

The behavior of the 2.72 eV resonance is more complicated than for the above two cases. The SHG intensity as a function of overlayer thickness is displayed in Fig. 6.9.

The solid line is the prediction of the thickness dependent intensity based on a model similar to the bulk, where the susceptibility was assumed to be uniform through the overlayer. In this calculation GaAs was taken as a linear medium. The experimental results are much different when compared to those calculated. A close inspection of the data also shows that the thickness dependent behavior cannot be explained by the simple exponential model described in Sec. 6.4.2.

In another model we assumed that the susceptibility has its maximum value at the interface and decays exponentially with distance from the junction. The motivation for this model was described in Chapter 2 and in Appendix C. The result of this calculation is shown by a dotted line in Fig. 6.9. Even though this result is closer to the experimental results than the previous model, it still does not describe the dependence of the 2.72 resonance as a function of the overlayer thickness. The failure of these models to accurately predict this dependence indicates that the signal at 2.92 eV and 2.72 eV and the bulk have different spatial origins and are intrinsically different.

## 6.5 Spectral Origin

We will now discuss the spectral origin of the 2.72 eV interfacial resonance. In this section, the effect of the deformation potential on the bulk signal will be described. We will then present the band profile of ZnSe/GaAs and show that the 2.72 eV resonance feature is a result of the coupling of the valence band to the quantum well

resonance state, and not due to the strain in the system.

### 6.5.1 The Effect of the Deformation Potential

The ZnSe/GaAs(001) system contains a small lattice mismatch that produces a deformation potential within the heterostructure. This deformation potential produces a tetragonal distortion of the ZnSe unit cell and gives rise to a biaxial compressive strain in the layer. As a result, the four-fold degenerate valence band of the ZnSe,  $\Gamma_8$ , splits to two two-fold degenerate bands [70]. The conduction bands,  $\Gamma_6$  and  $\Gamma_7$ , cannot split, but they can shift in energy. The optical transitions and band splitting of the system are shown in Fig. 6.10. This mechanism will change the optical band gap of the overlayer. Under these conditions it is essential to investigate the effect of the deformation potential on the SHG signal. The deduced  $\chi_{xyz}^{(2)}$  from the bulk of the ZnSe overlayer is shown, along with the interface SH intensity data in Fig. 6.11. The bulk resonance at 2.67 eV, corresponding to the  $E_0$  transition is shifted by  $\sim 50$  meV with respect to the interface feature. It is natural to ask if the SHG signal at 2.72 eV is the bulk signal with a shift in energy resulting from the deformation potential. To answer this question we must compute the shift in band gap energy of ZnSe as a function of the strain.

We start the computation with the orbital-strain perturbation Hamiltonian,  $H_c$ , for tetragonal symmetries introduced by Pikus and Bir [71, 72]

$$H_c = -a(\epsilon_{xx} + \epsilon_{yy} + \epsilon_{zz}) - 3b[(L_x^2 - \frac{1}{3}L^2)\epsilon_{xx} + c.p.] \quad (6.8)$$

where  $\epsilon_{ij}$  represents the components of the strain tensor and  $L$  is the angular-momentum operator. "c.p." denotes cyclic permutation with respect to the indices  $x, y$ , and  $z$ . The parameters  $a$  and  $b$  are the hydrostatic and shear potential, respectively. For biaxial stress parallel to the  $[100]$  and  $[010]$  directions, the strain tensor is

$$\epsilon = \begin{pmatrix} -\epsilon & 0 & 0 \\ 0 & -\epsilon & 0 \\ 0 & 0 & 2\epsilon C_{12}/C_{11} \end{pmatrix} \quad (6.9)$$

where  $C_{ij}$  stands for the elastic stiffness of the ZnSe overlayer. This reduces the Hamiltonian to

$$H_\epsilon = 2a\epsilon\left(1 - \frac{C_{12}}{C_{11}}\right) - 3b\epsilon\left(1 + \frac{2C_{12}}{C_{11}}\right)\left(L_z^2 - \frac{1}{3}L^2\right) \quad (6.10)$$

A. Gavinián and M. Cardona [73] calculated the eigenvalue of this strain Hamiltonian using the unperturbed wave function of the valence and conduction bands in a zinc blende-type material. The results of the perturbation calculations are

$$\Delta E_0(1) = \left[-2a\left(\frac{C_{11} - C_{12}}{C_{11}}\right) + b\left(\frac{C_{11} + 2C_{12}}{C_{11}}\right)\right]\epsilon, \quad (6.11)$$

$$\Delta E_0(2) = \left[-2a\left(\frac{C_{11} - C_{12}}{C_{11}}\right) - b\left(\frac{C_{11} + 2C_{12}}{C_{11}}\right)\right]\epsilon \quad (6.12)$$

and

$$\Delta(E_0 + \Delta_0) = -2a\left(\frac{C_{11} - C_{12}}{C_{11}}\right)\epsilon. \quad (6.13)$$

Using the following values for these parameters,

$$C_{11} = 0.826 \times 10^6 \text{ Kg/cm}^2, \quad C_{12} = 0.498 \times 10^6 \text{ Kg/cm}^2, \quad a = -4.25 \text{ eV}, \quad b = -0.40 \text{ eV},$$

and  $\epsilon = 3. \times 10^{-3}$  [74, 75, 76], we deduce the energy shift to be

$$\Delta E_0(1) = 7.0\text{meV},$$

$$\Delta E_0(2) = 13.0\text{meV},$$

and

$$\Delta(E_0 + \Delta_0) = 10.0\text{meV}.$$

It is clear that the energy shift in the bulk susceptibility with respect to the interface spectra is  $\sim 4\times$  too large to be attributed to the measured strain in the system. Therefore the deformation potential could not be responsible for the shift between the bulk and interface features.

## 6.6 A New Picture of the Interface: Band Bending

Both spectral and spatial inconsistencies of the 2.72 eV resonance signal led us to the development of a new picture for this effect. It is known that Zn and Ga diffuse across the buried interface during growth [77]. The diffusion length for Ga (Zn) in ZnSe (GaAs) is about 30 Å (100 Å), so that relatively high dopant densities arise near the interface [32]. Because Zn is an acceptor in GaAs and Ga is a donor in ZnSe, their diffusion produces an intrinsic band bending at the interface (see Fig 6.12). As a result of this band bending an interfacial quantum well forms in the

GaAs conduction band. Quantum wells at hetero-interfaces have been produced and studied in other systems [5, 6, 7]. The ZnSe/GaAs heterojunction differs from most previous observations because the donors and the acceptors are *generated during growth by interdiffusion* across the junction. In our system a resonant electronic state with energy higher than the conduction band of ZnSe exists in the quantum well. An attractive explanation for the resonance thus presents itself. The SHG feature at 2.72 eV corresponds to a virtual cross-over transition between the interfacial quantum well state and the ZnSe valence band. A cross-over excitation [78, 79, 80] is a transition between two states whose density of states (DOS) is provided by two spatially *separated* materials. This kind of transition can arise when the wave functions of the terminal states extend beyond the interface. Then the states can be directly coupled by photoexcitation. Ultrasensitive electrolyte electroreflectance (EER) measurements in doped ZnSe/GaAs systems have independently revealed the existence of a cross-over transition [32]. This transition is always blue-shifted by 40-60 meV with respect to the ZnSe  $E_0$  transition.

Within the dipole approximation, SFG and SHG processes involve three electronic transitions (real or virtual) in the media. Since the observed feature is resonant with the upconverted (output) photon, the effect of the *input* field is to transfer an electron (virtually) from the ZnSe valence band to the quantum well state. This excitation process can take place via several different pathways, but the final resonant step of the SFG or SHG process involves some charge transfer ac

interface. In contrast to the EER measurements, the cross-over SH resonance is a virtual transition, has nearly zero background, and possesses a nonlinearity that is comparable in magnitude to the bulk  $\chi_{xyz}^{(2)}$ . We speculate that because the virtual transition is accompanied by a substantial charge transfer *across* the interface, a large permanent dipole moment in the intermediate state can arise and enhance the second-order nonlinearity. Regardless of its origin, the strong nonlinearity enables us to conduct more detailed experiments on the phenomena.

## 6.7 The Interfacial Quantum Well in ZnSe/GaAs Heterointerface: A Theoretical Model

We have established that the interfacial SHG resonance at 2.72 eV resulted from a virtual coupling between the ZnSe valence band and the resonance state of the quantum well. However, there are still some interesting problems that remain unsolved, namely, the existence of bond states in the quantum well, the charge distribution, the effect of the perturbation on the quantum well, and the type of SH process (i.e. two- or three-level processes). We have constructed a simple theoretical model to study the electronic energy levels of the quantum well. This model provides an approximated solution to the above problems and is described in this section.

Within the effective mass approximation, electronic motion is governed by the

Schrodinger equation [10]

$$-\frac{\hbar^2}{2} \nabla \frac{1}{m(r)} \nabla \psi(r) + V(r)\psi(r) = E\psi(r). \quad (6.14)$$

If an electron is free in the plane parallel to the interface (i.e.  $xy$ -plane), the potential is

$$V(r) = V(z) \quad (6.15)$$

where  $z$  is zero at the surface of the ZnSe and is equal to  $d$  at the interface. This leads to the wavefunction

$$\psi(r) = \frac{1}{\sqrt{A}} e^{i(k_x x + k_y y)} \phi(z) \quad (6.16)$$

where  $A$  is the sample area. With  $k_x = k_y = 0$  (center of the B.Z.) Eq. (6.14)

reduces to

$$-\frac{\hbar^2}{2} \frac{\partial}{\partial z} \frac{1}{m(z)} \frac{\partial}{\partial z} \phi(z) + V(z)\phi(z) = E\phi(z), \quad (6.17)$$

with

$$m(z) = \begin{cases} m_{ZnSe}, & \text{if } z < d; \\ m_{GaAs}, & \text{if } z > d. \end{cases} \quad (6.18)$$

The continuity condition states that  $\phi(z)$  and  $[1/m(z)][\partial\phi(z)/\partial z]$  must be continuous at the junction of ZnSe and GaAs [81, 82, 83, 84, 85, 86, 87]. We rewrite Eq. (6.17) in a dimensionless form for each side of the junction

$$\frac{\partial^2 \phi(\zeta)}{\partial \zeta^2} = (e - v) \bar{m}_* \phi(\zeta) \quad (6.19)$$

with

$$\frac{z}{\zeta} = 10 \times a_0 \quad \text{where } a_0 = 0.529 \text{ \AA}, \quad \bar{m}_* = \frac{m}{10m_e}, \quad \text{and } R_y a_0^2 = \frac{\hbar^2}{2m_e}, \quad (6.20)$$

and also

$$\frac{E}{e} = mR_y,$$

$$\frac{V}{v} = mR_y \quad \text{where} \quad mR_y = 13.605 \text{ meV}.$$

The above dimensionless Schrodinger equation was solved numerically for the potential  $V(z)$  [88]. This potential will be described as follows. The value  $\Phi = -V(z)/e$  is the outcome of Poisson's equation with a given charge distribution. Kassel *et. al* [32] showed that the charge distribution at the interface can be described by a Gaussian function. In ZnSe the charge distribution is

$$\rho(z)_{ZnSe} = \frac{eN_{ZnSe}}{\lambda_{Ga}\sqrt{2\pi}} \exp\left(-\frac{(z-d)^2}{2\lambda_{Ga}^2}\right). \quad (6.21)$$

A similar charge distribution is written for the GaAs side of the junction

$$\rho(z)_{GaAs} = \frac{-eN_{GaAs}}{\lambda_{Zn}\sqrt{2\pi}} \exp\left(-\frac{(z-d)^2}{2\lambda_{Zn}^2}\right) \quad (6.22)$$

where  $N$  is the number density of the charge and  $\lambda$  is the diffusion length. To solve Poisson's equation,

$$-\nabla^2\Phi = \frac{1}{\epsilon}\rho, \quad (6.23)$$

we have used two boundary conditions at each side of the junction, namely  $\Phi_{junction-ZnSe}$  and  $\Phi_{surface-ZnSe}$  for the ZnSe side, and  $\Phi_{junction-GaAs}$  and  $\Phi_{bulk-GaAs}$  for the GaAs side, and solved Eq. (6.23) numerically. In this numerical method we have divided the distance coordinate  $z$  into a "mesh" of small segments of equal width,  $\delta z$ . Following is the conventional form for the parameters at the  $j$ th mesh point

$$z \rightarrow z_j \equiv j\delta z$$

$$\Phi(z) \rightarrow \Phi(z_j) \equiv \Phi_j$$

$$\rho(z) \rightarrow \rho(z_j) \equiv \rho_j.$$

Using this method, we can calculate  $\Phi_{j+1}$  as a function of  $\Phi_j$  and  $\Phi_{j-1}$ . This is shown as

$$\Phi_{j+1} = 2\Phi_j - \Phi_{j-1} - \rho'_j \quad (6.24)$$

where  $\Phi_j$  is the value of  $\Phi$  at the  $j$ th mesh point and  $\rho'$  is  $(\delta z)^2 \rho / \epsilon$  with mesh size  $\delta z$ . If we start the calculation from the surface of the ZnSe ( $j = 0$ ), then we need to know the value of  $\Phi_1$ . One can show that

$$\Phi_j = j\Phi_1 - (j-1)\Phi_0 - [(j-1)\rho'_1 + (j-2)\rho'_2 + \dots + \rho'_{j-1}]. \quad (6.25)$$

This gives the value of  $\Phi_1$  as a function of two boundary conditions,  $\Phi_0$  and  $\Phi_M$ , that is

$$\Phi_1 = \{\Phi_M + (M-1)\Phi_0 + [(M-1)\rho'_1 + \dots]\} / M \quad (6.26)$$

where  $M$  defines the last mesh point. The potential  $V = -e\Phi$  for the valence band and the conduction band are shown in Fig. 6.12. The parameters used for this computation are tabulated in Table 6.1.

### 6.7.1 Results of the Calculation

The wavefunction of the first three eigenstates of Eq. (6.17) are shown in Fig. 6.12. It should be noted that the system does not have any bound state and carries six

Table 6.1: Parameters used for band-profile calculations

Parameter	Value of the parameter
$N_{Ga}$	$8.5 \times 10^{12} \text{ cm}^{-2}$
$N_{Zn}$	$5.1 \times 10^{12} \text{ cm}^{-2}$
$\lambda_{Ga}$	4 nm
$\lambda_{Zn}$	10 nm
$\Phi_{ZnSe \text{ surface}}$	100 meV
$\Phi_{ZnSe \text{ interface}}$	180 meV
$\Phi_{GaAs \text{ interface}}$	370 meV

Table 6.2: Energy levels in the quantum well. Energies are measured relative to the conduction band of ZnSe.

Energy level	Energy (above the ZnSe conduction band)
$E_0$	18 meV
$E_1$	28 meV
$E_2$	54 meV
$E_3$	88 meV
$E_4$	124 meV
$E_5$	159 meV

distinct resonance states above the conduction band of ZnSe. The energy levels of these states are given in Table 6.2.

Here we are interested in calculating the dipole moment operator between the valence band state and the quantum well state. This calculation is essential for identifying the resonance state that is responsible for the observed peak at 2.72 eV. It requires knowledge of the wavefunction of the valence band. We have calculated a similar Schrodinger equation for the valence potential (see Fig. 6.12). The energy level of the resultant wavefunction is equal to the highest value in the valence band potential.

The matrix element was calculated as follows

$$\langle \Psi_{ex} | z | \Psi_g \rangle = \langle A_n \{ \phi_c \phi_2 \phi_3 \dots \} | z | A_n \{ \phi_v \phi_2 \phi_3 \dots \} \rangle = \langle \phi_c | z | \phi_v \rangle \quad (6.27)$$

where  $A_n$  is the antisymmetry operator and is applied to all the available electronic states of the system. We have computed the matrix elements of the dipole moment operator using calculated wavefunctions of the conduction band and the valence band. The result is shown in Fig. 6.13. As one can see, the strongest dipole transition is the transition between the valence band and the third energy level of the well.

It is interesting to compute the permanent dipole moment of the system. The result of this calculation will be used to determine the relative strength of the SHG signal in a *two-level* process [61]. To calculate the permanent dipole moment, we

start with the ground state permanent dipole moment,  $\mu_g$ ,

$$\mu_g = \langle A_n \{ \psi_v \psi_2 \psi_3 \dots \} | z | A_n \{ \psi_v \psi_2 \psi_3 \dots \} \rangle - \mu_{background} \quad (6.28)$$

where  $\mu_{background}$  is the background or the initial permanent dipole moment of the system. We can write a similar expression for the excited state permanent dipole moment,  $\mu_{ex}$ ,

$$\mu_{ex} = \langle A_n \{ \psi_c \psi_2 \psi_3 \dots \} | z | A_n \{ \psi_c \psi_2 \psi_3 \dots \} \rangle - \mu_{background}. \quad (6.29)$$

The resultant permanent dipole is thus,

$$\mu_g - \mu_{ex} = \langle \phi_v | z | \phi_v \rangle - \langle \phi_c | z | \phi_c \rangle. \quad (6.30)$$

The result of this calculation is shown in Fig. 6.14.

Now we assume that the SHG process, responsible for the interfacial resonance at 2.72 eV, is a two level process (see Chapter 4). Based on energy considerations, the above assumption is reasonable. Thus, we must calculate the relative oscillator strength of the signal for each quantum well state, namely

$$\{ |\langle \phi_v | z | \phi_c \rangle|^2 (\mu_g - \mu_{ex}) \}^2 \quad (6.31)$$

The result is shown in Fig. 6.15. It is clear that the third energy level in the quantum well is the strongest contributor to the SHG signal. This level is about 50 meV above the conduction band of ZnSe and is in good agreement with experimental results.

## 6.8 Lattice Relaxation As Detected by SHG Spectroscopy

Because of a small lattice mismatch between ZnSe and GaAs, there exists a tetragonal distortion in the ZnSe unit cell. As a result, a biaxial compressive strain is produced in the overlayer. This strain is represented by Eq (6.9) in Section 6.5.1. The elastic energy,  $E_\epsilon$ , associated with the elastic strain  $\epsilon$ , increases with ZnSe thickness according to [89]

$$E_\epsilon = \epsilon^2 B h \quad (6.32)$$

with

$$B = 2G(1 + \nu)/(1 - \nu) \quad (6.33)$$

where  $\nu$  is Poisson's ratio (i.e.  $2C_{12}/C_{11}$ ),  $G$  is the shear modulus, and  $h$  is the ZnSe overlayer thickness.

The increase in  $E_\epsilon$  with increasing  $h$  continues until there is enough energy to create a misfit dislocation at the interface (see Fig. 6.16). This process reduces  $\epsilon$  at the interface. J. W. Matthews defines the total misfit,  $f = \Delta a/a$ , [89] as

$$f = \epsilon + \delta. \quad (6.34)$$

Here the misfit is divided between the strain,  $\epsilon$ , and the dislocation,  $\delta$ . It is clear that with no dislocations,  $f = \epsilon$ . The largest value of  $h$  for which  $\delta = 0$  corresponds to the critical thickness,  $h_c$ . Samples with thickness less than  $h_c$  are free of dislocations and are pseudomorphic. The SHG spectra for various overlayer thicknesses are shown

in Fig. 6.17. Our data shows a marked change in the SHG spectra as the critical thickness is reached. All the samples with a thickness less than 1330 Å exhibited a peak at 2.72 eV; within our resolution, no spectral shift was observed. For samples thicker than 1330 Å, the intensity of this feature dropped and a new resonance appeared at 2.67 eV. In Fig. 6.18 the normalized peak intensity is plotted as a function of thickness. A transition between 1330 Å and 2000 Å is evident.

We will now interpret these observations. Misfit dislocations are produced at the buried interface as a result of an abrupt strain relaxation. These line defects are typically surrounded by a space-charge region [59, 90, 92, 93]. We expect the strong line charges at the interface to change the electric field such that the band bending on the ZnSe side of the heterointerface is altered drastically, and the resonance state of the quantum well vanishes. Since the SH resonance at 2.72 eV is due to virtual coupling of the resonance state of the quantum well and the valence band of the ZnSe, a substantial change in band bending leads to a marked reduction in the 2.72 eV SHG signal. Our thickness dependent data demonstrate that the lattice relaxation occurs when the overlayer thickness is greater than 1330 Å [Fig.( 6.18)]. This is in agreement with previous measurements of the critical thickness.

Yao *et al.* [28] measured the lattice parameter as a function of overlayer thickness utilizing x-ray diffraction. They found that the lattice parameter of ZnSe *abruptly* decreased to its bulk value at a thickness of 1500 Å. Mohammad and coworkers

[29] measured the thickness dependent strain in the ZnSe/GaAs(001) heterostructure. Their deduced strain from photo-luminescence (PL) and transmission electron microscopy (TEM) measurements suggested a critical thickness of 2000 Å. Unfortunately, we did not have access to samples with thicknesses between 1330 Å and 2000 Å, therefore, we were unable to identify the transition more precisely.

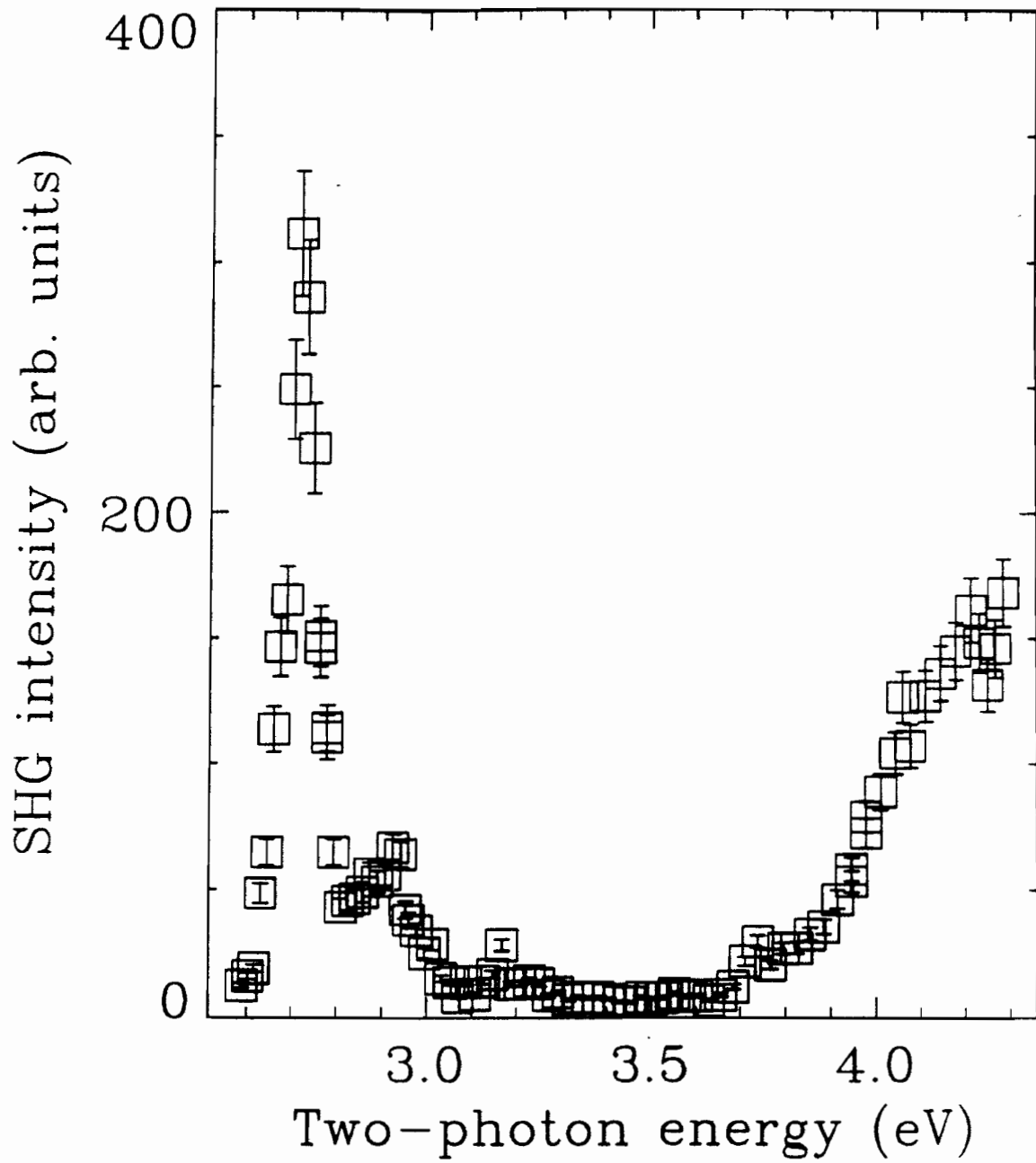


Figure 6.1: A typical interfacial SH spectrum of a ZnSe/GaAs(001) heterostructure. The spectra exhibits two sharp features at 2.92 and 2.72 eV. Thickness of the overlayer is 215 Å for this sample.

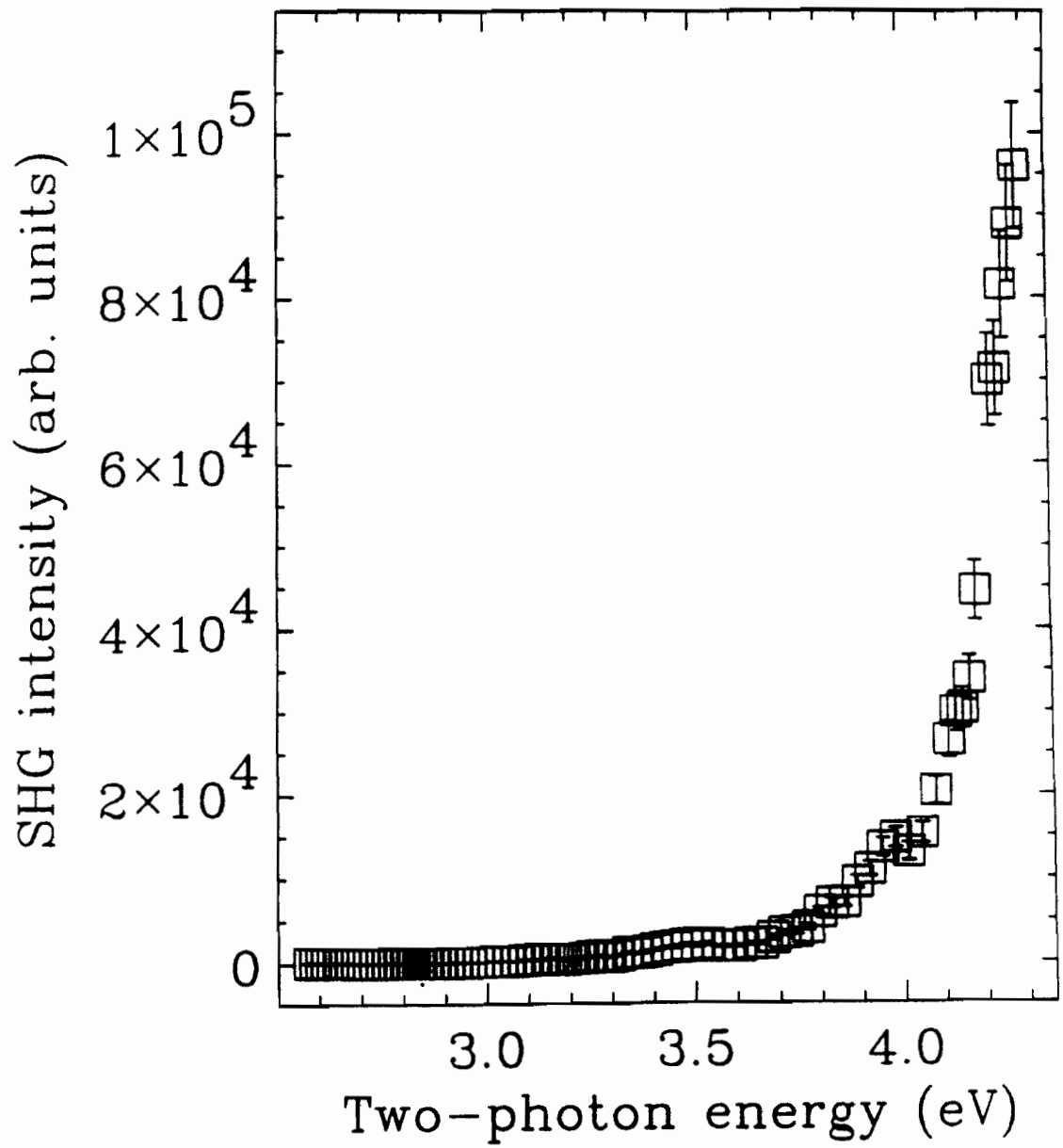


Figure 6.2: A typical SH spectra of a bulk ZnSe/GaAs(001) heterostructure. Thickness of the overlayer is 215 Å for this sample.

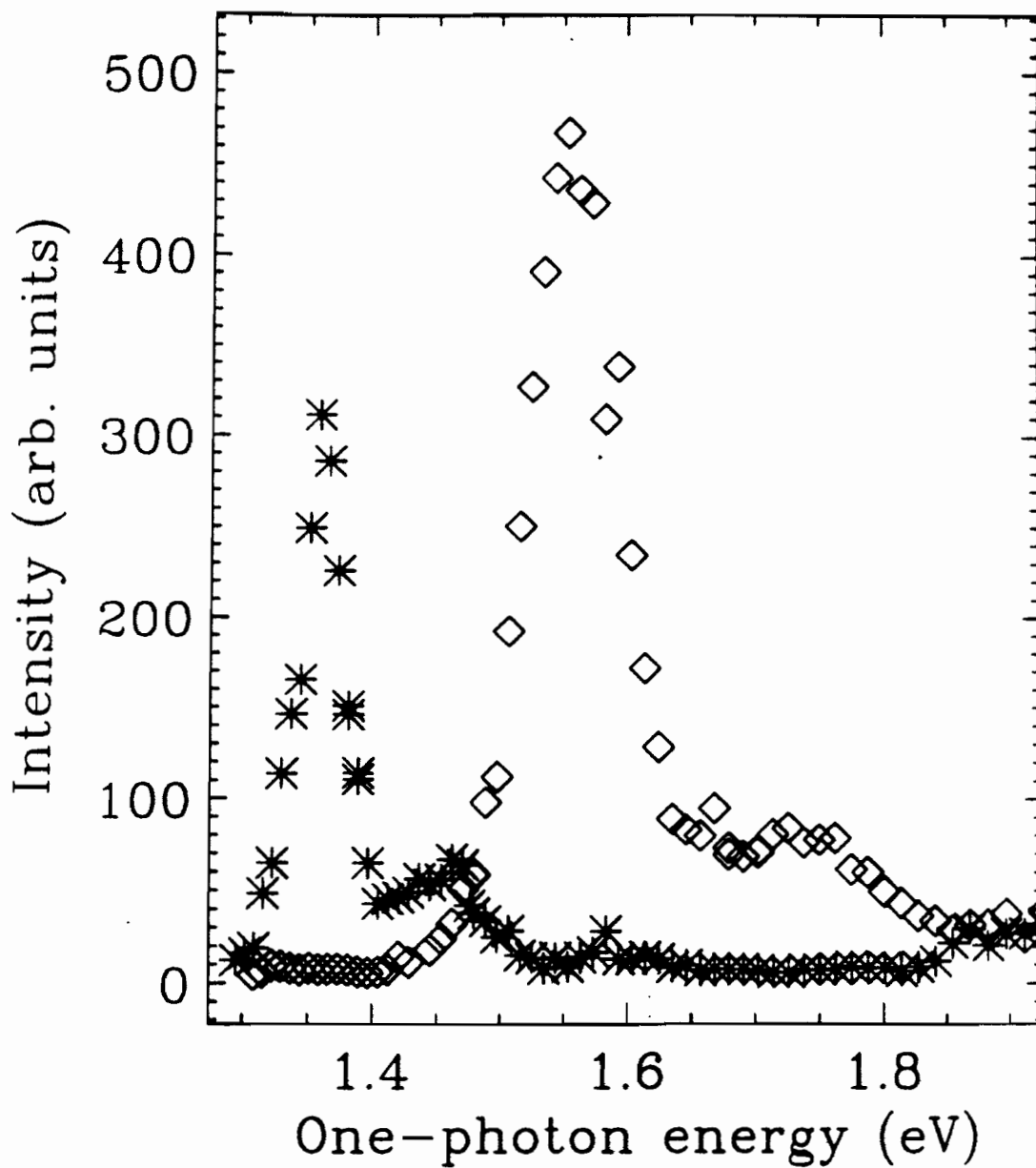


Figure 6.3: The variation of SH (\*) and SF ( $\diamond$ ) intensity as a function of one-photon energy. Thickness of the overlayer is 215 Å. It is clear that none of the features are one-photon resonance.

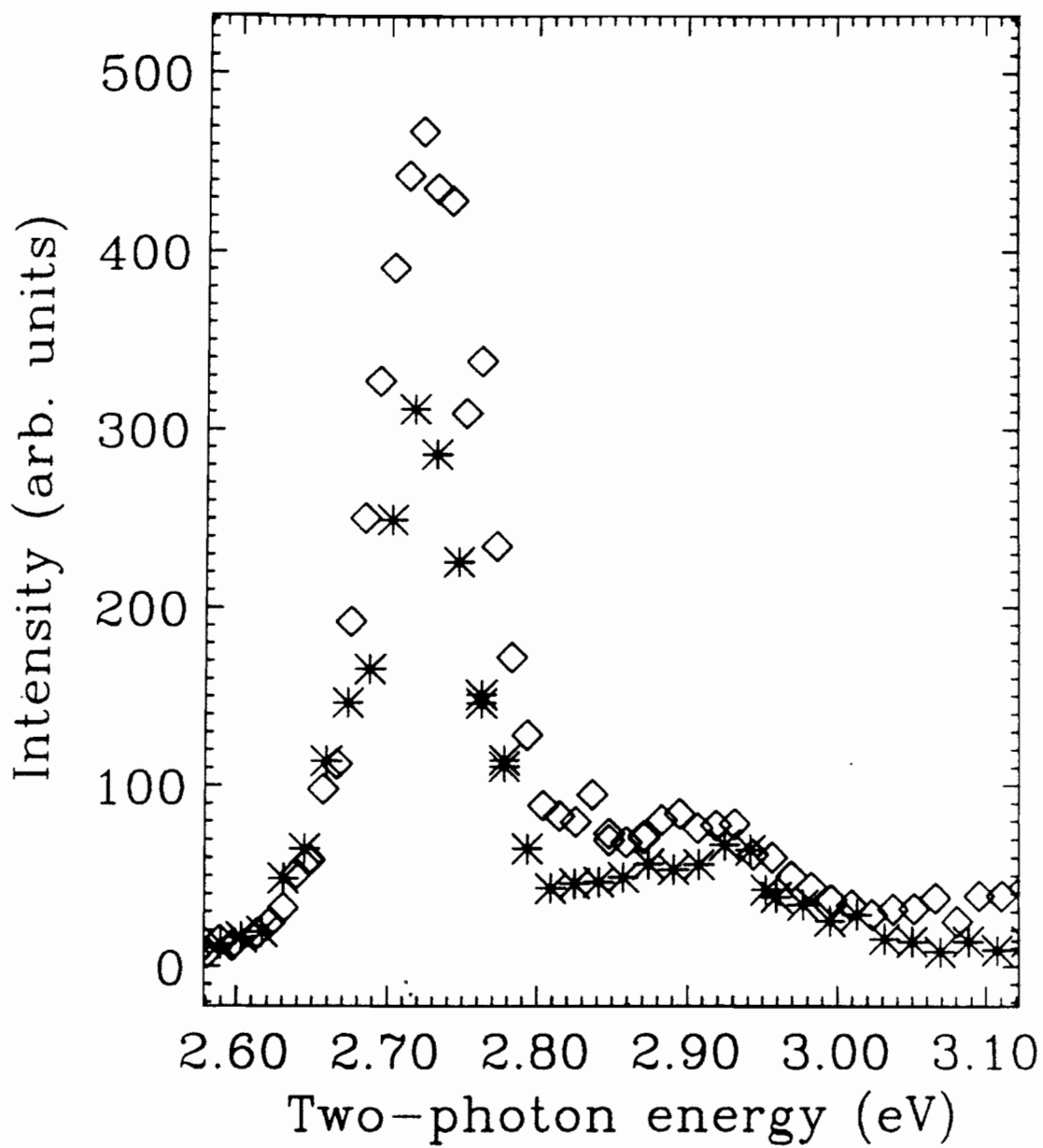


Figure 6.4: The variation of SH (\*) and SF (◇) intensity as a function of two-photon energy. This shows that both features are two-photon resonances.

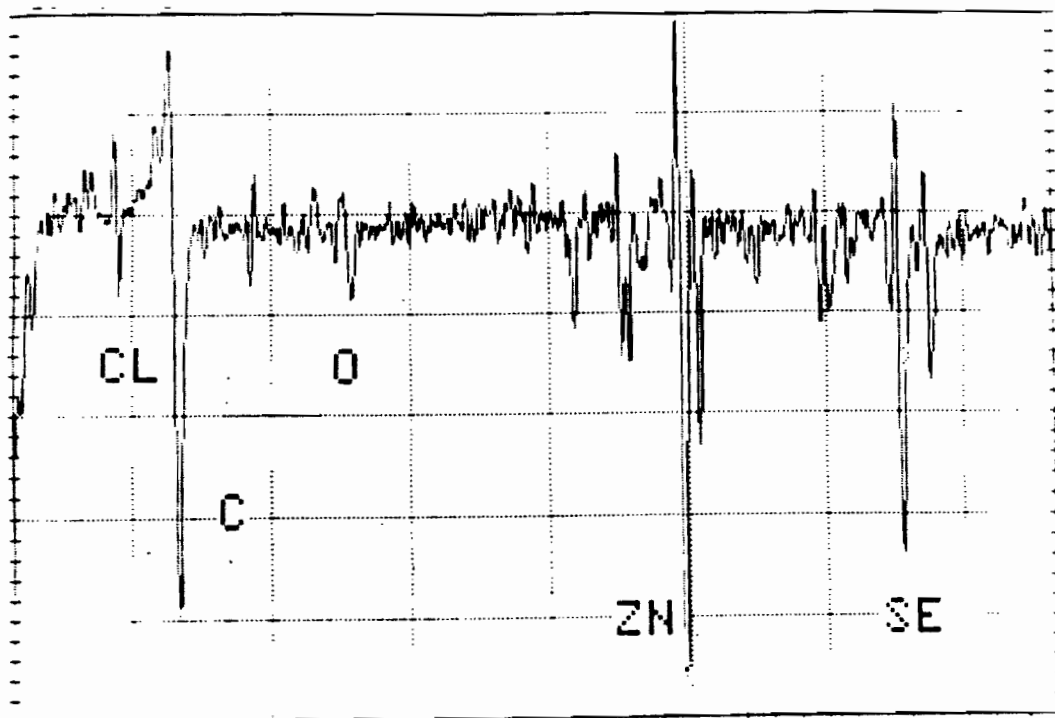


Figure 6.5: Auger electron spectroscopy of the etched sample. The spectrum suggests that there is C and Cl on the sample. These elements were introduced by chemical etching.

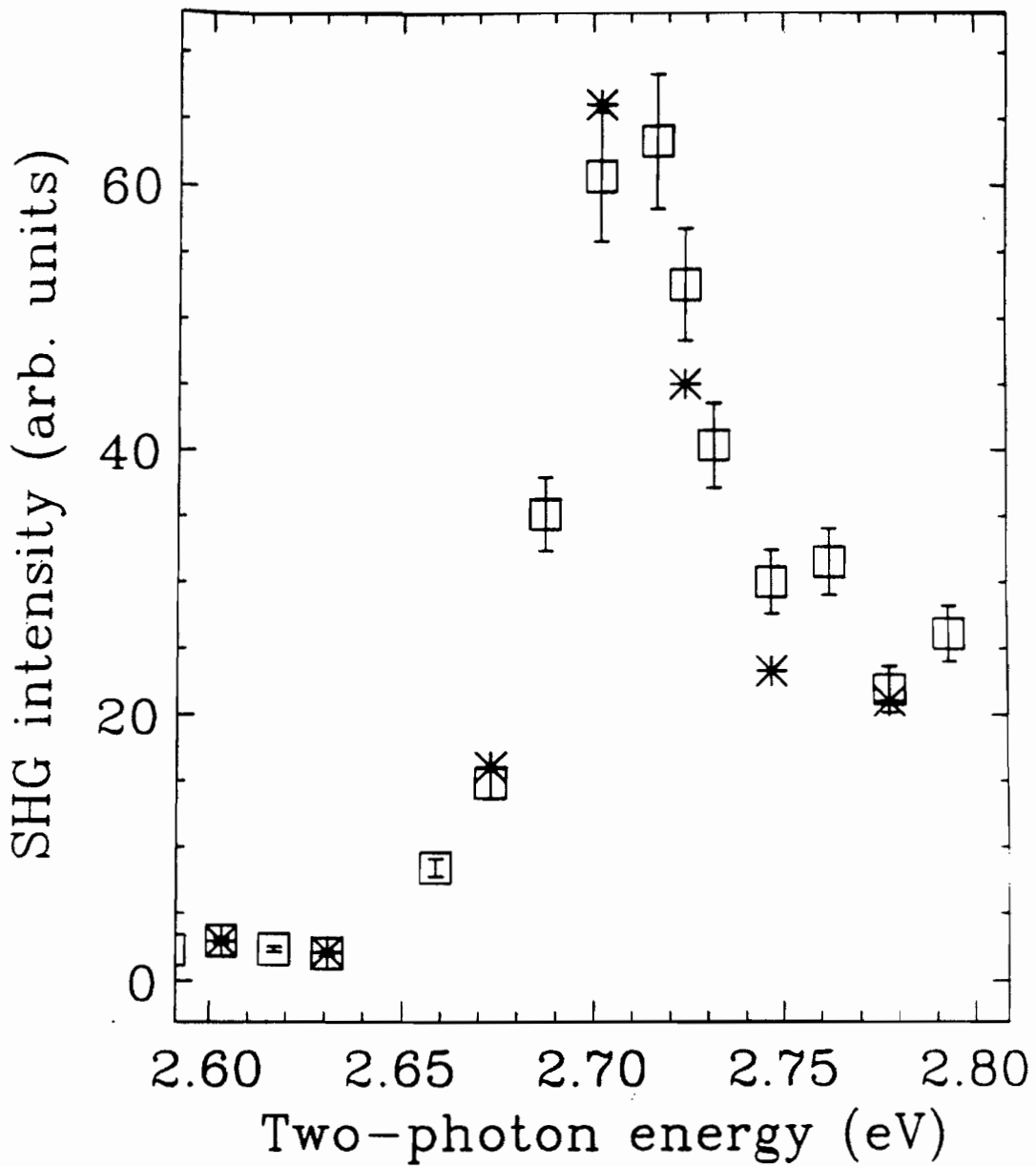


Figure 6.6: The variation of SH intensity as a function of energy of the 1028 Å sample before (□) and after (\*) chemical etching. The chemical etching did not produce any detectable change in the spectrum.

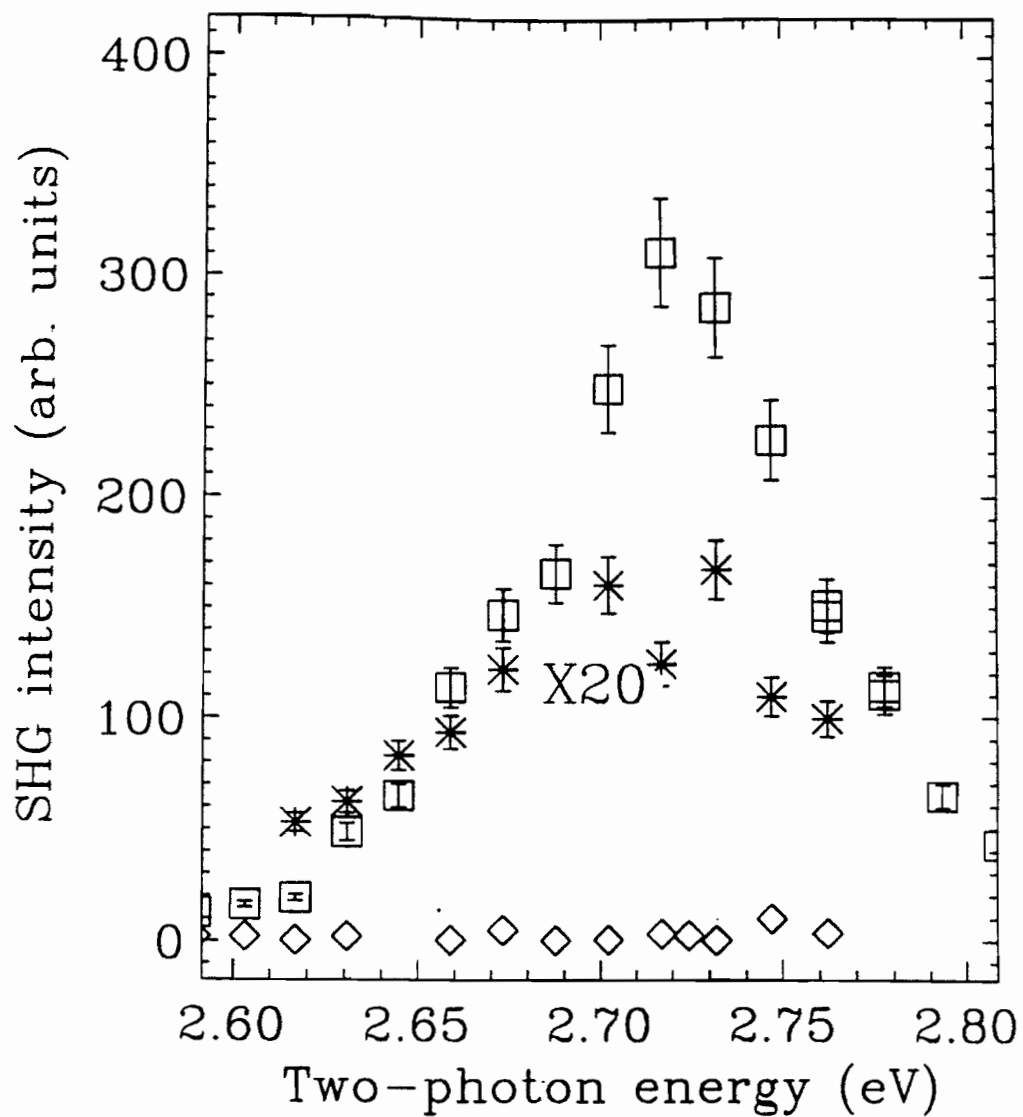


Figure 6.7: The variation of SH intensity as a function of two-photon energy in a S-in/S-out ( $\diamond$ ) and S-in/P-out ( $*$ ) polarization configurations. The interfacial SH spectra ( $\square$ ) is shown for comparison. The S-in/S-out intensity is too small to detect and S-in/P-out intensity is  $\sim 40$  times smaller than the interface signals.

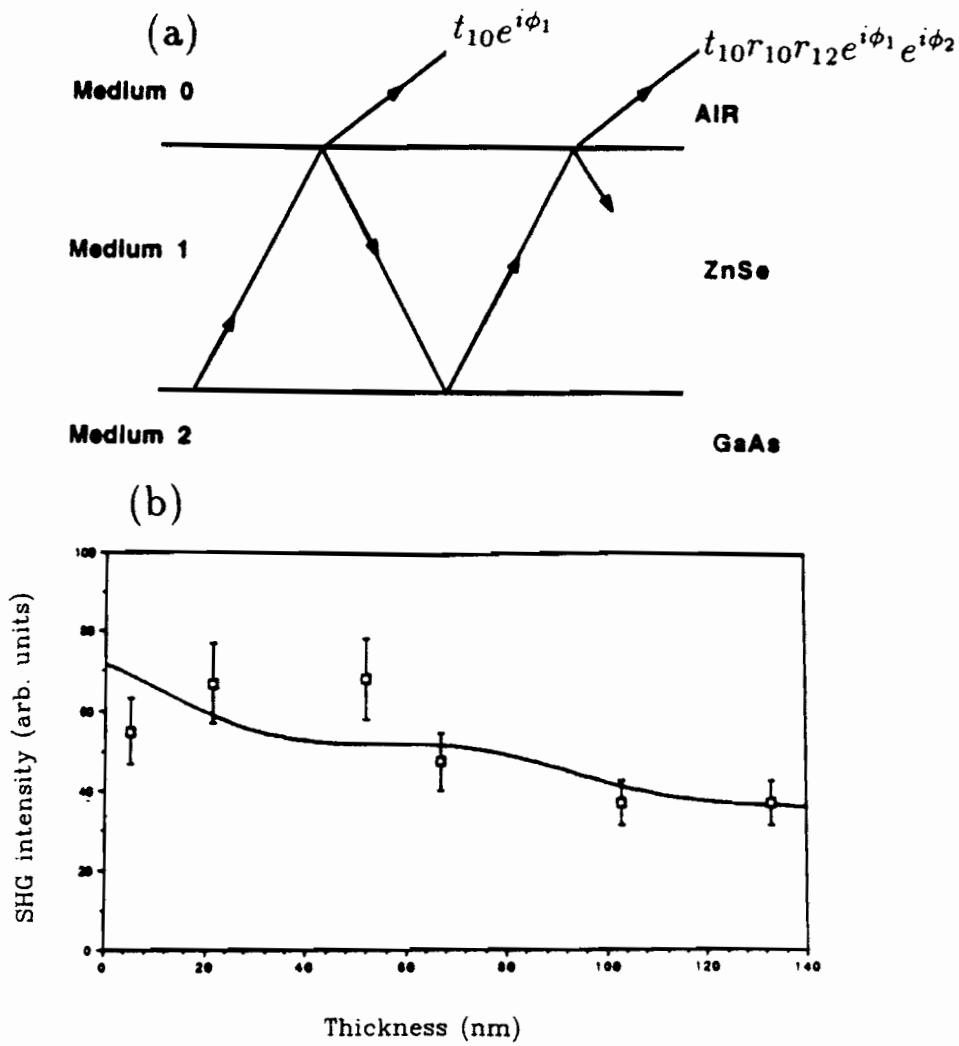


Figure 6.8: (a) A simplified coordinate for the model that described the 2.92 eV resonance. (b) The 2.92 eV interfacial resonance as a function of overlayer thickness. The solid line is the prediction of the model described in the text.

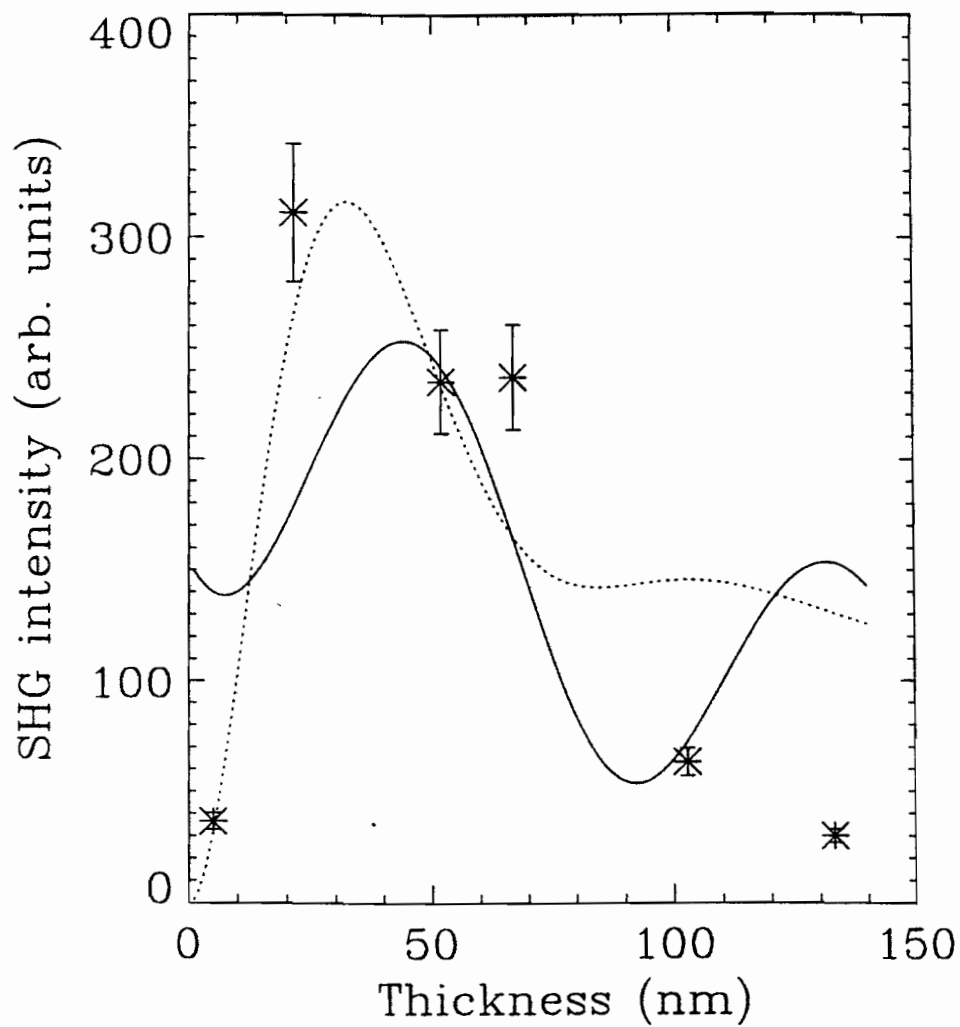


Figure 6.9: Thickness dependence of the 2.72 eV interfacial resonance. The solid line is the prediction of the thickness dependent intensity based on a model similar to the bulk, where the susceptibility was assumed to be uniform through the overlayer. The dotted line is the result of the calculation based on the model which takes  $\chi^{(2)}$  position dependent.

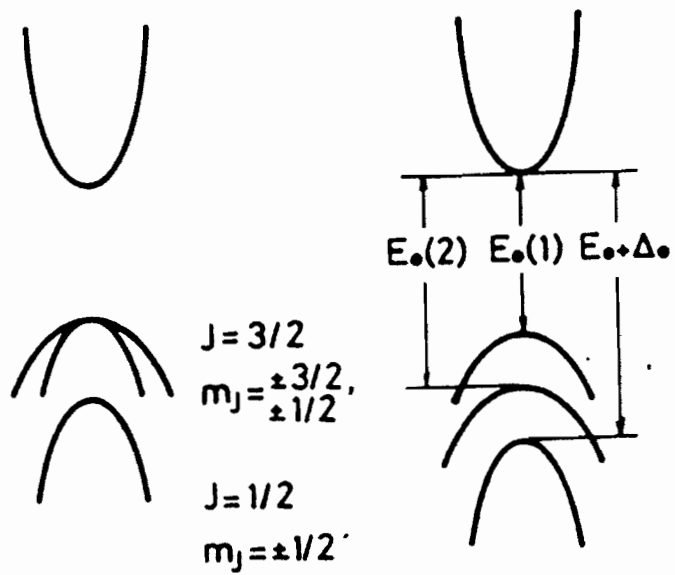


Figure 6.10: The optical transitions and band splitting caused by the deformation potential.

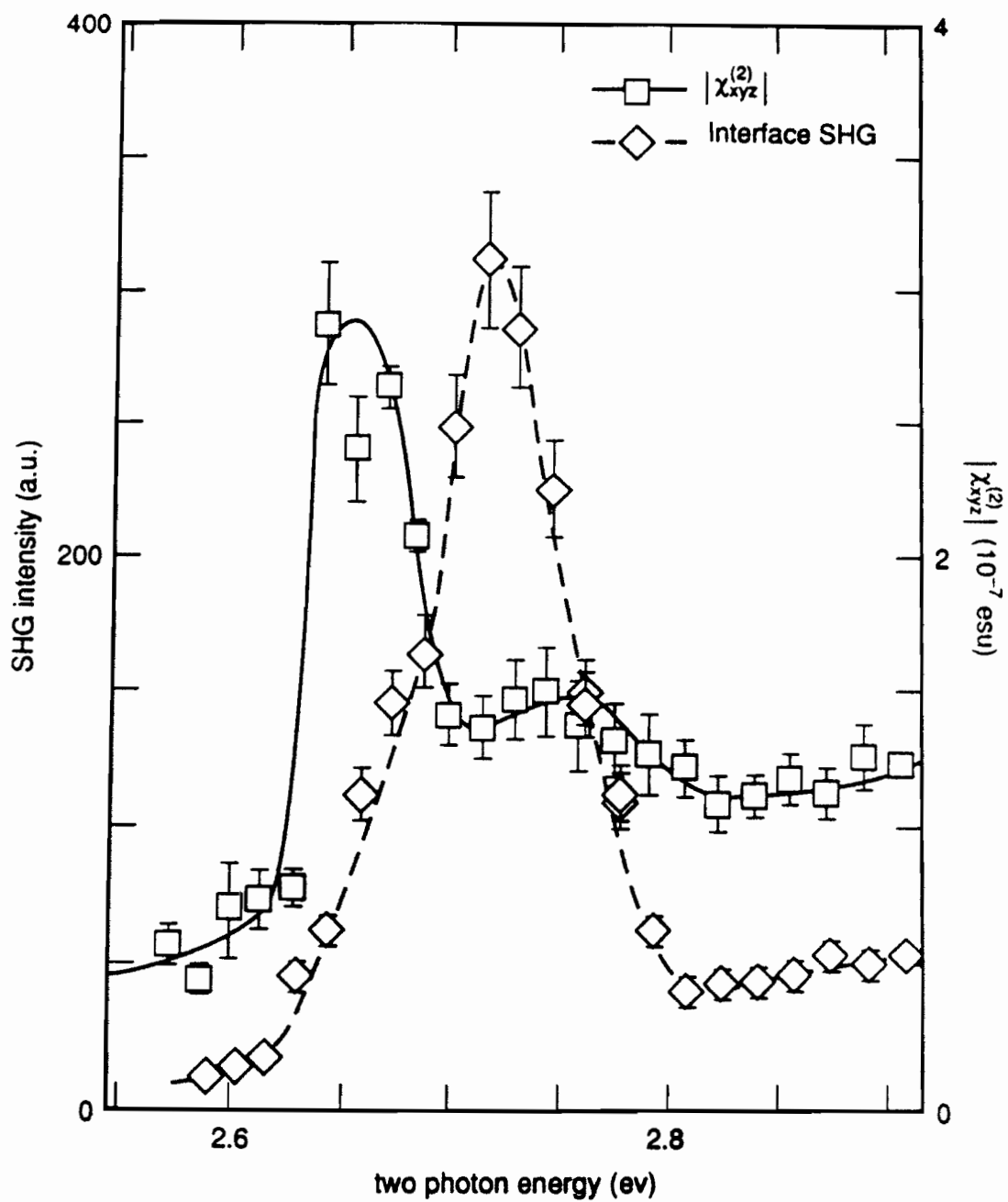


Figure 6.11: The deduced  $\chi_{xyz}^{(2)}$  of the bulk of the ZnSe overlayer ( $\square$ ) is compared with the interface SH spectrum ( $\diamond$ ). The solid lines are only a guide for the eye.

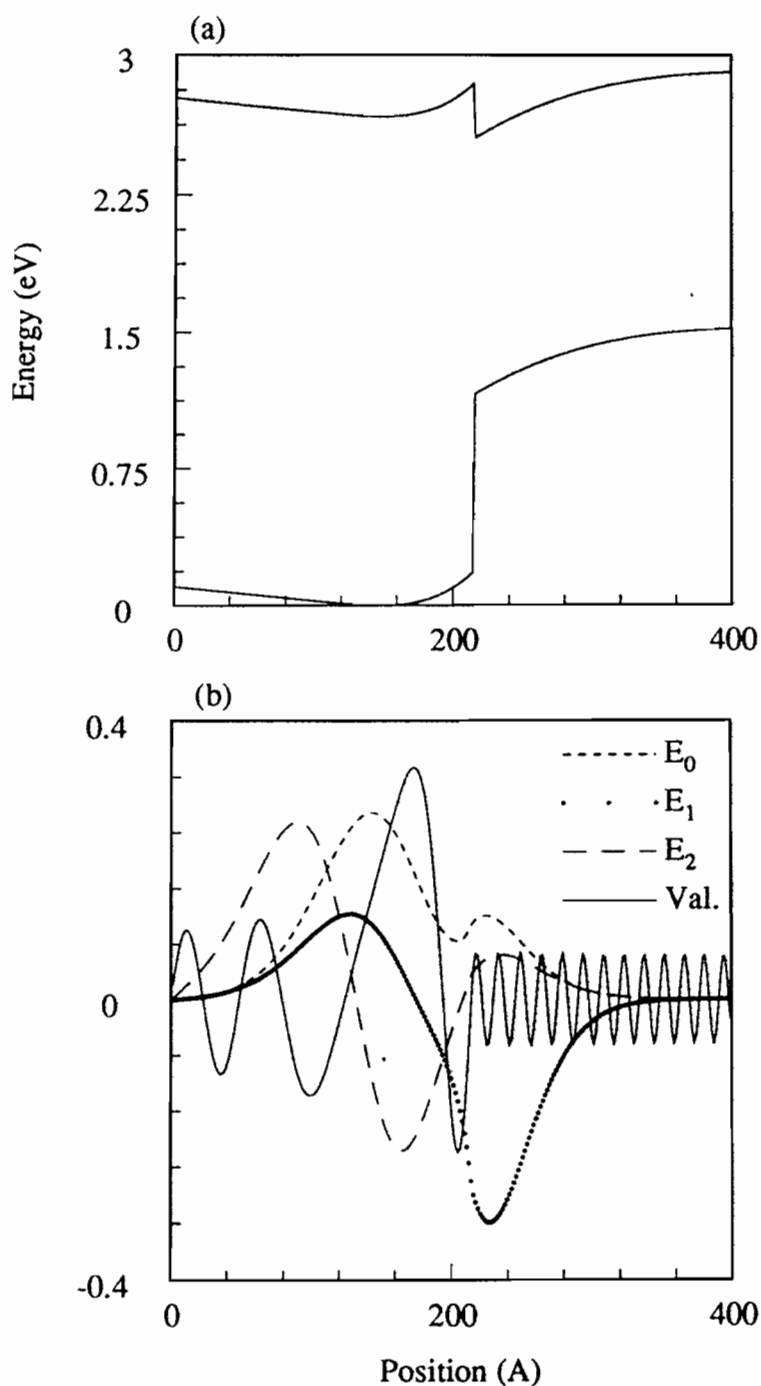


Figure 6.12: (a) Energy-band profile as a function of the depth for ZnSe/GaAs(001) system. This band profile was determined by solving Poisson equation for a Gaussian charge distribution. (b) The wavefunction of first three eigenstates of the quantum well along with the valence band wavefunction. The thickness of the overlayer is 215 Å.

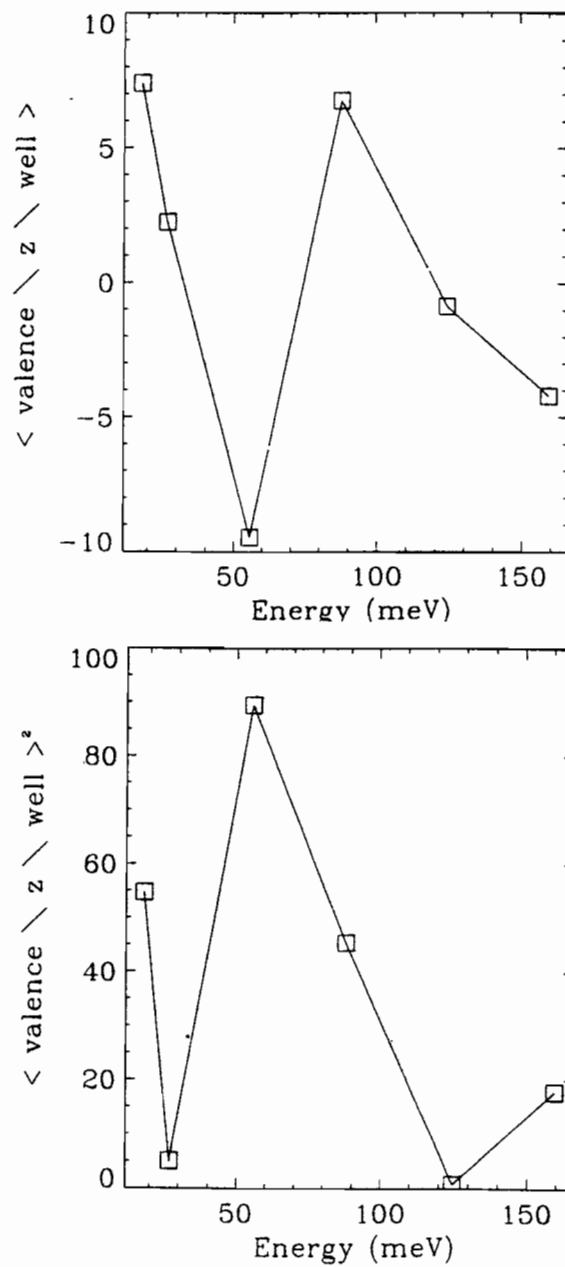


Figure 6.13: In the top figure the matrix element of the dipole moment is calculated as a function of the energy for the interfacial quantum well. It is clear that the third energy level generated the strongest matrix element. In the bottom figure, the square of the dipole moment is plotted.

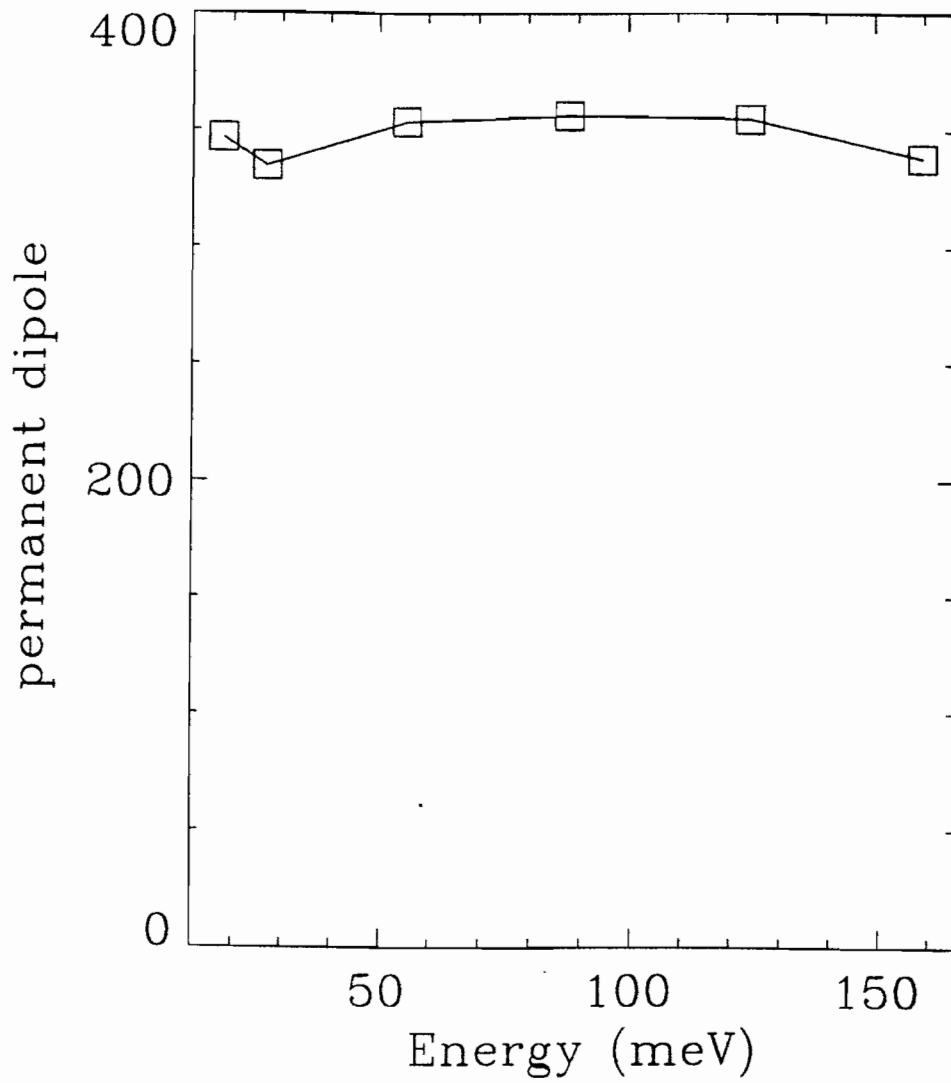


Figure 6.14: Calculated permanent dipole moment as a function of the energy for the interfacial quantum well.

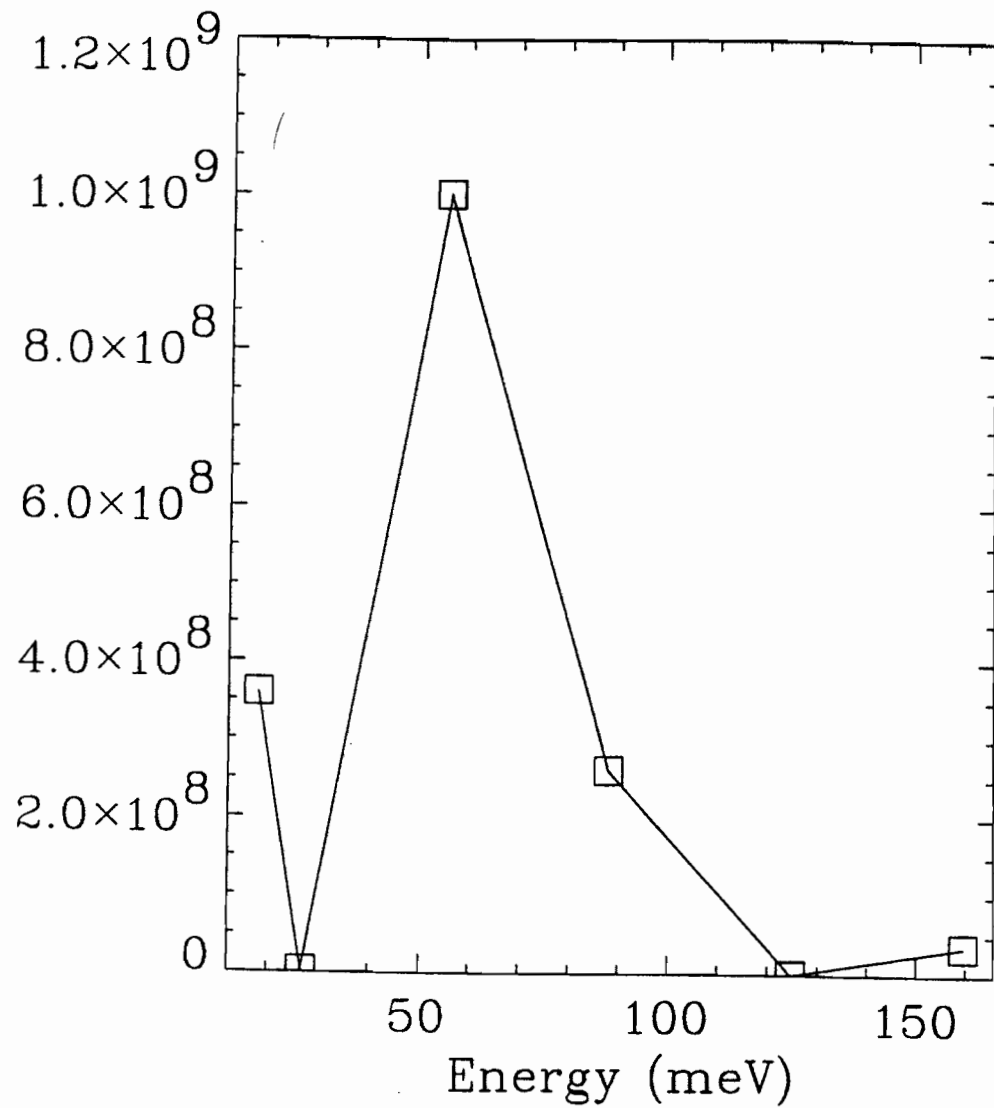


Figure 6.15: Relative strength of the SH signal in two level process as a function of the energy.

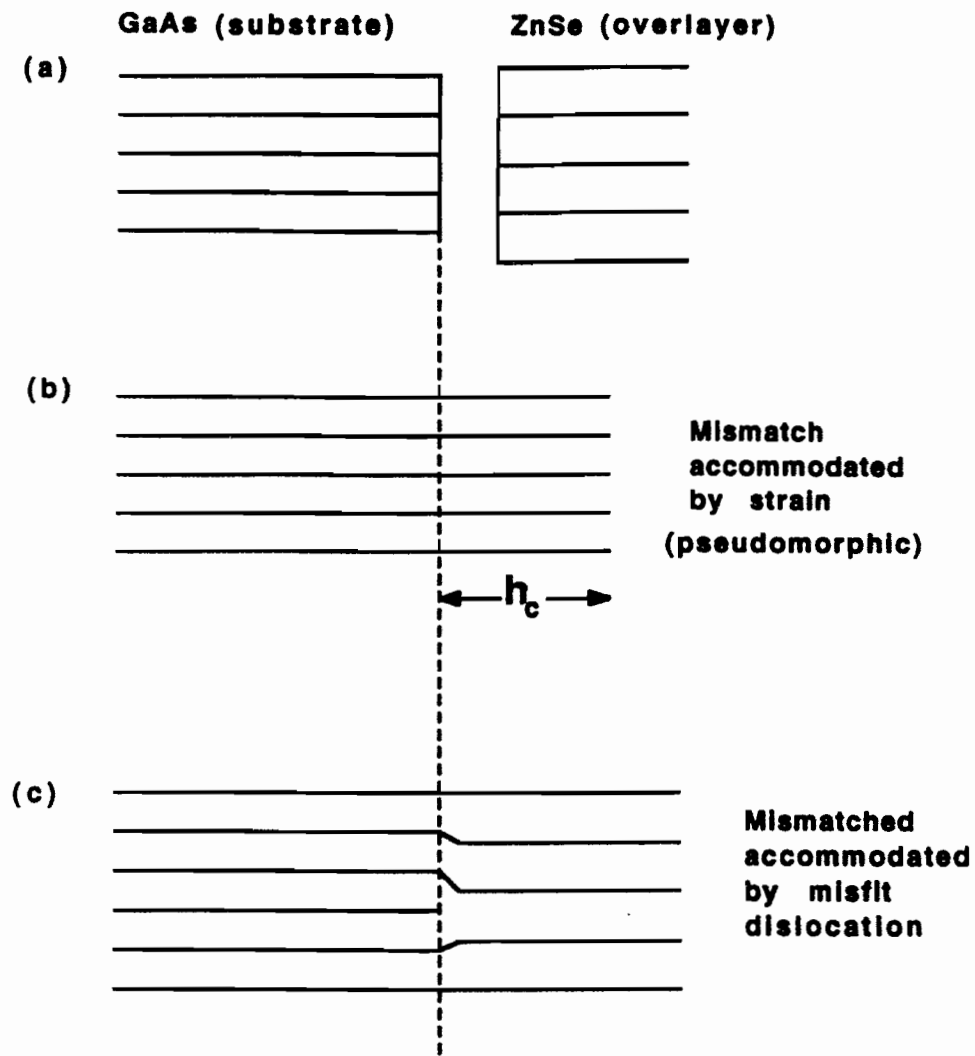


Figure 6.16: A schematic representation of the formation of misfit dislocations.

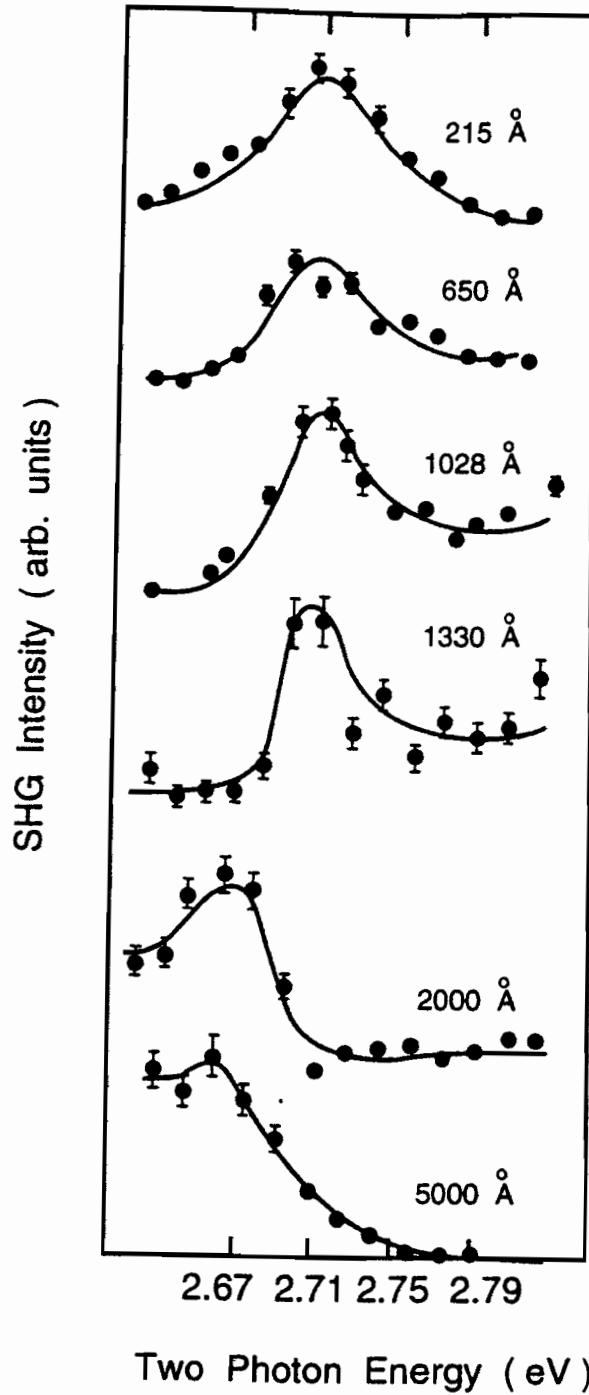


Figure 6.17: Interfacial resonance SHG spectra near 2.72 eV, as a function of overlayer thickness. The critical thickness is between 1330 Å and 2000 Å. Note that the resonance vanishes over this thickness range.

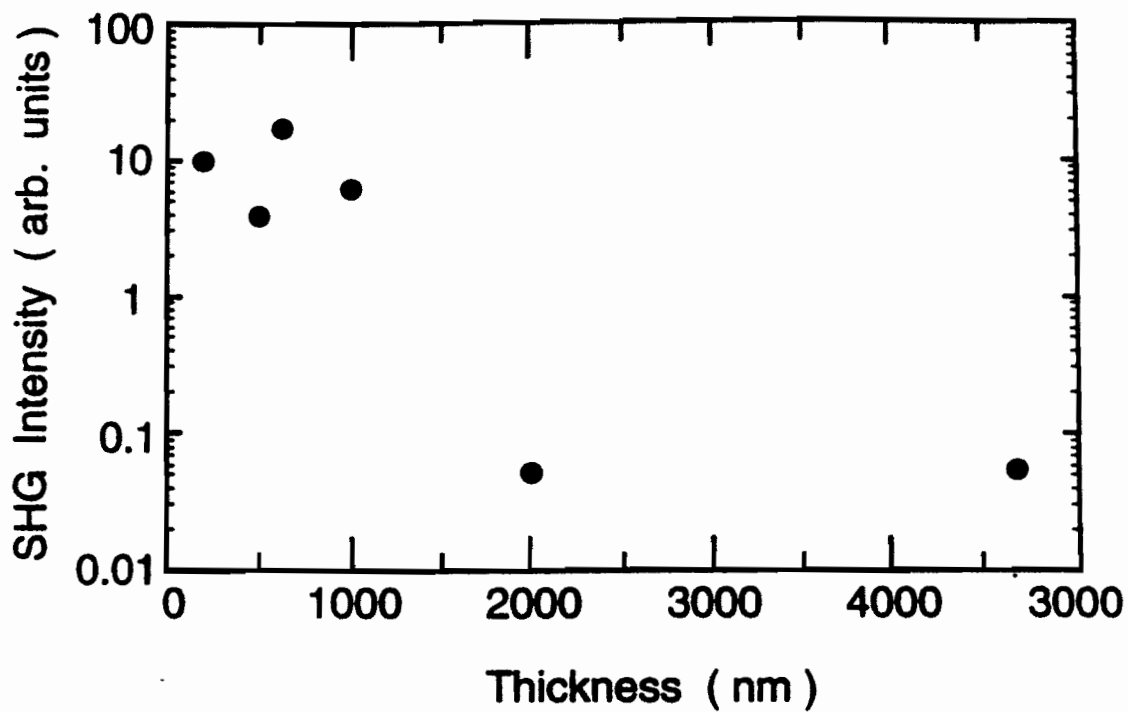


Figure 6.18: Normalized SHG peak intensity at 2.72 eV as a function of overlayer thickness. The data, derived from last figure, exhibit a dramatic drop for overlayer thicker than 1330 Å.

## Chapter 7

# Photomodulation of Second-harmonic Generation

It is well known that band bending often arises at the junction of two dissimilar semiconductors [94]. As we have seen in ZnSe/GaAs heterostructures this band profile can lead to new electronic states. Under these conditions any mechanism that changes the electric field in a heterojunction can alter the interfacial band profile and the wave function of the new electronic states [32]. As a result, the nonlinear optical response of the system that involves the transition to those states will be substantially changed.

Linear photomodulation is a simple way to alter the band bending. A weak beam of light generates electron hole pairs (EHP) which can change the electric field in a material [95, 96]. We have combined second-harmonic generation with

photomodulation as a new method of measurement to study solid/solid interfaces. The photomodulation-second-harmonic generation (PSHG) technique was used to confirm the existence of a quantum well at the ZnSe/GaAs heterointerface and to study interfacial trapping, electronic trap lifetimes, and surface reconstruction of buried GaAs. This chapter will describe the PSHG experiments and its applications.

## 7.1 PSHG Experiment

In the PSHG experiments we have measured the intensity of the 2.72 eV SH resonance as a function of fluence and wavelength of a photoexciting light source. The sample was illuminated at normal incidence by light from either a Tungsten lamp-monochromator or an argon-ion laser, *while the SHG experiment was in progress*. The intensity of the photoexciting beam was monitored simultaneously, and never exceeded 0.5 mW/cm<sup>2</sup>. Typically the sample was illuminated for a period of  $\sim 2$  minutes before it reached steady state. A schematic of the PSHG experiment is shown in Fig. 7.1, and details of the SHG experiments with ZnSe/GaAs(001) are given in Chapter 3.

## 7.2 Is the Interfacial Resonance at 2.72 eV Associated With the Quantum Well? An Independent Test

In this section we will discuss the PSHG experiments which were used to confirm the origin of the SH interfacial resonance at 2.72 eV. First a brief discussion of the PSHG mechanism will be given, and then the experimental results will be presented.

The underlying mechanism of the technique can be described as follows. The photogenerating light beam, with photon energy greater than the band gap of the system, produces EHP. Some of these free carriers move toward the junction and are captured by the interfacial trap centers, thereby altering the interface charge density. The new interface charge will modify the band bending and perturb the states associated with the quantum well. The interfacial trapped holes *decrease* the negative charge of the interface and decrease (increase) the band bending on the ZnSe (GaAs) side of the junction. This delocalizes the quantum well wave function and reduces its relative amplitude within the well. As a result the SHG signal will drop (see Section 7.5). Alternatively, interfacial trapped electrons will increase the SHG signal.

We have displayed the variation of the interface and bulk signals as a function of lamp intensity using a fixed lamp photon energy of 3.0 eV in Fig. 7.2. The bulk and the 2.92 eV interface resonance changed by less than 3%, even at the highest lamp

powers. In contrast, the 2.72 eV interface resonance exhibited a marked decrease in intensity at very low lamp powers. The photomodulation-SHG measurements thus lead us to conclude that the two interface resonances at 2.72 eV and 2.92 eV are intrinsically different. This corroborates our earlier assignment of the 2.92 eV resonance to the  $E_1$  transition of buried GaAs. *The photoexcitation was not observed to significantly affect any bulk signal.*

The weak photoexcitation was observed to cause a reduction in peak SH intensity, but was too small to create a measurable energy shift within our experimental resolution. These observations are consistent with theoretical modeling (see Section 7.5) done by integrating the one-dimensional Schrodinger equation for the quantum well potential. Note also that the results of PSHG cannot be explained by the optical pumping of electrons into the quantum well resonance state. Our PSHG data as a function of lamp photon energy, described in Section 7.3, exhibits that the maximum rate of change of the SHG intensity is at the ZnSe optical band gap energy of 2.67 eV and not at 2.72 eV. This fact, along with the observed *increase* of SHG intensity as a result of 2.4 eV carrier exciting photons (see Section 7.6), does not support the optical pumping mechanism.

### 7.3 Identification of the Type of Trap-centers

PSHG experiments enabled us to identify the type of interfacial trap-centers in ZnSe/GaAs(001) heterostructures. The variation of the resonant SH intensity as

a function of lamp photon energy is shown in Fig. 7.3. In this experiment the lamp intensity transmitted into the sample was kept constant at  $10 \mu\text{W}/\text{cm}^2$ . Although the efficiency of carrier generation in GaAs is much greater than ZnSe [103], we see no effect as a result of carriers in GaAs at this intensity level. Since electrons are the only photoexcited carriers in GaAs that move toward the interface, we can conclude that the interface traps are mainly hole traps. This is in agreement with the result of the negative interface charge in 2x4 samples [97]. Because the proposed interface intermediate phase [98, 99],  $\text{Ga}_2\text{Se}_3$ , is positively charged, our result suggested that this phase does not exist.

## 7.4 Interfacial Trap Lifetime and Density: A Theoretical Model

Here we are interested in calculating the change in the dominant second-order susceptibility,  $\chi_{zzz}^{(2)}$ , and the SH intensity as a function of trapped-charge density and time. We have shown that the interfacial traps are dominantly hole traps. In this section we only consider the effect of this type of trap with carrier generating photon energy greater than the band gap of ZnSe (2.67 eV). The argument for electron traps is described in Appendix. H

Ultimately we are interested in calculating the carrier induced change of the dominant second-order susceptibility tensor element,  $\chi_{zzz}^{(2)}$ . This will enable us to

deduce the variation in SH intensity as a function of trapped-charge density and time. In the following discussion we will assume the trap-centers are localized at the junction and evaluate all the parameters at the interface. This assumption is reasonable since the interfacial imperfections are the main cause for the generation of trap-centers. We also use the steady state value of the free electron ( $n$ ) and the free hole densities ( $p$ ) for this calculation. Since our measured trap lifetime is many orders of magnitude greater than the lifetime of the free carriers, this assumption is also reasonable. Within this model the change in the interface charge due to trapping is proportional to the density of the interfacial trapped-holes,  $p_t$ . A localized rate equation at the interface relates  $p_t$  to the other physical parameters of the system [100, 101]:

$$\frac{\partial p_t}{\partial t} = k_{1h}p(N_h - p_t) - k_{2h}np_t - r_h p_t. \quad (7.1)$$

Here  $N_h$  is the number density of the interfacial hole trap centers, and  $k_{1h}$  ( $k_{2h}$ ) is the rate constant at which an unoccupied (occupied) trap center will trap a hole (recombine with an electron) at the interface.  $r_h$  is the rate constant at which a trapped-hole is injected into the valence band by thermal excitation. At the low injection limit we assume that the densities of photogenerated carriers are linearly proportional to the intensity of the photogenerating lamp light,  $I_l$ . This *linear approximation* was experimentally tested and will be explained later in this chapter. Within the linear approximation we write

$$p = \alpha_{1h}I_l + p_0 \quad (7.2)$$

and

$$n = \alpha_{2h} I_l + n_0. \quad (7.3)$$

Here  $\alpha_{1h}$  ( $\alpha_{2h}$ ) represents the deviation of interfacial free hole (electron) density from its thermal equilibrium value per unit of lamp light intensity. Both  $\alpha_{1h}$  and  $\alpha_{2h}$  depend on the generation of free carriers as well as their transport to the interface. Thus, these parameters are a function of the quantum efficiency and mobility of the system.  $p_0$  and  $n_0$  denote the equilibrium value of free hole and electron density in the absence of the photoexciting light. Since the thermal excitation in a wide band gap semiconductor is very small we can safely ignore the density of thermally excited holes,  $p_o$ , in comparison to  $\alpha_1 I_l$  for photon energies greater than 2.67 eV.

The rate equation, Eq. (7.1), leads to the following time dependent trapped-hole density:

$$P_t(t) = A_h e^{-t/\tau_h} + \frac{k_{1h}\alpha_{1h}N_h I_l}{(k_{1h}\alpha_{1h} + k_{2h}\alpha_{2h})I_l + \tau_{oh}^{-1}}, \quad (7.4)$$

with

$$\tau_{oh} = \frac{1}{k_{2h}n_{oh} + r_h} \quad (7.5)$$

and

$$\tau_h = \frac{1}{(k_{1h}\alpha_{1h} + k_{2h}\alpha_{2h})I_l + \tau_{oh}^{-1}}. \quad (7.6)$$

$A_h$  is a constant and is determined by boundary conditions. The parameter with subscripts "h" is a hole trap parameter.

We approximate the time dependent Hamiltonian resulting from this interfacial

trapped-charge by

$$H_h^{(1)} = \frac{2\pi}{\epsilon} q_h p_t z \quad (7.7)$$

where  $\hat{z}$  is in the direction normal to the interface, and  $q_h$  is the unit charge of a hole. The effect of this Hamiltonian on the electronic structure of the system and  $\chi_{zzz}^{(2)}$  can be described by perturbation theory. Since the measured time scale for the change in  $\chi_{zzz}^{(2)}$  was much slower than the electronic lifetime of the quantum well states, we can use the time independent perturbation to explain the physical phenomena in our calculations.

The wavefunction of the interfacial quantum well is sensitive to the detailed structure of the well and thus to the band bending at the junction. However, the sensitivity of the wavefunction to photomodulation in the valence band (ground state) and the higher energy levels of the conduction band of ZnSe are much weaker than the interfacial quantum well. This was confirmed experimentally where we did not observe any change in the bulk SHG signal under photomodulation. The variation of  $\chi_{zzz}^{(2)}$  may thus be reasonably modeled by considering only the change of the resonance state of the interfacial quantum well wavefunction,  $|w\rangle$ .

The electrons in the conduction band are free in the plane parallel to the interface, therefore the Schrodinger equation for this system reduces to a one-dimensional problem. The eigenstates of this problem decay rapidly into the vacuum (i.e.  $z \rightarrow \infty$ ) and are non-degenerate [102]. Thus we use non-degenerate perturbation theory with

the perturbation Hamiltonian  $H_h^{(1)}$ . That is

$$|w\rangle = |w_o\rangle + \sum_{w'} \frac{\langle w'|H_h^{(1)}|w_o\rangle}{E_{w'w_o}} |w'\rangle. \quad (7.8)$$

The  $|w'\rangle$  are other states of the quantum well and the subscript "o" indicates the value of the parameter in the steady state in the absence of the photogenerating light. The denominator  $E_{w'w_o}$  denotes the difference between the energy eigenvalue  $E_{w'}$  and  $E_{w_o}$ . The perturbation leads to the first order variation of the second-order susceptibility  $\chi_{zzz}^{(2)}$

$$\frac{\chi_{zzz}}{\chi_{zzz,o}} = 1 + \sum_{w'} \frac{2\pi p_t}{\epsilon E_{ww'}} \left( \frac{\langle v|z|w'\rangle \langle w'|z|w\rangle}{\langle v|z|w\rangle} + \frac{\langle w|z|w'\rangle \langle w'|z|e\rangle}{\langle w|z|e\rangle} \right) \equiv 1 + M_h p_t \quad (7.9)$$

with

$$M_h \equiv \sum_{w'} \frac{2\pi}{\epsilon E_{ww'}} \left( \frac{\langle v|z|w'\rangle \langle w'|z|w\rangle}{\langle v|z|w\rangle} + \frac{\langle w|z|w'\rangle \langle w'|z|e\rangle}{\langle w|z|e\rangle} \right). \quad (7.10)$$

The states  $|v\rangle$  and  $|e\rangle$  represent, respectively, the valence band and a higher energy (above ZnSe conduction band) excited state. Eq. (7.8) and (7.9) determine the fractional SHG intensity variation, i.e.

$$\frac{I(2\omega)}{I_o(2\omega)} = (1 + C_{1h} + C_{2h} e^{-t/\tau_h})^2 \quad (7.11)$$

Here,

$$C_{1h} = \frac{M_h k_{1h} \alpha_{1h} N_h I_l}{(k_{1h} \alpha_{1h} + k_{2h} \alpha_{2h}) I_l + \tau_{0h}^{-1}} \quad (7.12)$$

and

$$C_{2h} = M_h A_h \quad (7.13)$$

where  $I^{(2\omega)}$  is the SH intensity. The wavefunction for the one-dimensional problem under investigation is chosen to be real in coordinate basis [102], therefore the parameters  $C_{1h}$  and  $C_{2h}$  are real. Note that  $C_{1h}/M_h$  is the steady state solution of the trapped-hole density (Eq. 7.1). Eq. (7.11) clearly shows that the trapped-charge density increases with the lamp intensity and approaches its asymptotic value,  $(k_{1h}\alpha_{1h}N_h)/(k_{1h}\alpha_{1h} + k_{2h}\alpha_{2h})$ . At this point the charge density,  $p_t$ , will not be affected by higher lamp intensity and the band flattening will have reached its final condition.

## 7.5 Variation of Quantum Levels With Photomodulation: A Theoretical Model

We have already described the band profile and electronic states of the quantum well in Chapter 6. This section discusses the change in the band profile and the electronic states of the quantum well with photomodulation. It was found that the amplitude of the wavefunction of the valence band and the quantum well are reduced in the depletion region and in the quantum well. The description of the calculation follows.

A photomodulating beam with photon energy of  $> 2.67$  eV introduced a positive interfacial charge into the system. We have re-solved Poisson's equation with the new charge distribution and deduced the new band profile in a manner similar to that discussed in Chapter 6. Once we had the new band profile, the electronic states were

identified by solving the one-dimensional Schrodinger equation. The change in the band profile and wavefunction as influenced by photoexcitation is shown in Figs. 7.4, 7.5, and 7.6. One can see that the amplitude of the wavefunction of the valence band decreased in the well and in the depletion region. A similar behavior is observed for the wavefunction of the quantum well. The reduction in amplitude also produced a reduction in oscillator strength between the valence band and the quantum well. This is in agreement with our SHG experimental observation as discussed in Section 7.2.

It can also be seen that, under photomodulation, the energy levels of the quantum well shift to a higher value with respect to the bottom of the well. However, in our experiment we did not observe any energy shift in the SH spectra under photomodulation within our experimental resolution of 6 meV at 915 nm. This observation is understood in the following context. Our SHG measurement is sensitive to the energy difference between the valence band and the quantum well state and not to the energy difference between the bottom of the well and the quantum level. Since the band profile of ZnSe also shifts upward under the perturbation, the change in the energy interval between the valence band and the quantum well state is small. Our calculation indicates that the quantum well state could shift by 52 meV with respect to the bottom of the well. This large shift, however, introduces a small shift of 1.3 meV in the SHG resonance.

## 7.6 Interfacial Electronic Trap Lifetime

In this section we will describe the time dependent PSHG experiments for studying the interfacial trap lifetime of the ZnSe/GaAs(001) heterojunction. The time dependent PSHG experiments were designed to measure trapping and detrapping lifetimes ( $\tau$  and  $\tau_o$ ) as a function of lamp intensity. The steady state PSHG experiments were aimed at studying the dependence of photomodulating intensity on band flattening. The details of these experiments are as follows. Time dependent measurements were performed using two different initial conditions, an open and a closed photogenerating beam shutter. To measure the intensity dependence of  $\tau$  the sample was first illuminated with light at a fixed intensity, and the SH signal was measured as a function of time. This procedure was then carried out for different lamp intensities and repeated 100 times at each fluence.

The measurements of  $\tau_o$  were carried out by illuminating the sample with the lamp for at least 2 minutes. Then, the photogenerating beam shutter was closed and the SHG intensity was measured as a function of time. This procedure was also repeated 100 times.

We have also measured the steady state SH intensity as a function of lamp fluence for a photon energy of 2.4 and 3.0 eV. In these measurements the sample was illuminated for a period of  $\sim 2$  minutes. Then with the lamp beam kept on the sample the data acquisition began.

The ZnSe/GaAs(001) heterostructure sample used in these experiments consists of a 215 Å epitaxial layer of undoped ZnSe(001) grown on a .5 μm undoped GaAs(001) film terminated with 2x4 surface reconstruction. It should be noted that a Nd:YAG pumped dye laser with a repetition rate of 10 Hz was used as the light source for SH measurements, and the boxcar averager was set to take an average over 10 shots. This brings the time resolution of the experiments to ~1 second.

The experimental results for  $\tau_h$  measurements with lamp intensity of  $5.3\mu\text{W}/\text{cm}^2$  and photon energy of 3.0 eV are shown in Fig. 7.7. We repeated the same measurements for lamp intensities of  $0.4\mu\text{W}/\text{cm}^2$  to  $5.3\mu\text{W}/\text{cm}^2$ . We were not able to perform the time dependent measurements at higher lamp intensities, because the higher intensity resulted in a lifetime that was shorter than the resolution of our boxcar averager. The solid line in Fig. 7.7 is the best fit to Eq. (7.11), and it determined the best value for the free parameter  $C_{1h}$ ,  $C_{2h}$ , [Eqs. (7.12) and (7.13)] and lifetime  $\tau_h$  [Eq. (7.6)]. The fitting was performed for all measured lamp intensities. In this way we were able to study the intensity dependence of  $\tau_h$  (see Fig. 7.8). Our data, at least for the fluence below  $5.3\mu\text{W}/\text{cm}^2$ , showed that the inverse of  $\tau$ , and thus the free carrier densities, are linearly dependent on the intensity of the photoexcitation beam.

We have shown the results of  $\tau_{oh}$  and  $\tau_{oe}$  measurements with photon energy of 2.4 and 3.0 eV in Fig. 7.9. The data exhibit a slow recovery time for the SH intensity. The solid lines in Fig. 7.9 are the best fit to the theory. Our fitting routine determined

the best value for the recombination of the interfacial trap lifetime,  $\tau_0$ . This value was  $35.4 \pm 0.5$  sec and  $35.0 \pm 0.5$  sec for a carrier generating photon energy of 3.0 and 2.4 eV, respectively. These long lifetimes are characteristic of metastable electronic states typically generated by defects.

We now turn to the dependence of the steady state SH intensity on the photoexcitation fluence. The steady state SHG intensity as a function of lamp intensity for a lamp photon energy of 3.0 eV is shown in Fig. 7.10. A word of caution is necessary in analyzing the data. Our theoretical results in Eq. (7.12) are based on a linear approximation and our lifetime measurements were able to show the linearity only up to  $5.3 \mu\text{W}/\text{cm}^2$ . Thus, in principle, we can only fit our data for intensity below  $5.3 \mu\text{W}/\text{cm}^2$ . The solid line in Fig. 7.10 is the best fit, using only the low intensity data. The constants  $k_{1h}\alpha_{1h}N_h$  and  $(k_{1h}\alpha_{1h} + k_{2h}\alpha_{2h})$  are the only two free parameters in our fitting routine, and the value of  $kn_0 + r = \tau_0^{-1}$  was deduced from the time dependent measurements.

We have also carried out the fitting routine for all available data. This is shown by a dotted line in Fig. 7.10. The comparison of these two fits could determine the validity of a linear approximation for higher intensities. One can see that these two fits are different for high lamp intensities. This difference could be an indication of poor agreement of a linear approximation with our data for high lamp intensity. We should note that the  $(k_{1h}\alpha_{1h} + k_{2h}\alpha_{2h})$  parameter in the steady state solution is the slope of the line in Fig. 7.8. The deduced value from these two separate fits are

within  $\sim 2\%$  of each other.

## 7.7 Influence of Buried GaAs Surface Reconstruction on Interfacial Defect Density

We were able to utilize the PSHG technique to study the 2x4 and 3x1 buried GaAs surface reconstructed samples. These measurements demonstrate the sensitivity of second-order nonlinear optics to interfacial defect and atomic structures and provide a unique technique to determine the relative interfacial defect density as a function of substrate surface reconstruction.

The 2x4 and 3x1 GaAs(001) surface reconstructions arise when different mixtures of As and Ga are used to terminate the free surface. Our heterostructure samples consist of an epitaxial layer of undoped ZnSe(001) grown on a 0.5  $\mu\text{m}$  undoped GaAs(001) film terminated with 2x4 or 3x1 surface reconstructions. The 3x1 GaAs(001) surface reconstructed film is accepted to have an approximately equal number of Ga and As atoms, and the 2x4 surface reconstructed layer was prepared to have higher concentration (75 %) of As [27]. The different GaAs(001) surface reconstructions were observed by reflection high energy electron diffraction (RHEED) during growth. When the desired reconstruction pattern was observed, samples were cooled and epitaxial growth of ZnSe was initiated [27]. Both ZnSe and GaAs films were grown by molecular beam epitaxy (MBE) on a  $n^+$  silicon doped GaAs substrate

in a dual chamber MBE system [65]. The thickness of the ZnSe overlayer in both samples was 215 Å.

In considering the effect of substrate surface reconstruction on the SHG signal, there are two important observations. The first is the variation of the SH resonance intensity as a function of lamp intensity derived for both reconstructed samples in separate PSHG experiments (Fig. 7.11). With the blue (3 eV) photomodulating light source, the 3x1 reconstructed sample required more photogenerated carriers than the 2x4 reconstructed sample to achieve the same fractional SHG signal reduction. The results of the second observation are shown in Fig. 7.12. Here the SHG spectra of two samples with the same overlayer thickness, but different surface reconstructions of substrate are compared. One can see that the sample with 3x1 reconstruction exhibits a much stronger peak than the 2x4 sample.

These results can be understood in the context of existing theories of the ZnSe/GaAs(001) interface. The 2x4 GaAs(001) reconstructed sample is an As rich terminated surface which produces a relatively large number of charged interfacial bonds [27], whereas the 3x1 reconstruction should minimize both the interface charge and charge trap number density. The models used to make these predictions are based on a valence electron counting method for polar interfaces [97].

A detailed analysis of the data in Fig. 7.10, along with additional trap lifetime experiments explained in Section 7.6, have enabled us to make a stronger and more precise statement about the relative hole trap densities. We have fit the data to

steady state [Eq. (7.11) with  $\tau$  approaching infinity] for both samples. The result of the fit is shown in Fig. 7.10. The parameters  $M_h k_{1h} \alpha_{1h} N_h$  and  $(k_{1h} \alpha_{1h} + k_{2h} \alpha_{2h})$  are the only two free parameters in our fitting routine. We have used the value of  $\tau_{0h}^{-1}$  from our time dependent measurement described in Section 7.6. We have found that

$$(k_{1h} \alpha_{1h} N_h)_{2 \times 4 \text{ sample}} / (k_{1h} \alpha_{1h} N_h)_{3 \times 1 \text{ sample}} \simeq 10.$$

The parameter  $\alpha_{1h}$  represents the deviation of interfacial free hole density from its thermal equilibrium value per unit of lamp light intensity. Intuitively we expect  $\alpha$  to be bigger in systems with a lower number of trap and scattering centers. Our time-dependent measurements (see Section 7.6) indicate that  $k$  is about the same in both samples. Thus, we can argue that the trap density in the 3x1 sample is *at least* 10 times less than in the 2x4 sample. A similar analysis of the PSHG data, with 2.4 eV carrier generating photon (see Fig. 7.13), indicates that the electron trap density in the 3x1 sample is *at least* 3 times less than the 2x4 sample. The lower trap densities should also be expected to enhance the size of the 3x1 SH resonance as compared to the 2x4 resonance (Fig. 7.12), in analogy with photoconductivity measurements on these systems [27] where the 3x1 reconstruction exhibits a factor of  $\sim 50$  increase in photocurrent over the 2x4 system.

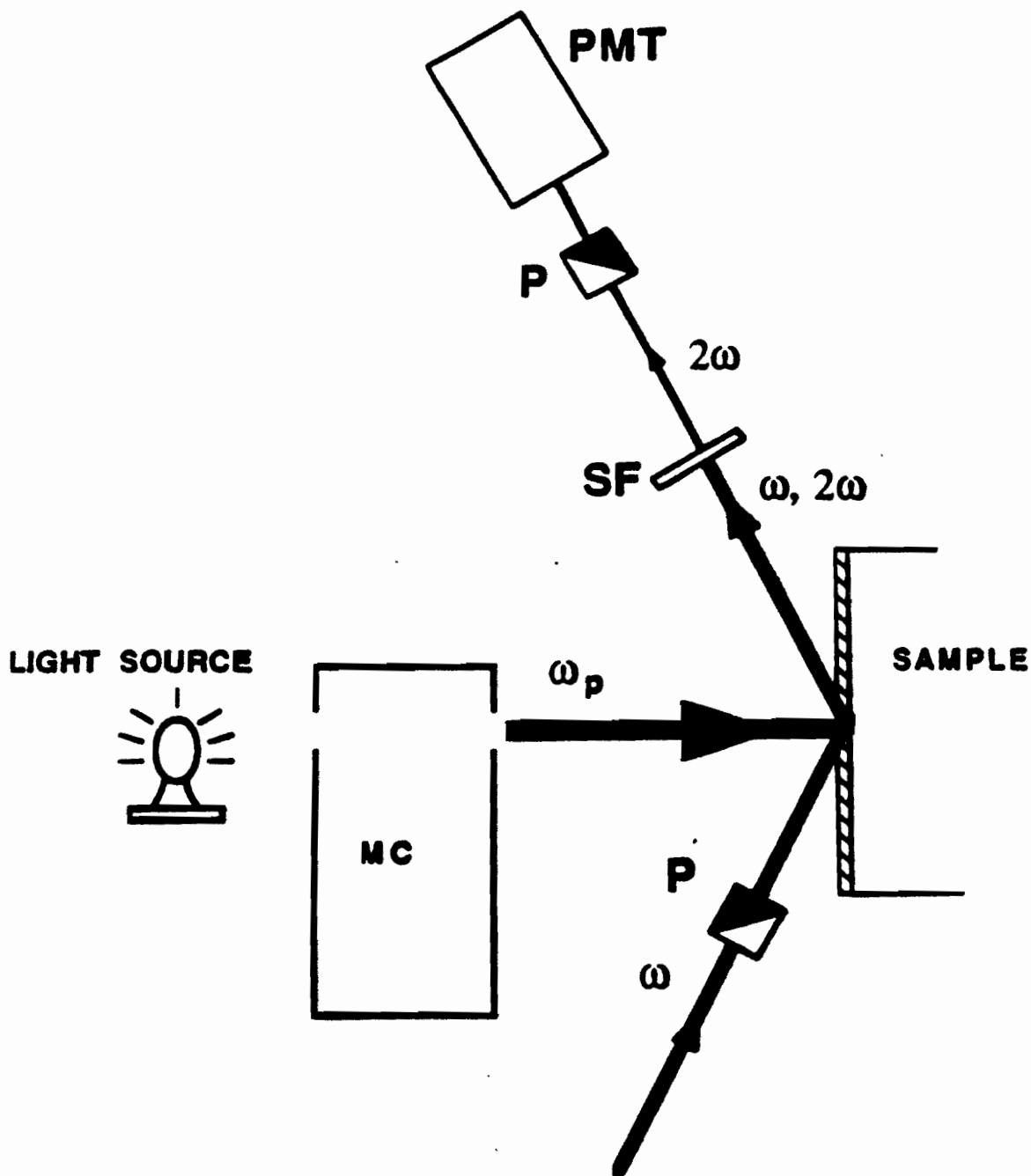


Figure 7.1: Schematic of PSHG experiment: Sample was illuminated at normal incidence by light from a Tungsten-lamp-monochromator, while the SHG experiment was in progress.

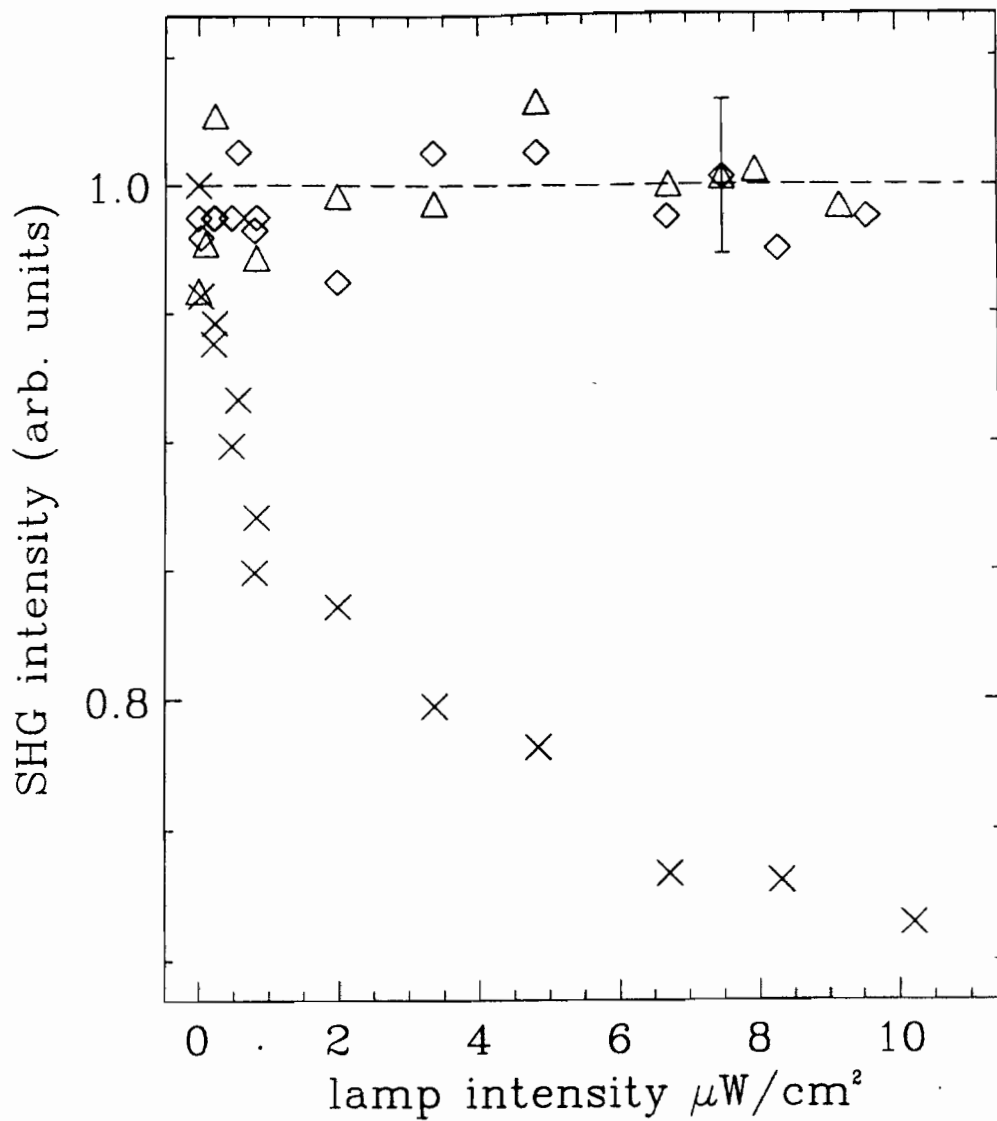


Figure 7.2: Normalized variation of the SHG intensity for the interface at 2.72 eV ( $\times$ ) and 2.92 eV ( $\Delta$ ), and the bulk at 2.67 eV ( $\diamond$ ) as a function of the lamp intensity transmitted into the sample at a fixed lamp photon energy of 3.0 eV.

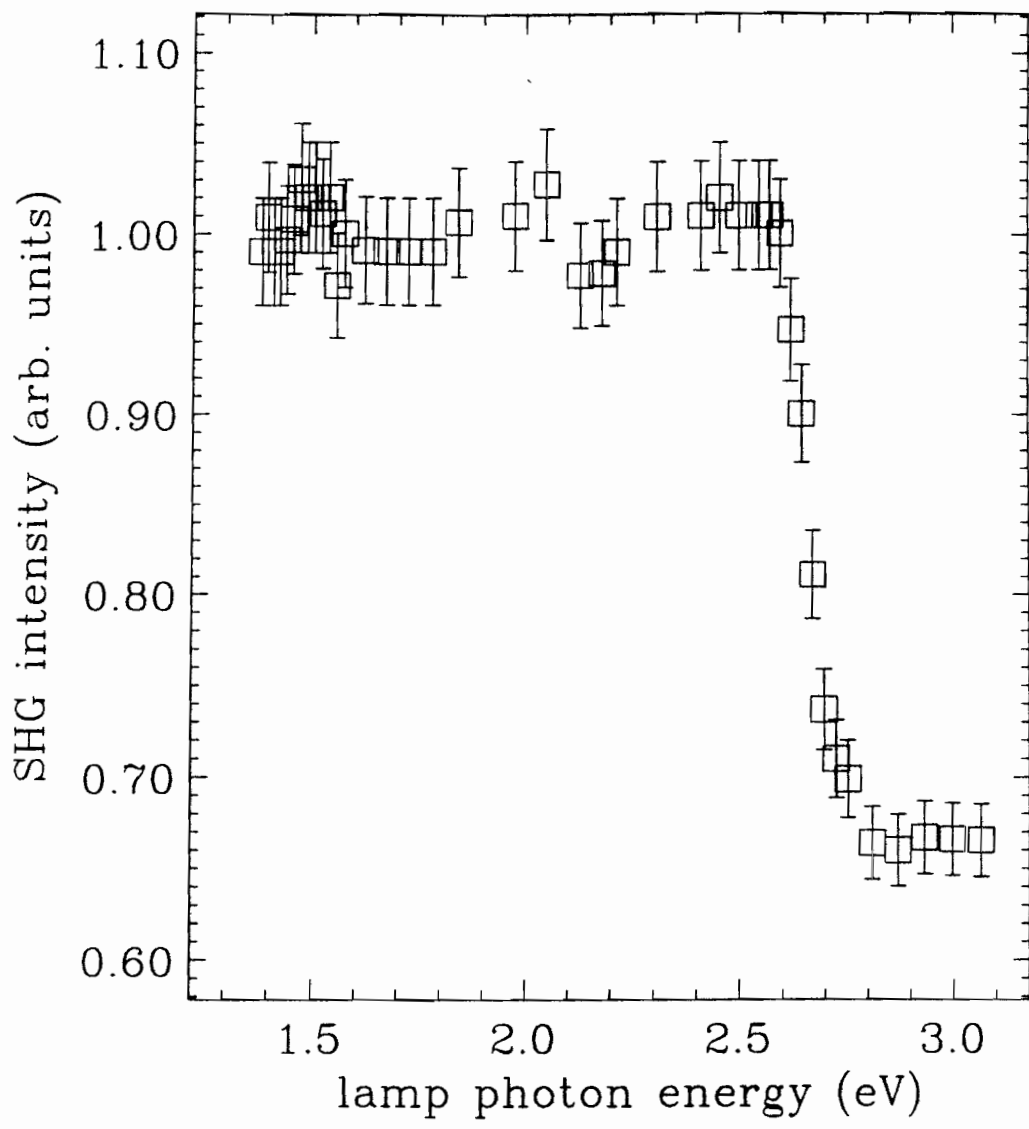


Figure 7.3: Normalized variation of the resonance interface SHG intensity at 2.72 eV as a function of lamp photon energy. Here the transmitted lamp intensity into the sample is fixed at  $10\mu\text{W}/\text{cm}^2$ . The sample used in these measurements had a  $215 \text{ \AA}$  ZnSe overlayer.

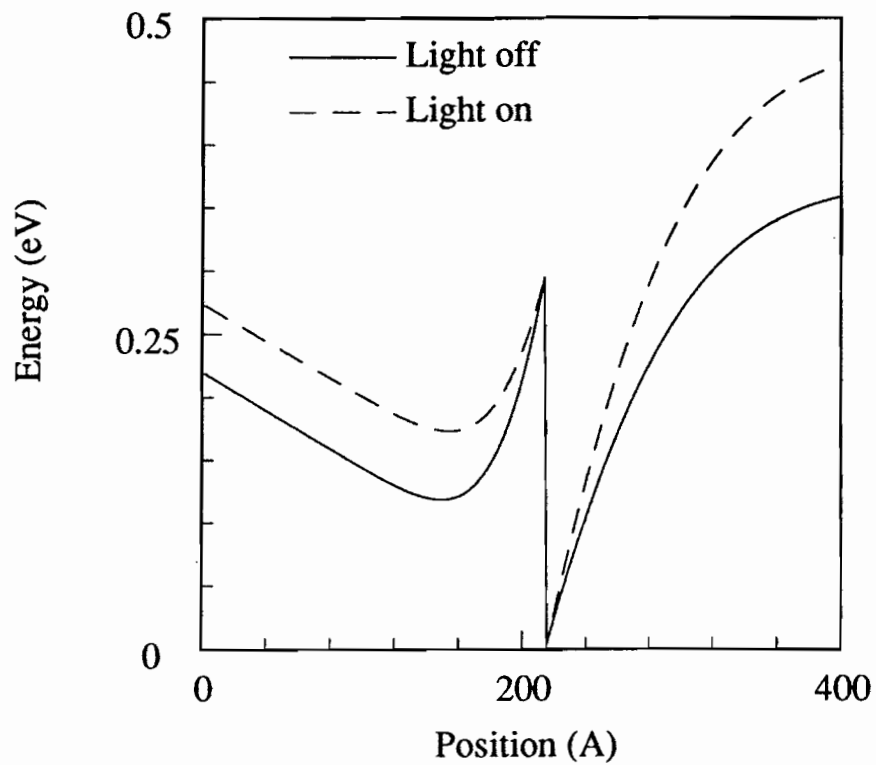


Figure 7.4: Variation of energy-band profile with photomodulation. This change was calculated based on the creation of positive interface charge. Band bending increased (decreased) in GaAs (ZnSe) side of the junction.

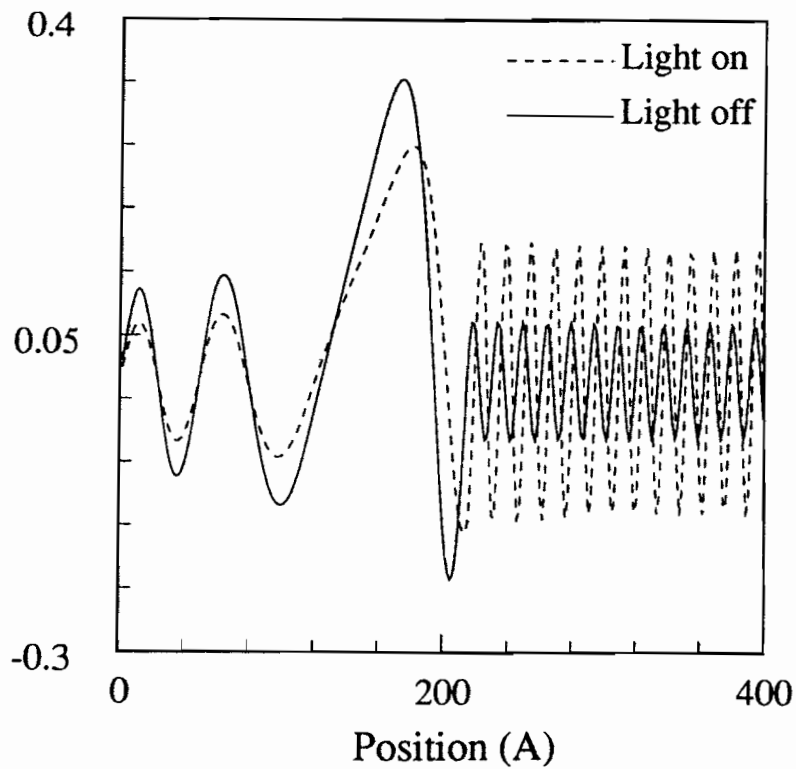


Figure 7.5: Variation of valence band wavefunction with photomodulation. There are two important changes: a-the amplitude of the wavefunction reduced in ZnSe while it increased in GaAs side of the junction, b-there is an overall shift toward the interface.

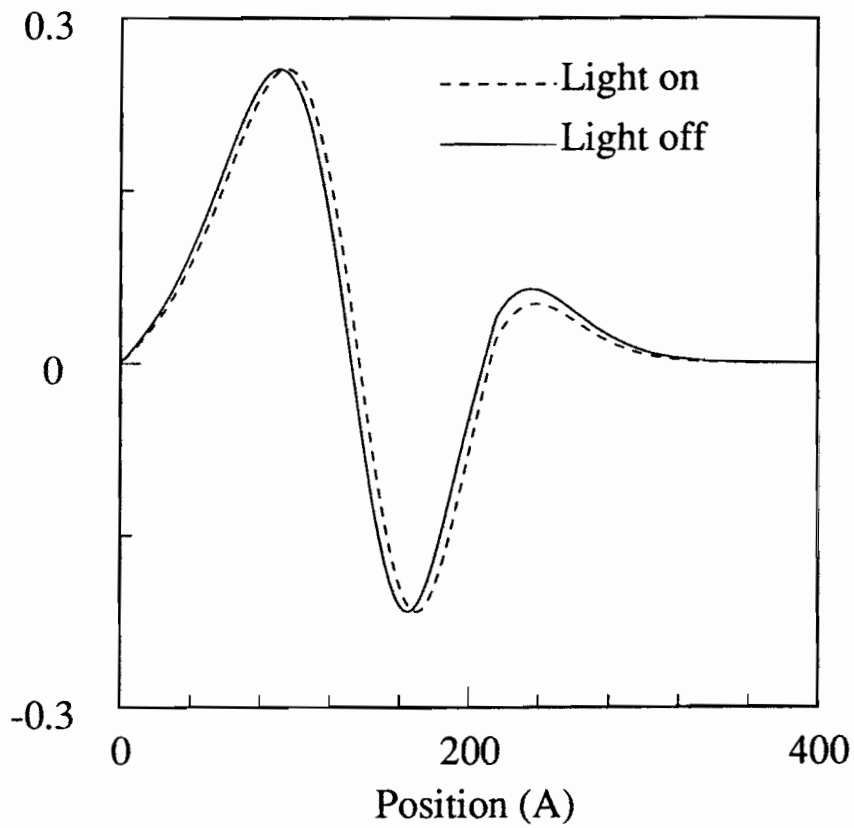


Figure 7.6: Variation of quantum well wavefunction with photomodulation. The amplitude of the wavefunction reduced within the well and the depletion area.

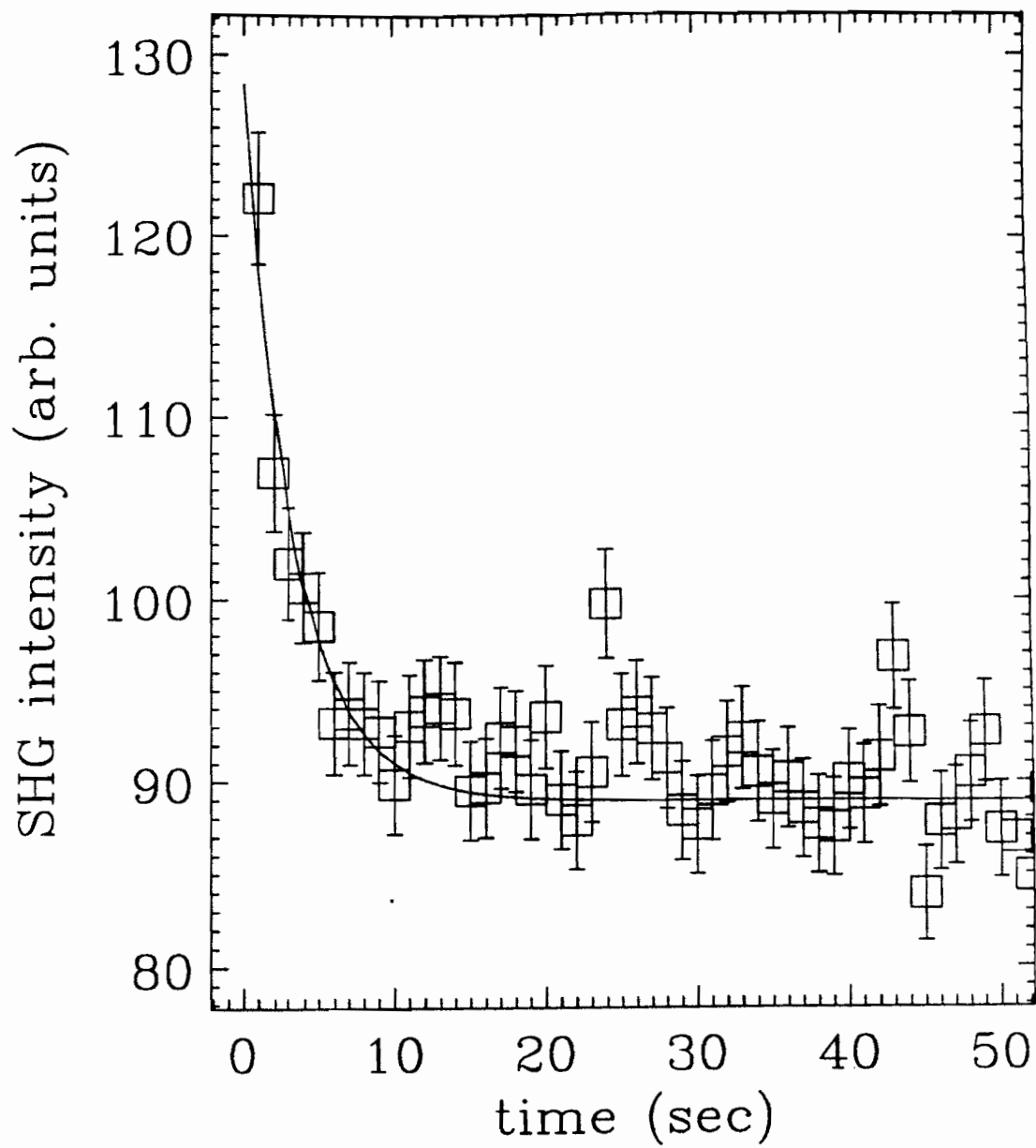


Figure 7.7: Normalized interfacial SH intensity at 2.72 eV as a function of time. The photoexcitation beam with intensity of  $5.3\mu\text{w}/\text{cm}^2$  was sent to the sample at  $t=0$ .

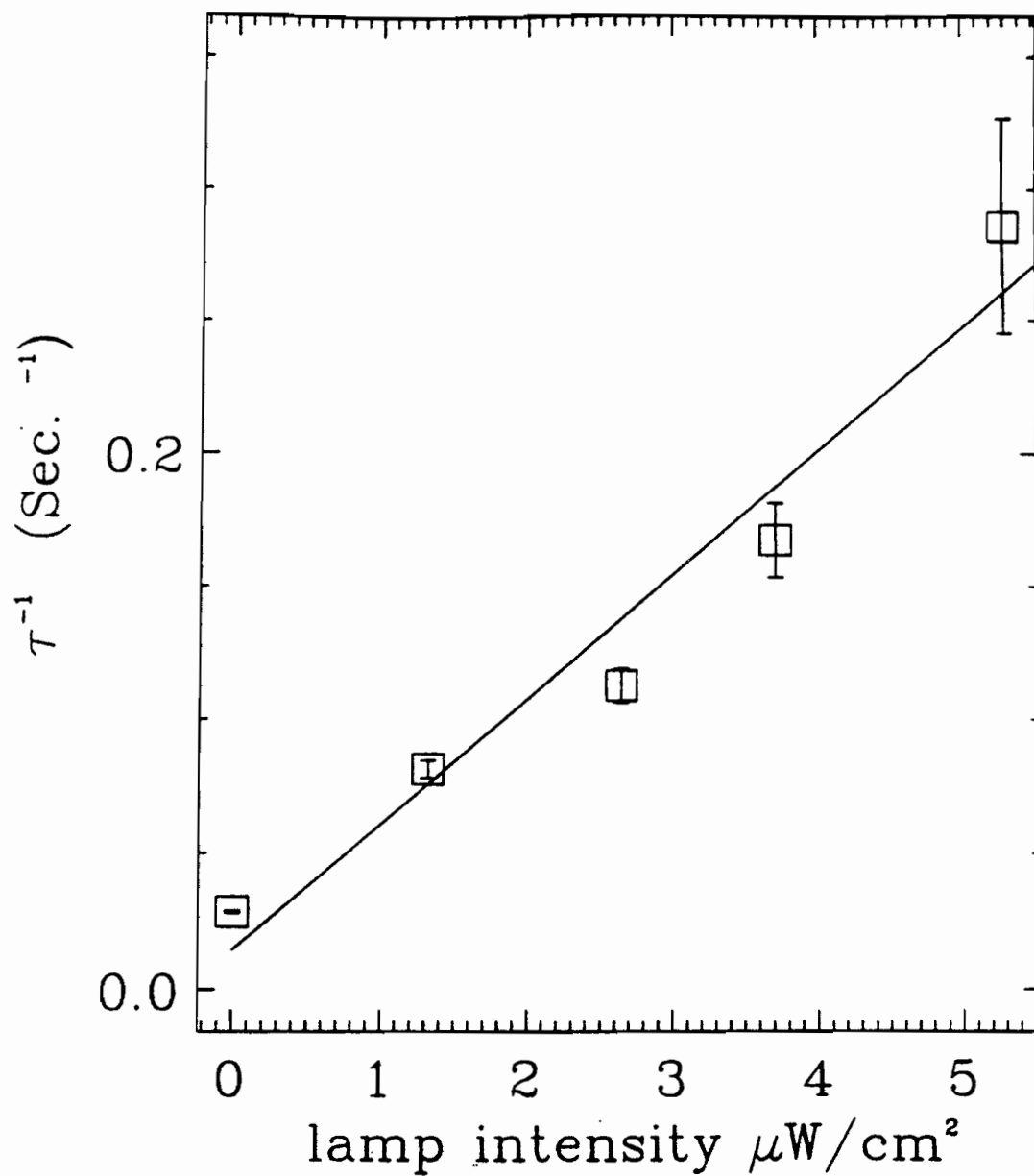


Figure 7.8: The inverse of lifetime ( $\tau$ ) as a function of intensity. The solid line is the best fit to the data.

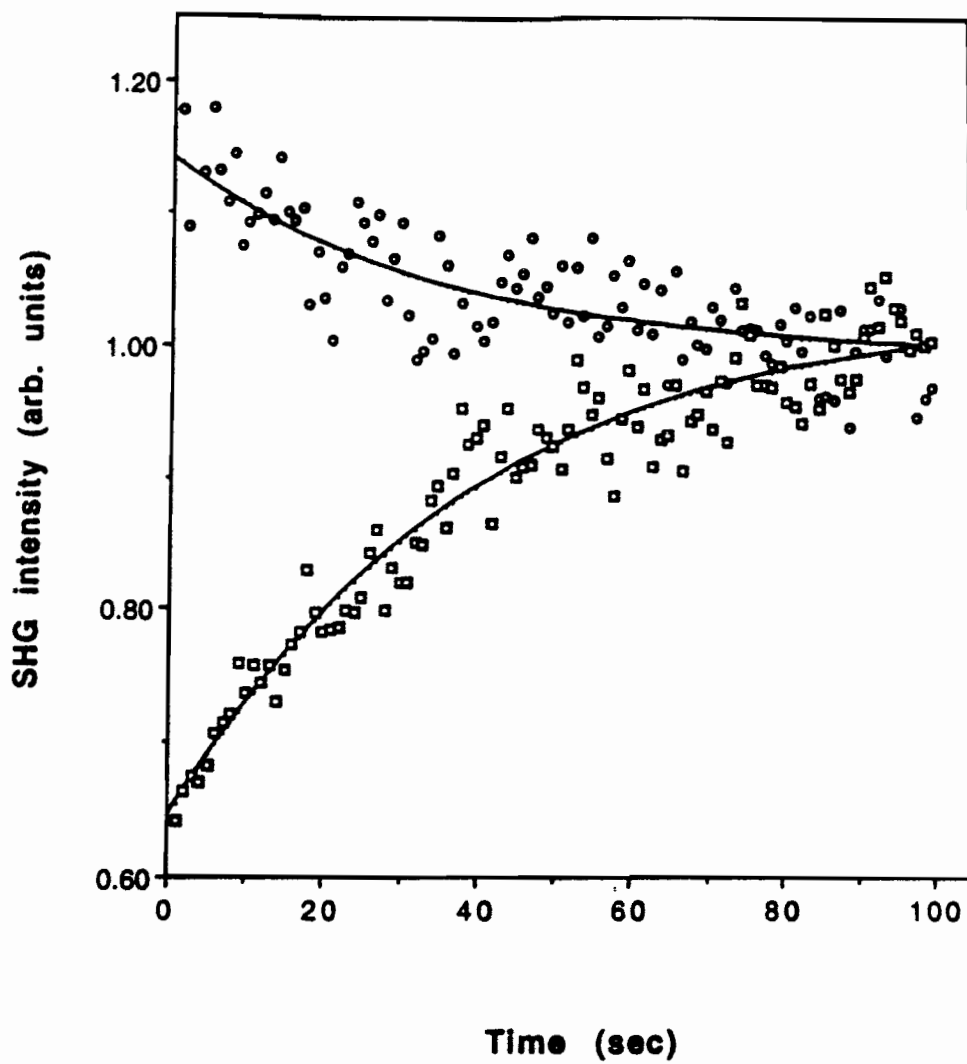


Figure 7.9: Normalized SH intensity with 2.4 eV, o, and 3.0 eV, [], lamp photon energy as a function of time. Sample was illuminated with photoexcitation beam for at least 2 minutes, then the photoexcitation shutter was closed (at  $t=0$ ) and data acquisition began.

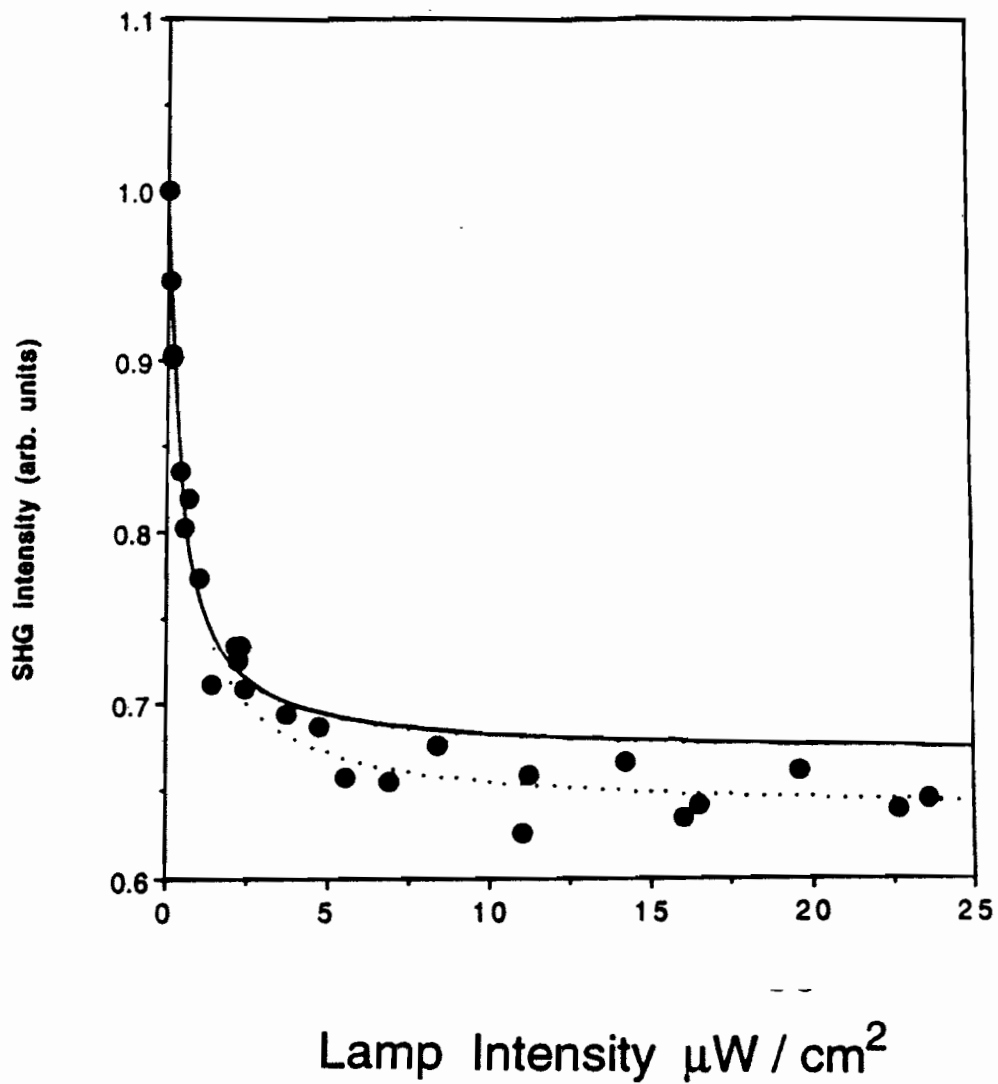


Figure 7.10: Normalized steady state SH intensity as a function of lamp intensity. The solid line is the best fit using all the available data and the dotted line is the best fit using only the low intensity portion of the data.

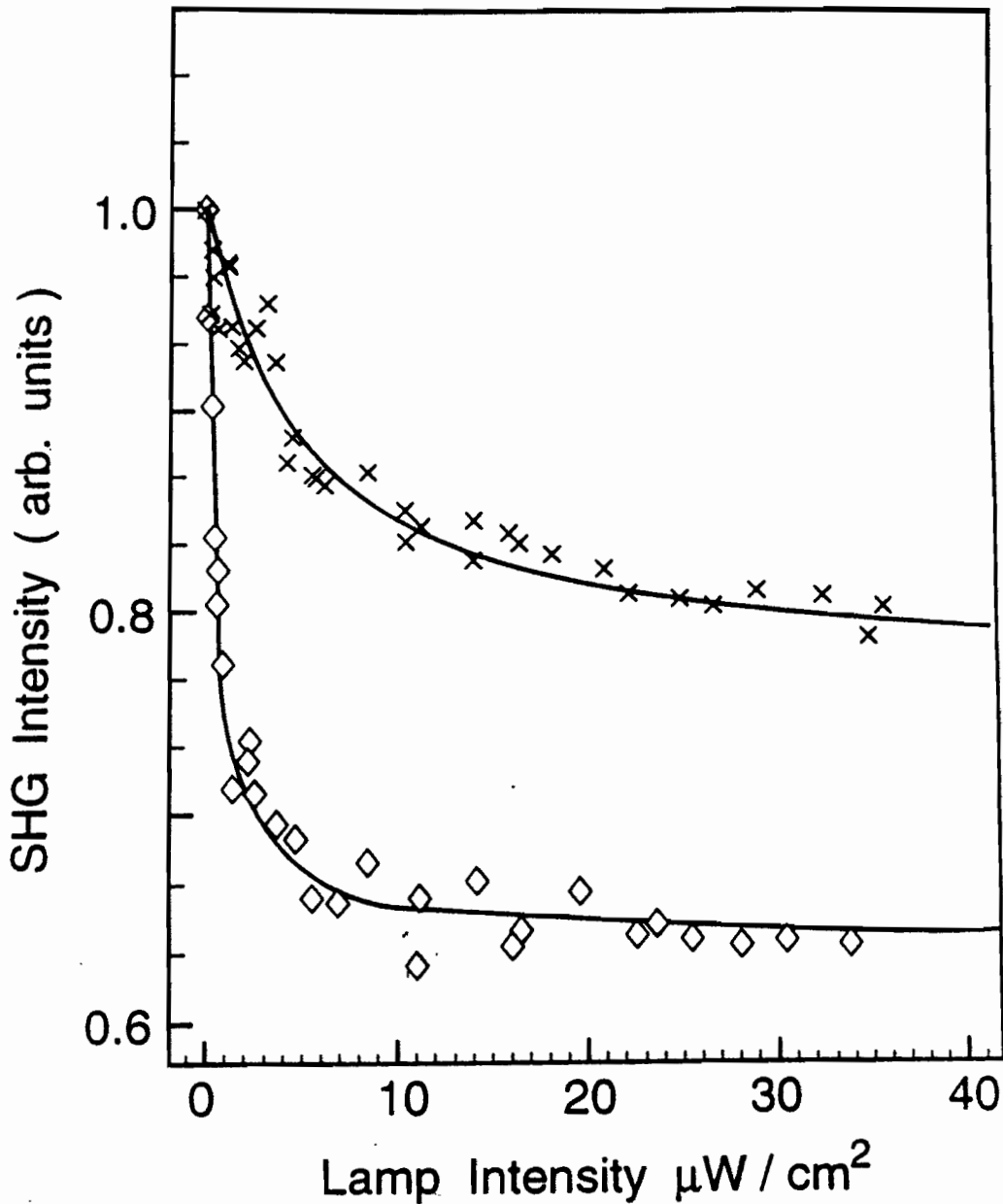


Figure 7.11: Fractional change of the interfacial resonance SHG peak intensity at 2.72 eV for 3x1 (x) and 2x4 (◇) samples as a function of lamp intensity using lamp photons with an energy of 3.0 eV. The solid lines are the best fit to the data. The SHG intensity reached its saturation level at  $\sim 10 \mu\text{W}/\text{cm}^2$  for the 2x4 sample. The saturation condition was not achieved for the 3x1 sample in our lamp intensity range.

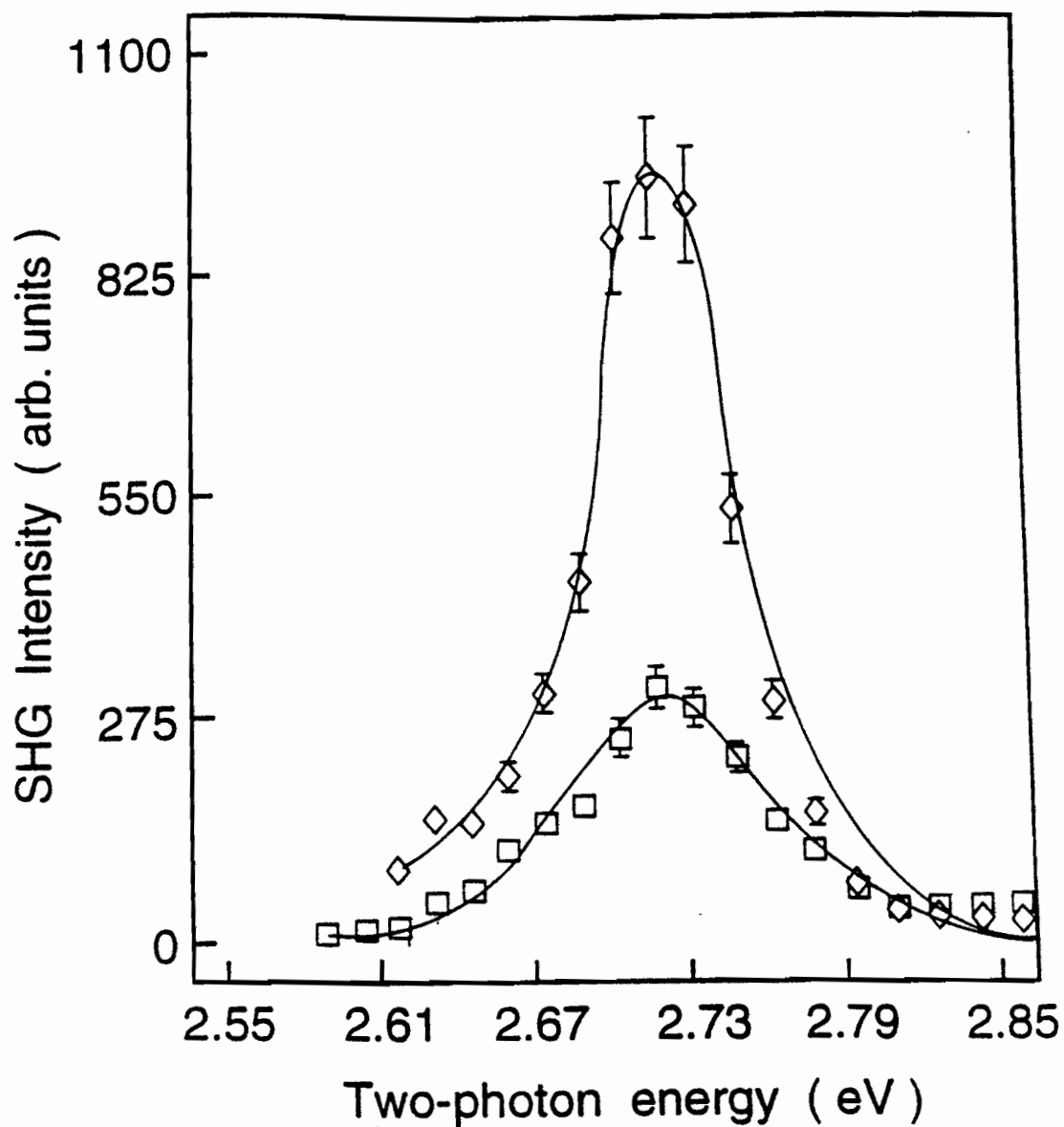


Figure 7.12: SHG spectra for 3x1 (◇) and 2x4 (□) buried GaAs surface reconstructed samples as a function of upconverted photon energy. The 3x1 sample exhibits a 4 times stronger peak nonlinearity than the 2x4 sample. The ZnSe overlayer thickness was 215 Å for both samples. Solid lines are only a guide for the eye.

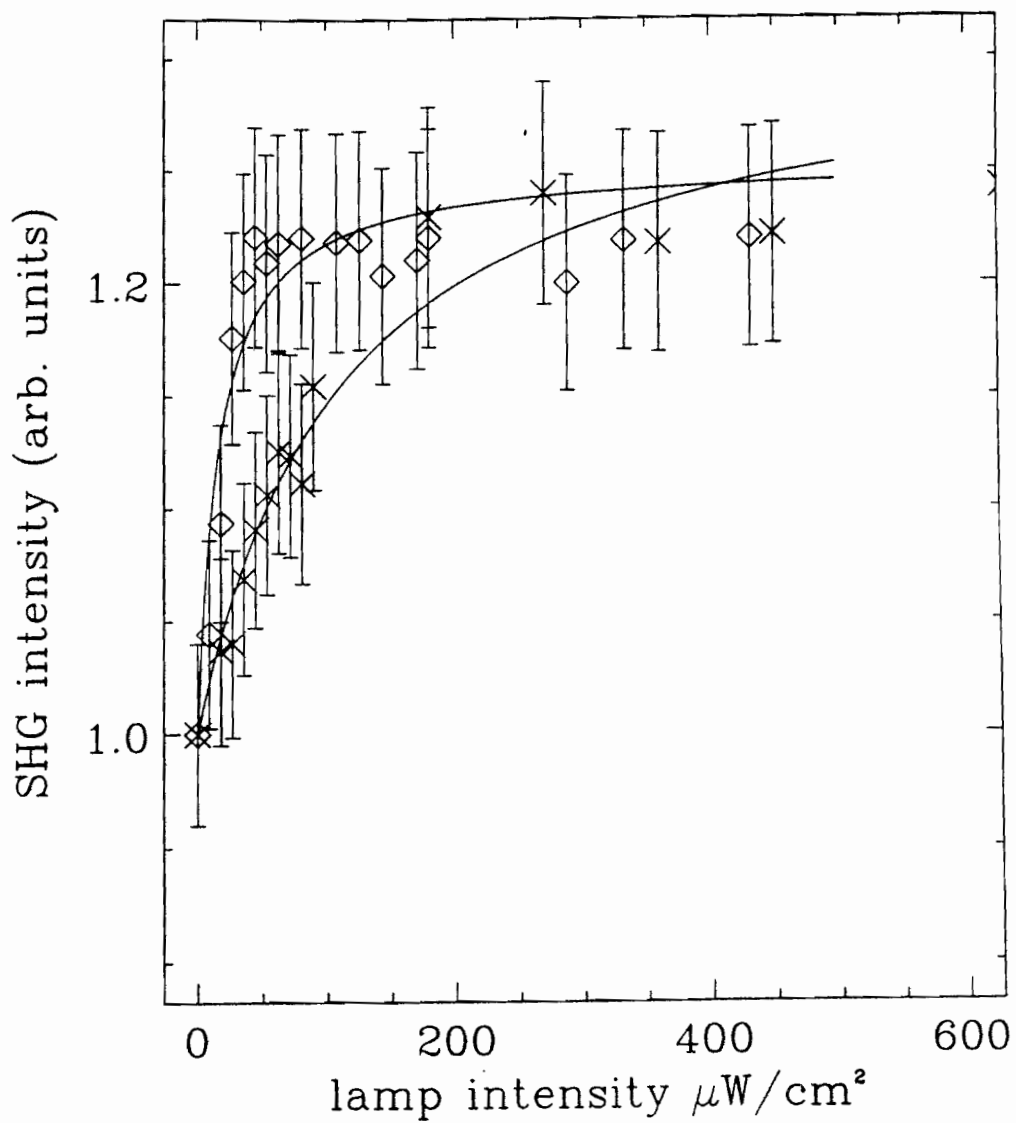


Figure 7.13: Fractional change of the interfacial resonance SHG peak intensity at 2.72 eV for 3x1 (x) and 2x4 ( $\diamond$ ) samples as a function of lamp intensity using lamp photons with an energy of 2.4 eV. The solid lines are the best fit to the data.

# Chapter 8

## Conclusion

We have used second-harmonic and sum-frequency spectroscopy to probe the electronic structure of the interface and bulk of ZnSe/GaAs(001) heterostructures. We were able to separate the bulk and interface contributions by proper choice of polarization and sample orientation.

The bulk results were as follows. The SH intensities were observed to oscillate as a function of overlayer thickness. This resulted from interference of the reflected second-harmonic generation from two adjoined nonlinear slabs. A theoretical calculation for the phenomena was presented and it was introduced as a new methodology to measure the second-order susceptibility of thin overlayer materials. For the first time, the frequency-dependent bulk,  $\chi_{xyz}^{(2)}$ , of ZnSe was measured. The sharp feature at 2.67 eV was assigned to the  $E_0$  transition.

The interface results were as follows. The interface of ZnSe/GaAs(001) systems

exhibited strong SH and SF resonances. We observed two sharp features at 2.92 and 2.72 eV. The 2.92 eV resonance was assigned to the  $E_1$  transition of buried GaAs. The spectral feature at 2.72 eV was produced as a result of virtual coupling between the ZnSe valence band and a *resonance state* of a quantum well located *across* the junction in the GaAs conduction band. The interfacial quantum well was brought about by interdiffusion of Zn into GaAs and Ga into ZnSe during sample growth.

The interfacial resonance at 2.72 eV was used to investigate the pseudomorphic growth and critical thickness. The sensitivity of the SH resonance to surface reconstructions of buried GaAs was also demonstrated.

Linear photomodulation and second-harmonic generation were combined as a new method to investigate solid-solid interfaces. Using this technique, we have studied the trapping of free carriers in ZnSe/GaAs(001) heterointerfaces. The band-flattening of the interfacial band profile was described by a trapping mechanism. This mechanism was formulated and used along with the time dependent measurement to deduce the recombination lifetime of interfacial traps and relative interfacial trap densities as a function of the buried surface reconstructions.

# Appendix A

## $\chi^{(2)}$ and Symmetry

This appendix will discuss the relationship between the tensor elements by utilizing the structural symmetry of the medium. First we explain Neumann's principle, which is the initial step in relating the symmetry of a material to the physical property of a system. Neumann's principle simply states that any macroscopic physical property of a medium, for example  $\chi^{(2)}$ , at least has the symmetry of the point group of the space group. Using this principle and the fact that the second-order susceptibility tensor,  $\chi_{ijk}^{(2)}$ , transforms similar to the Cartesian coordinates,  $r_i r_j r_k$ , we can determine the relationship between the tensor elements. As an example the relation between the tensor elements of a system with  $C_{4v}$  (e.g. surface of fcc[001]) and  $\bar{4}3m$  symmetry (e.g. bulk of zinc-blende crystal) will be discussed below.

### $C_{4v}$ system:

This system is invariant under the symmetry elements of  $E$ ,  $2C_4$ ,  $C_2$ ,  $\sigma_v$  and  $\sigma_d$ . The

definition of each operator is given in any standard group theory textbook [44, 45]. Because of Neumann's principle,  $\chi_{ijk}$  must also be invariant under the symmetry elements of group  $C_{4v}$ . Since  $\chi_{ijk}$  transforms like  $r_i r_j r_k$ , we only need to study the coordinate transformation under the symmetry operators. However we only need to investigate the transformation under the generators of the point group and not all the operators. The group generators of  $C_{4v}$  are  $\sigma_v$  and  $C_4$ .

$\sigma_v$  is reflection in a vertical plane. This is the indication of the existence of a vertical mirror plane in the system. If we take the coordinate axis such that  $\sigma_v$  intercepts the horizontal ( $xy$ ) plane along  $y$ -axis, we can write

$\sigma_v$ :

$$x \rightarrow -x$$

$$y \rightarrow +y$$

$$z \rightarrow +z$$

In other words,

$$xyz \rightarrow -xyz \quad \text{that is,} \quad \chi_{xyz} \rightarrow -\chi_{xyz}.$$

We know that the system is invariant under  $\sigma_v$ , therefore

$$\chi_{xyz} = -\chi_{xyz} = 0.$$

We can generalize this and set  $\chi_{ijk} = 0$  if an odd number of  $x$  appears in the subscript. That is

$$\chi_{xxx} = \chi_{xyz} = \chi_{yxz} = \dots = 0.$$

The system is also invariant under the  $C_4$  operator, which is a rotation by 90 degrees. This implies that there must be another mirror plane perpendicular to the  $(xy)$  plane which intercepts the horizontal plane along the  $x$ -axis. Under this reflection operator all  $\chi_{ijk} = 0$  if an odd number of  $y$  appears in the subscript. That is

$$\chi_{yyy} = \chi_{yxx} = \chi_{yzz} = \dots = 0.$$

The  $C_4$  operator also implies that

$$x \rightarrow y$$

$$y \rightarrow -x$$

$$z \rightarrow z$$

thus,

$$\chi_{xxz} = \chi_{yyz}$$

$$\chi_{xzx} = \chi_{yzy}$$

$$\chi_{zxx} = \chi_{zyy}$$

These elements and  $\chi_{zzz}$  are the only nonzero elements for  $C_{4v}$  symmetry. We must note that these relationships will be even more simplified if we only considered the SHG process. For SHG (but not SFG) we can write;  $\chi_{ijk} = \chi_{ikj}$ .

**$\bar{4}3m$  [001] symmetry:**

We are interested in the zinc-blende crystal structure with a (001) face. The bulk of this system carries a  $43m$  symmetry group. The generators of this group are

$C_3[111]$  and  $S_4^3$ . The  $S_4$  operator is a rotation by  $2\pi/4$  followed by a reflection in the horizontal plane, and  $S_4^3 = S_4S_4S_4$ . If we take  $(xy)$  as the horizontal plane, then

$S_4^3$  :

$$x \rightarrow -y$$

$$y \rightarrow x$$

$$z \rightarrow -z.$$

This operation suggests that the only nonzero elements are

$$\chi_{yyx} = -\chi_{xxy}, \chi_{xyy} = -\chi_{yxx}, \chi_{zzz} = \chi_{yyz}$$

$$\chi_{xzy} = \chi_{yzx}, \chi_{xyx} = \chi_{yxz}, \chi_{yxz} = \chi_{xyx}$$

and

$$\chi_{zxy} = \chi_{zyx}.$$

We should note that the  $S_4^3$  symmetry is responsible for  $\chi_{zzz} = 0$ . To identify the other relationships among these elements we must study the transformation under  $C_3[111]$ . Under this operator we have

$C_3[111]$  :

$$x \rightarrow y$$

$$y \rightarrow z$$

$$z \rightarrow x.$$

This makes all  $\chi_{ijk}$  equal to each other when  $i \neq j \neq k$  and

$$-\chi_{112} = \chi_{221} = \chi_{332} = \chi_{113} = 0,$$

$$\chi_{223} = \chi_{133} = \chi_{211} = \chi_{332} = 0,$$

$$-\chi_{211} = \chi_{122} = \chi_{233} = \chi_{311} = 0.$$

Thus, the only nonzero elements are  $\chi_{ijk}$  with  $i \neq j \neq k$ .

## Appendix B

# Boundary Conditions at Vacuum/crystal interface

In the p-in/s-out polarization configuration the boundary conditions at vacuum/crystal interface ( $z = 0$ ) have the form

$$\checkmark \quad E_{\perp,R10} = E_{\perp,f1} + \frac{4\pi P_{\perp,1}}{\epsilon_{b1} - \epsilon_{f1}}, \quad (\text{B.1})$$

and

$$\checkmark \quad E_{\perp,R10} k_{f0,z} = E_{\perp,f1} k_{f1,z} + \frac{4\pi P_{\perp,1}}{\epsilon_{b1} - \epsilon_{f1}} k_{b1,z}. \quad (\text{B.2})$$

Eqs. (B.1) and (B.2) are derived from the continuity for the tangential components of the electric and the magnetic fields at  $z = 0$ . These equations lead to the determination of  $E_{\perp,R10}$ , given in Eq. (2.28), and  $E_{\perp,f1}$ ,

$$E_{\perp,f1} = \frac{4\pi P_{\perp,1}}{\epsilon_{b1} - \epsilon_{f1}} \left[ \frac{k_{f0,z} - k_{b1,z}}{k_{f1,z} - k_{f0,z}} \right]. \quad (\text{B.3})$$

# Appendix C

## Solution of The Nonlinear Wave

## Equation With Position

## Dependent $\chi^{(2)}$

Localized electric fields or deformation potentials can make  $\chi^{(2)}$  position dependent. If the second-order susceptibility tensor,  $\chi^{(2)}$ , decays exponentially in the direction of  $\hat{z}$  with decay constant  $\alpha$ , we can write the position dependent polarization  $P^{(2\omega)}$  as

$$P = P_0 e^{-\alpha(z+d)}, \quad (\text{C.1})$$

where  $P_0$  is the polarization at the interface  $z = -d$ . Then, assuming the linear dielectric constant is still independent of position, the nonlinear wave equation (1)

has a solution of the form (3), but with a new, modified,  $\mathbf{k}_b$ ,

$$\mathbf{k}_b = 2\mathbf{k}_t + i\alpha\hat{z}. \quad (\text{C.2})$$

This leads to a new form for  $\epsilon_b(2\omega)$ ,

$$\epsilon_b(2\omega) = \epsilon(\omega) + \frac{c^2}{4\omega^2} \left( 4i\alpha\mathbf{k}_t \cdot \hat{z} - \alpha^2 \right). \quad (\text{C.3})$$

Thus the polarization decay indirectly affects the free wave propagation through the boundary conditions, and of course, it directly affects the bound wave amplitude in the  $\hat{z}$  direction.

## Appendix D

# Exact Boundary Conditions at Buried Interface

To solve the general problem of reflection at the boundary between two nonlinear media, we look for solutions on *both sides* of the interface in the form of Eq. (3). The general boundary conditions in the p-in/s-out polarization configuration at the buried interface which include the nonlinearity of both slabs can be written as

(a) continuity of  $E_{\parallel}$

$$E_{f1} e^{i\mathbf{k}_{f1} \cdot \mathbf{r}_0} + \frac{4\pi P_{\perp,1}}{\epsilon_{b1} - \epsilon_{f1}} e^{i\mathbf{k}_{b1} \cdot \mathbf{r}_0} + E_{fr} e^{i\mathbf{k}_{fr1} \cdot \mathbf{r}_0} + \frac{4\pi P'_{\perp,1}}{\epsilon_{b1} - \epsilon_{f1}} e^{i\mathbf{k}_{br1} \cdot \mathbf{r}_0} = E_{f2} e^{i\mathbf{k}_{f2} \cdot \mathbf{r}_0} + \frac{4\pi P_{\perp,2}}{\epsilon_{b2} - \epsilon_{f2}} e^{i\mathbf{k}_{b2} \cdot \mathbf{r}_0}, \quad (\text{D.1})$$

(b) continuity of  $H_{\parallel}$

$$E_{f1}k_{f1,z} e^{ik_{f1}\cdot\mathbf{r}_0} + \frac{4\pi P_{\perp,1}}{\epsilon_{b1} - \epsilon_{f1}} k_{b1,z} e^{ik_{b1}\cdot\mathbf{r}_0} - E_{fr}k_{f1,z} e^{ik_{fr1}\cdot\mathbf{r}_0} - \frac{4\pi P'_{\perp,1}}{\epsilon_{b1} - \epsilon_{f1}} k_{b1,z} e^{ik_{br1}\cdot\mathbf{r}_0} = E_{f2}k_{f2,z} e^{ik_{f2}\cdot\mathbf{r}_0} + \frac{4\pi P_{\perp,2}}{\epsilon_{b2} - \epsilon_{f2}} k_{b2,z} e^{ik_{b2}\cdot\mathbf{r}_0}. \quad (\text{D.2})$$

Here the reflected bound wave amplitude is proportional to  $P'_{\perp,1}$ , and

$$P'_{\perp,1} = r_{\parallel,12}^{(\omega)^2} P_{\perp,1}. \quad (\text{D.3})$$

$k_{fr1}$  and  $k_{br1}$  are wavevectors of the reflected free and bound wave in medium 1 respectively, and  $\mathbf{r}_0$  is the position vector at the interface.  $E_{fr}$  ( $E_{ft}$ ) is the amplitude of the reflected (refracted) free wave at  $2\omega$ . The relation between  $E_{fr}$  and the reflected SH fields in the main text, i.e.  $E_{\perp,R11}$  and  $E_{\perp,R21}$ , is further clarified below.

Eqs. (D.1-D.3) lead to the determination of  $E_{fr}$  :

$$E_{fr} = r_{\perp,12}^{(2\omega)} E_{f1} e^{-2idk_{f1,z}} + \left[ \frac{k_{b1,z} - k_{f2,z}}{k_{f1,z} + k_{f2,z}} \right] \frac{4\pi P_{\perp,1}}{\epsilon_{b1} - \epsilon_{f1}} \left[ 1 + \frac{k_{f2,z} + k_{b1,z}}{k_{f2,z} - k_{b1,z}} r_{\parallel,12}^{(\omega)^2} e^{i2dk_{b1,z}} \right] e^{-id(k_{f1,z} + k_{b1,z})} + \frac{4\pi P_{\perp,2}}{\epsilon_{b2} - \epsilon_{f2}} \left[ \frac{k_{f2,z} - k_{b2,z}}{k_{f1,z} + k_{f2,z}} \right] e^{-id(k_{f1,z} + k_{b2,z})}. \quad (\text{D.4})$$

The reflected SH field,  $E_{\perp,R11}$ , arises from the first and second terms of (D.4). The third term in (D.4) gives rise to  $E_{\perp,R21}$  of the main text. We can see how these terms arise by building up our solution from two separate boundary value problems. In the first problem we suppress the nonlinearity of the second slab. In this case

$P_{\perp,2} = 0$  in Eq. (D.4), and all harmonic waves originate from the first slab. In the second problem we ignore the harmonic waves generated in the first slab and study the effect of the nonlinearity of the second slab. In this case  $E_{f1}$  and  $P_{\perp,1}$  are zero in Eq. (D.4). The total solution is, of course, a superposition of these resulting fields.

The solution to the boundary conditions is algebraically simpler if the reflection of the fundamental field at the buried interface is small, i.e.

$$r_{\parallel,12}^{(\omega)2} \ll 1. \quad (\text{D.5})$$

Under these circumstances we can ignore both the reflected bound wave and the effect of this field on the reflected free wave,  $E_{fr}$ . This leads to the following simplifications for  $E_{\perp,R11}$ ,  $P'_{\perp,1}$ , and  $E_{\perp,R21}$ ,

$$E_{\perp,R11}^{(2\omega)} = r_{\perp,12}^{(2\omega)} E_{f1} e^{-2idk_{f1,z}} + \left[ \frac{k_{b1,z} - k_{f2,z}}{k_{f1,z} + k_{f2,z}} \right] \frac{4\pi P_{\perp,1}}{\epsilon_{b1} - \epsilon_{f1}} e^{-id(k_{f1,z} + k_{b1,z})}, \quad (\text{D.6})$$

$$P'_{\perp,1} = 0, \quad (\text{D.7})$$

$$E_{\perp,R21}^{(2\omega)} = \frac{4\pi P_{\perp,2}}{\epsilon_{b2} - \epsilon_{f2}} \left[ \frac{k_{f2,z} - k_{b2,z}}{k_{f1,z} + k_{f2,z}} \right] e^{id(k_{f1,z} - k_{b2,z})}. \quad (\text{D.8})$$

The condition (D.5) exists for our ZnSe/GaAs[001] samples, and the small correction is not included in the results presented in the main text.

## Appendix E

# Transmitted SHG From a Quartz Plate

This appendix will describe the formulation of a transmitted second-harmonic field,  $E_{f2}$ , from a nonlinear slab (e.g. quartz plate). We start with Eqs. (D1-D2) and set  $P_{\perp,2} = 0$ , and solve for the transmitted second-harmonic field:

$$E_{f2} = \frac{2\sqrt{\epsilon_{f1}} \cos \theta_{f1}}{\sqrt{\epsilon_{f1}} \cos \theta_{f1} + \cos \theta_i} E_{f1} e^{id(k_{0,z} - k_{f1,z})} + Q \frac{\sqrt{\epsilon_{f1}} \cos \theta_{f1} + \sqrt{\epsilon_{b1}} \cos \theta_{b1}}{\cos \theta_i + \sqrt{\epsilon_{f1}} \cos \theta_{f1}} e^{id(k_{0,z} - k_{b1,z})}. \quad (\text{E.1})$$

where we have used

$$k(\omega) = \frac{\omega}{c} \sqrt{\epsilon(\omega)}$$

and

$$Q = \frac{4\pi P}{\epsilon_{b1} - \epsilon_{f1}}.$$

$E_{f1}$  can be written as a function of  $E_{R10}$  and  $Q$ . That is

$$E_{f1} = E_{R10} - Q \quad (E.1)$$

where  $E_{R10}$  is described in Chapter 2. Substituting  $E_{f1}$  in Eq. (E.1), we can write

$$E_{f2} = E_{Trans.}^{(2\omega)} = Q \left\{ - \frac{2\sqrt{\epsilon_{f1}} \cos \theta_{f1} [\cos \theta_i + \sqrt{\epsilon_{b1}} \cos \theta_{b1}]}{[\sqrt{\epsilon_{f1}} \cos \theta_{f1} + \cos \theta_i]^2} e^{id(k_{0,z} - k_{f1,z})} \right. \\ \left. + \frac{\sqrt{\epsilon_{f1}} \cos \theta_{f1} + \sqrt{\epsilon_{b1}} \cos \theta_{b1}}{\sqrt{\epsilon_{f1}} \cos \theta_{f1} + \cos \theta_i} e^{id(k_{0,z} - k_{b1,z})} \right\}. \quad (E.2)$$

## Appendix F

# Linear Reflectivity of Two Adjoined Slabs

This appendix will describe the linear reflectivity from two adjoined slabs with the geometry shown in Fig. F.1. The front surface (i.e. air/first slab interface) is at  $z=0$ , and the junction is located at  $z=-d$ . The total reflected field,  $E_{total}$  can be related to the incident electric field,  $E_i$  as,

$$\frac{E_{total}}{E_i} = r_{01} + t_{01}t_{10}r_{12}e^{i\delta} + t_{01}t_{10}r_{12}^2e^{i2\delta} + \dots \quad (\text{F.1})$$

with

$$\delta = \frac{4\pi}{\lambda} \cos \theta_1 n_1. \quad (\text{F.2})$$

Here  $r_{ij}$  and  $t_{ij}$  are the Fresnel coefficients at the interface between medium  $i$  and  $j$ .  $\theta_1$  is the transmitted angle in medium 1 and  $n_1$  is the complex index of refraction of

medium 1. Eq. (F.1) can be simplified to

$$\frac{E_{total}}{E_i} = \frac{r_{01} + r_{12}e^{i\delta}}{1 + r_{12}r_{01}e^{i\delta}} \quad (\text{F.3})$$

Where we have used

$$t_{10}t_{01} + r_{01}^2 = 1 \quad \text{and} \quad r_{01} = -r_{10}.$$

It should be noted that the effects of multiple reflections are important for thin overlayers, and must be included to ensure that radiation from medium 1 reduces to zero as the first slab thickness approaches zero.

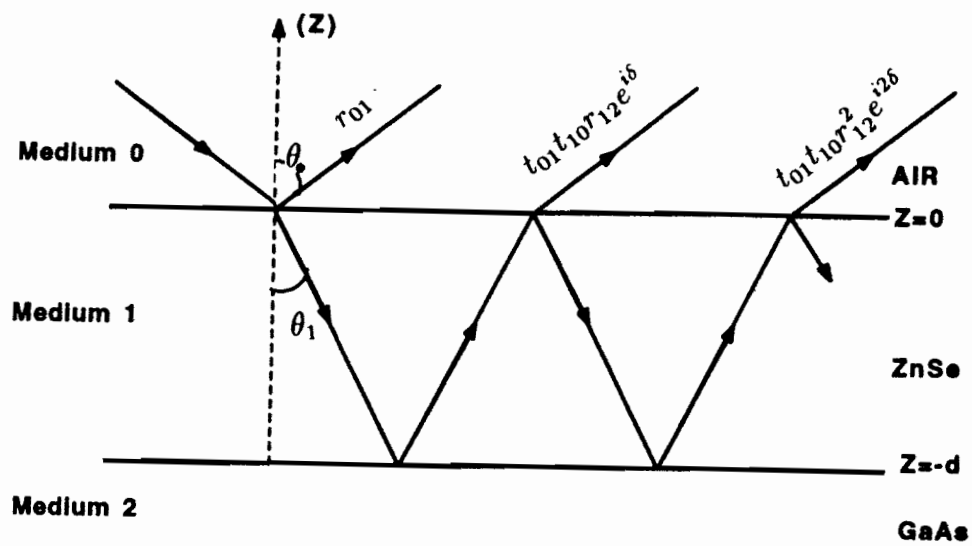


Figure F.1: Simplified coordinate for linear reflectivity

# Appendix G

## Joint Density of States: Formulation

To describe the JDOS mathematically and its relationship to the susceptibility we start with the expression of  $\chi_{zz}^{(1)}$ ,

$$\chi_{zz}^{(1)} = \frac{Ne^2}{\hbar} \sum_{cv} \left( \frac{|\langle c|z|v\rangle|^2}{\omega + \omega_{cv} + i\Gamma_{cv}} - \frac{|\langle c|z|v\rangle|^2}{\omega - \omega_{cv} + i\Gamma_{cv}} \right) \rho^{(0)} \quad (\text{G.1})$$

where  $\langle c|$  and  $\langle v|$  are the conduction and valence band states, respectively. For simplicity we assume that the conduction band is empty and the valence band is full, i.e.  $\rho^{(0)} = 1$ . We also change the summation to the integral using

$$\sum_{cv} \rightarrow \frac{2}{(2\pi)^3} \int dk \quad (\text{G.2})$$

Even though there are two summations in the above expression, we only have to perform one integration over  $k$ -space. This results from the fact that the dipole

matrix elements are diagonal in  $k$ -space. With these changes we can rewrite the expression for  $\chi_{zz}^{(1)}$  as

$$\chi_{zz}^{(1)} = \frac{Ne^2}{\hbar} \frac{2}{(2\pi)^3} \int |\langle c|z|v \rangle|^2 \frac{-2\omega_{cv}}{\omega_{cv}^2 - (\omega + i\Gamma_{cv})^2} dk. \quad (\text{G.3})$$

Now if we write  $dk$  in terms of an element of area with a constant energy surface,  $E = \hbar\omega_{cv}$ , then

$$dk = dS_{cv} dk_n \quad (\text{G.4})$$

where  $dS_{cv}$  is an element of the surface in  $k$ -space such that  $\omega_{cv}$  is constant.  $dk_n$  is the normal component of  $dk$  on  $dS_{cv}$ . This leads to

$$dk = \frac{dS_{cv}}{|\nabla_k \omega_{cv}|} d\omega_{cv}. \quad (\text{G.5})$$

Thus

$$\chi_{zz}^{(1)} = \frac{Ne^2}{\hbar} \frac{4}{(2\pi)^3} \int_{\omega_{cv}} \int_{S_{\omega_{cv}=\omega}} |\langle c|z|v \rangle|^2 \frac{-\omega_{cv}}{\omega_{cv}^2 - (\omega + i\Gamma_{cv})^2} \frac{dS_{cv}}{|\nabla_k \omega_{cv}|} d\omega_{cv}. \quad (\text{G.6})$$

Now we can write an expression for the dielectric constant,  $\epsilon_{zz}(\omega)$  as

$$\epsilon_{zz}(\omega) = 4\pi\chi_{zz}^{(1)} + 1$$

which leads to

$$\epsilon_{zz}(\omega) = 1 + \frac{Ne^2}{\hbar\pi^2} \int_{\omega_{cv}} \int_{S_{\omega_{cv}=\omega}} |\langle c|z|v \rangle|^2 \frac{-2\omega_{cv}}{\omega_{cv}^2 - (\omega + i\Gamma_{cv})^2} \frac{dS_{cv}}{|\nabla_k \omega_{cv}|} d\omega_{cv} dk \quad (\text{G.7})$$

or

$$\epsilon_{zz}(\omega) = 1 + \frac{2Ne^2}{\hbar\pi^2} \int_{\omega_{cv}} \int_{S_{\omega_{cv}=\omega}} \frac{|\langle c|P_z|v \rangle|^2 / m^2 \omega_{cv}}{\omega_{cv}^2 - (\omega + i\Gamma_{cv})^2} \frac{dS_{cv}}{|\nabla_k \omega_{cv}|} d\omega_{cv} dk. \quad (\text{G.8})$$

We have used the relationship  $|\langle c|P_z|v\rangle|^2 = -m^2\omega_{cv}^2|\langle c|z|v\rangle|^2$  in the above expression. Where  $P$  is the dipole operator. In most materials, including GaAs and ZnSe,  $\omega_{cv}$  is much larger than  $\Gamma_{cv}$ . With this in mind we can use the Cauchy integration to write  $\epsilon_{zz}(\omega)$  in the following form:

$$\begin{aligned} \epsilon_{zz}(\omega) = 1 + \frac{2Ne^2}{\hbar\pi} \mathbf{P}\mathbf{V} \int_{\omega_{cv}} \int_{\mathbf{S}_{\omega_{cV}=\omega}} \frac{|\langle c|P_z|v\rangle|^2/m^2\omega_{cv}}{\omega_{cv}^2 - \omega^2} \frac{d\mathbf{S}_{cv}}{|\nabla_k \omega_{cv}|} d\omega_{cv} \\ + \frac{2\pi Ne^2}{\hbar\pi} \frac{i}{2\pi\omega} \int_{\mathbf{S}_{\omega_{cV}=\omega}} \frac{|\langle c|P_z|v\rangle|^2/m^2\omega_{cv}}{|\nabla_k \omega_{cv}|} d\mathbf{S}_{cv} \end{aligned} \quad (\text{G.9})$$

The imaginary part of this function is

$$Im\epsilon_{zz}(\omega) = \frac{Ne^2}{\hbar\pi m^2\omega^2} \int_{\mathbf{S}_{\omega_{cV}=\omega}} \frac{|\langle c|P_z|v\rangle|^2}{|\nabla_k \omega_{cv}|} d\mathbf{S}_{cv} \quad (\text{G.10})$$

It is known that  $|P_{cv}|^2$  varies slowly in many cases [107], therefore it can be taken outside the integral. The result is

$$Im\epsilon_{zz}(\omega) = 8N(\pi e/m\omega)^2 |P_{cv}|^2 J_{cv}(\omega) \quad (\text{G.11})$$

where

$$J_{cv}(\omega) = \frac{1}{(2\pi)^3 \hbar} \int_{\mathbf{S}_{\omega_{cV}=\omega}} \frac{d\mathbf{S}_{cv}}{|\nabla_k \omega_{cv}|_{\omega_{cv}=\omega}} \quad (\text{G.12})$$

The function  $J_{cv}$  is the joint density of states (JDOS).

# Appendix H

## Electron Trapping

Photogeneration of EHP with lamp photon energies less than the ZnSe band gap and greater than GaAs band gap can only occur in GaAs side of the heterostructure. Under these conditions electrons migrate toward the interface. Some of these carriers are captured by interfacial electron traps. In this appendix we are interested in calculating the deviation of the trapped electron density,  $\delta n_t$ , from its equilibrium value,  $n_{t0}$ . The localized rate equation for  $\delta n_t$  is

$$\frac{\partial n_t}{\partial t} = k_{1e}n(N_e - n_t) - k_{2e}pn_t - r_e n_t. \quad (\text{H.1})$$

The subscript “e” stands for electron and the definition of each parameter is given for hole trap in the text. Eq. (H.1) leads to the time dependent value of  $n_t$ . After subtracting the steady state value of the trap density in the absence of light,  $n_{t0}$ , we can write

$$\delta n_t = A_e e^{-t/\tau_e} + \frac{k_{1e}(k_{2e}p_0 + r_e)\alpha_{2e}N_e\tau_{oe}I_l}{\alpha_{2e}k_{1e}I_l + \tau_{oe}^{-1}}. \quad (\text{H.2})$$

Where

$$\tau_e = \frac{1}{(k_{1e}n_o + k_{2e}p_o + r_e) + \alpha_{2e}k_{1e}I_l} \quad (\text{H.3})$$

and

$$\tau_{eo} = \tau_e \quad \text{with} \quad I_l = 0. \quad (\text{H.4})$$

The expression for the perturbation Hamiltonian, second-order susceptibility and the SHG intensity result when the subscript "h", for hole, is replaced by "e", for electron, in Eq. ( 7.7- 7.13).

# Bibliography

- [1] F. J. Himpsel, U. O. Karlsson, J. F. Morar, D. Rieger and J. A. Yarmoff, *Phys. Rev. Lett.* **56**, 1497 (1986).
- [2] D. Rieger, F. J. Himpsel, U. O. Karlsson, F. R. McFeely, J. F. Morar and J. A. Yarmoff, *Phys. Rev. B* **34**, 7295 (1986).
- [3] A. B. McLean and F. J. Himpsel, *Phys. Rev. B* **39**, 1457 (1989).
- [4] T. F. Heinz, F. J. Himpsel, E. Palange, and E. Burstein, *Phys. Rev. Lett.* **63**, 644 (1989).
- [5] Y. Z. Liu, R. J. Anderson, R. A. Milano, and M. J. Cohen, *Appl. Phys. Lett.* **40**, 967 (1982).
- [6] H. Kroemer, *J. Appl. Phys.* **52**, 873 (1980).
- [7] R. People, K. W. Wecht, K. Alavi, and A. Y. Cho, *Appl. Phys. Lett.* **43**, 118 (1983).
- [8] J. Singh and K. D. Bajaj, *J. Appl. Phys.* **57**, 5433 (1985).

- [9] A. R. Peaker and H. G. Grimmiess, "*Low-Dimensional Structures in Semiconductors From Basic Physics to Applications*", NATO ASI Series (Plenum Press, New York, 1992).
- [10] C. Weisbuch and B. Vinter, "*Quantum Semiconductor Structures Fundamentals and Applications*" (Academic Press, Boston, 1991).
- [11] G. Bastard, "*Wave Mechanics Applied to Semiconductor Heterostructures*" (Halsted Press, New York, 1988).
- [12] M. Altarelli in "*Heterojunctions and Superlattices*" (Springer-Verlag, New York, 1986), G. Allan, G. Bastard, N. Boccara, M. Lannoo and M. Voos, eds.
- [13] J. Barker in "*The Physics and Fabrication of Microstructures and Microdevices*" (Springer-Verlag, New York, 1986) M. Kelly, and C. Weisbuch, eds.
- [14] L. D. Bell, and W. J. Kaiser, Phys. Rev. Lett. **61**, 2368 (1988).
- [15] W. J. Kaiser and L. D. Bell, Phys. Rev. Lett. **60**, 1406 (1988).
- [16] L. J. Brillson, R. E. Viturro, J. L. Shaw, and H. W. Richter, J. Vac. Sci. Tech. A **6**, 1437 (1988).
- [17] D. E. Aspnes and A. A. Studra, Phys. Rev. Lett. **54**, 1956 (1985).
- [18] H. W. K. Tom, T. F. Heinz and Y. R. Shen, Phys. Rev. Lett. **51**, 1983 (1983).
- [19] T. F. Heinz, M. M. T. Loy and W. A. Thompson, Phys. Rev. Lett. **54**, 63 (1985).

- [20] H. W. K. Tom and G. D. Aumiller, Phys. Rev. B **33**, 8818 (1986).
- [21] E. Ghahramani, D. J. Moss, and J. E. Sipe, Phys. Rev. Lett. **64**, 2815 (1990).
- [22] T. F. Heinz, F. J. Himpsel, E. Palange, and E. Burstein, Phys. Rev. Lett. **63**, 644 (1989).
- [23] J. F. McGilp, and Y. Yeh, Solid State Comm. **59**, 91 (1986).
- [24] M. S. Yeganeh, A. G. Yodh, and M. C. Tamargo, in *Proceedings of the Conference on Quantum Electronics and Laser Science (QELS '91)*, Baltimore, Maryland (1991). J. C. Hamilton, R. T. Tung, and H. W. K. Tom, *ibid.*
- [25] M. S. Yeganeh, J. Qi, A. G. Yodh, and M. C. Tamargo, Phys. Rev. Lett. **68**, 3761 (1992).
- [26] M. A. Haase, J. Qiu, J. M. Depuydt, and H. Cheng, Appl. Phys. Lett. **59**, 1272 (1991).
- [27] M. C. Tamargo, R. E. Nahory, B. J. Skromme, S. M. Shibli, A. L. Weaver, R. J. Martin, and H. H. Farrell, J. Vac. Sci. Technol. B **10**, 692 (1992).
- [28] T. Yao, Y. Okada, S. Matsui, K. Ishida, and I. Fujimoto, J. Crystal Growth **81**, 518 (1987).
- [29] K. Mohammed and D. A. Cammack, Appl. Phys. Lett. **50**, 37 (1987).
- [30] H. Mitsuhashi, I. Mitsuishi, M. Mizuta, and H. Kukimoto, Jap. J. Appl. Phys. **24**, L578 (1985).

- [31] D. B. Laks, C. G. Van de Walle, G. F. Neumark, and S. T. Pantelides, *Phys. Rev. Lett.* **66**, 648 (1991).
- [32] L. Kassel, H. Abad, J. W. Garland, P. M. Raccach, J. E. Potts, M. A. Haase, and H. Cheng, *Appl. Phys. Lett.* **56**, 42 (1990).
- [33] M. S. Yeganeh, J. Qi, A. G. Yodh, and M. C. Tamargo, *Phys. Rev. Lett.* **69**, 3579 (1992).
- [34] M. S. Yeganeh, J. Qi, J. P. Culver, A. G. Yodh, and M. C. Tamargo, *Phys. Rev. B* **46**, 1603 (1992).
- [35] M. S. Yeganeh, J. Qi, A. G. Yodh, and M. C. Tamargo, (manuscript in preparation).
- [36] See for example Y.R. Shen, *The Principles of Nonlinear Optics* (Wiley- Interscience, New York, 1984).
- [37] J. E. Sipe, D. J. Moss and H. M. van Driel, *Phys. Rev. B* **35**, 1129 (1987).
- [38] N. Bloembergen, R. K. Chang, S. S. Jha and C. H. Lee, *Phys. Rev.* **174**, 813 (1968).
- [39] J. A. Litwin, J. E. Sipe and H. M. van Driel, *Phys. Rev. B* **31**, 5543 (1983).
- [40] P. Guyot-Sionnest, W. Chen and Y. R. Shen, *Phys. Rev. B* **33**, 8254 (1986).
- [41] O. Keller, *Phys. Rev. B* **33**, 990 (1986).

- [42] E. Adler, Phys. Rev. **134**, A728 (1964).
- [43] A. Yariv, "*Quantum Electronics*" (Wiley, New York, 1988) Third Edition.
- [44] M. Tinkham, "*Group Theory and Quantum Mechanics*"
- [45] G. Burns, "*Solid State Physics*" (Academic Press, Orlando, 1985).
- [46] N. Bloembergen, and P.S. Pershan, Phys. Rev. **128**, 606 (1962).
- [47] H. Lotem, G. Koren, and Y. Yacoby, Phys. Rev. B, **9**, 3532 (1974).
- [48] D. Bethune, A. J. Schmidt, and Y. R. Shen, Phys. Rev. B, **11**, 3867 (1975).
- [49] R. K. Chang, J. Ducuing, and N. Bloembergen, Phys. Rev. Lett. **15**, 415 (1965).
- [50] F. G. Parsons, and R. K. Chang, Opt. Comm. **3**, 173 (1971).
- [51] It can be shown that the ratio of second-order polarization,  $P^{(2)}$ , to linear polarization,  $P^{(1)}$ , depends on  $E/E_{atomic}$ , where  $E$  is the electric field of the light source and  $E_{atomic}$  is the binding force per charge. For a typical value of  $E_{atomic} \approx 10^8 V/cm$  and  $P^{(2)}/P^{(1)} \approx 10^{-5}$  a field of  $E = 1KV/cm$  is needed.
- [52] Maker fringes are generated by interference of bound and free waves in the crystal. This interference can be observed by changing the angle of incidence. This change alters the relative phase of these fields and produce the interference pattern known as Maker fringes.

- [53] M.C. Tamargo, R. Nahory, B. J. Skromme, S. M. Shibli, A. L. Weaver, R. J. Martine and H. H. Farrell, *J. Cryst. Growth*, **111**, 741 (1991).
- [54] B. O. Seraphin, and H. E. Bennett, *Semiconductors and Semimetals* (Academic, New York, 1967), Vol. 3.
- [55] M. Aven, D. T. F. Marple, and B. Segall, *J. Appl. Phys.* **32**, 2261 (1961).
- [56] D. E. Aspnes and A. A. Studna, *Phys. Rev. B* **27**, 985 (1983).
- [57] S. Adachi and T. Taguchi, *Phy. Rev. B*, **43**, 9569 (1991)
- [58] T. Yao, *Jpn., J. Appl. Phys.* **25**, L544 (1986).
- [59] J. Petruzzello, B. L. Greenberg, D. A. Cammack and R. Dalby, *J. Appl. Phys.*, **63**, 2299 (1988).
- [60] See for example, M. L. Cohen and J. R. Chelikowsky, *"Electronic Structure and Optical Properties of Semiconductors"*, (Springer-Verlag, Berlin, 1988), and references therein.
- [61] M. Y. Jiang, G. Pajer, E. Burstein, M. S. Yeganeh and A. G. Yodh, (to be published).
- [62] M. Born, and E. Wolf, *Principles of Optics* (Pergamon Press, Oxford, 1975).
- [63] P. D. Maker, R. W. Terhune, M. Nisenoff, and C. M. Savage *Phys. Rev. Lett.* **8**, 21 (1962).

- [64] J. Jerphagnon, and S. K. Kurtz, *J. Appl. Phys.* **41**, 1667 (1970).
- [65] For details of sample growth and morphology see M. C. Tamargo, J. L. deMiguel, D. M. Hwang, and H. H. Farrell, *J. Vac. Sci. Technol. B* **6**, 784 (1988) and references therein.
- [66] T. Stehlin, M. Feller, P. Guyot-Sionnest, and Y. R. Shen, *Opt. Lett.* **13**, 389 (1988).
- [67] M. Cardona, *Modulation Spectroscopy*, (Academic, New York, 1969).
- [68] M. I. Bell, *Proceeding of the Conference on the Electronic Density of States*, Gaithersburg, Maryland, 1969 (unpublished).
- [69] C. Y. Fong and Y. R. Shen, *Phys. Rev. B* **12**, 2325 (1975).
- [70] H. Asai, and K. Oe, *J. Appl. Phys.* **54**, 2052 (1983).
- [71] G. E. Pikus and G. L. Bir, *Sov. Phys. Solid State* **1**, 136 (1959).
- [72] G. E. Pikus and G. L. Bir, *Sov. Phys. Solid State* **1**, 1502 (1960).
- [73] A. Gavini and M. Cardona, *Phy. Rev. B* **1**, 672 (1970).
- [74] D. Berlincourt, H. Jaffe and L. R. Shiozawa, *Phys. Rev.* **129**, 1009 (1963).
- [75] Y. F. Tsay, S. S. Mitra, and B. Bendow, *Phys. Rev. B* **10**, 1476 (1974).
- [76] D. W. Langer, R. N. Euwema, K. Era and T. Koda, *Phys. Rev. B* **2**, 4005 (1970).

- [77] R. M. Park, H. A. Mar, and N. M. Salansky, *J. Vac. Sci. Technol.* **B3**, 676 (1985); R. L. Longini, *Sol. St. Elec.* **5**, 127 (1962).
- [78] P. Dawson, R. A. Wilson, C. W. Tu, and R. C. Miller *Appl. Phys. Lett.* **48**, 541 (1986).
- [79] S. J. Hsieh, E. A. Patten, and C. M. Wolfe, *Appl. Phys. Lett.* **45**, 1127 (1984).
- [80] P. Voision, G. Bastard, C. E. T. Goncalves da Silva, M. Voos, L. L. Chang, and L. Esaki, *Solid State Comm.* **39**, 79 (1981).
- [81] H. C. Liu, *Superlattices and Microstructures*, **3**, 413 (1987).
- [82] P. Enders, *Phys. Stat. Sol. (b)* **139**, K113 (1987).
- [83] R. A. Morrow and K. R. Brownstein, *Phy. Rev. B*, **30**, 678 (1984).
- [84] R. Morrow, *Phys. Rev. B*, **35**, 8074 (1987).
- [85] R. A. Morrow, *Phys. Rev. B*, **36**, 4836 (1987).
- [86] J. Thomsen, G. T. Einevoll and P. C. Hemmer, *Phys. Rev. B*, **39**, 12783, (1989).
- [87] I. Galbraith and G. Duggan, *Phys. Rev. B*, **38**, 10057 (1988).
- [88] A. P. French, E. F. Taylor, *An Introduction to Quantum Physics*, (W. W. Norton, New York, 1987).
- [89] J. W. Matthews, *Epitaxial Growth* (Academic, New York, 1975).

- [90] W. T. Read, *Philos. Mag.* **45**, 775, 1115 (1954).
- [91] R. Labusch and W. Schroter in *Dislocations in Solids*, edited by F. R. N. Nabarro (North-Holland, Amsterdam, 1980), Vol 5, p. 127.
- [92] J. M. Woodall, G. D. Pettit, T. N. Jackson, C. Lanza, K. L. Kavanagh and J. W. Mayer, *Phys. Rev. Lett.* **51**, 1783 (1983).
- [93] W. Schroter and R. Labusch, *Phys. Stat. Sol.* **36**, 359 (1969).
- [94] H. Kroemer VLSI vol10 and referces therein.
- [95] E. Y. Wang, W. A. Albers and C. E. Bleil in "*II-VI semiconducting compounds*", D. G. Thomas ed., (Benjamin, New York, 1967), p136.
- [96] R. E. Nahory and J. L. Shay, *Phys. Rev. Lett.* **21**, 1569 (1968).
- [97] H. H. Farrell, M. C. Tamargo, and J. L. de Miguel, *Appl. Phys. Lett.* **58**, 355 (1991).
- [98] D. W. Tu and A. Kahn, *J. Vac. Sci. Technol.* **A3**, 922 (1985).
- [99] D. Li, J. M. Gonsalves, N. Otsuka, J. Qiu, M. Kobayashi, and R. L. Gunshor, *Appl. Phys. Lett.* **57**, 499 (1990).
- [100] S. Wang, "*Solid State Electronics*", (McGraw-Hill, New York, 1963).
- [101] N. V. Joshi, *Phys. Rev. B* **27**, 6272 (1983).

- [102] R. Shankar “ *Principles of Quantum Mechanics*” (Plenum Press, New York, 1985), p 186.
- [103] B. V. Zhuk, I. A. Zhukov and A. A. Zlenko, *Solid-state Electronics* **29**, 247 (1986).
- [104] H. Shen, P. Parayanthal, F. H. Pollak, M. Tomkiewicz, T. J. Drummond and J. N. Schulman, *Appl. Phys. Lett.* **48**, 653 (1986).
- [105] K. Yokoyama and K. Hess, *Phys. Rev. B* **33**, 5595 (1986).
- [106] T. Yao, in *Technology and Physics of Molecular Beam Epitaxy*, edited by E. H. C. Parker (plenum, New York), p. 313.
- [107] F. Wooten, “*Optical Properties of Solids*”, (Academic Press, San Diego, 1972).